ANTINEUTRINO-INDUCED CHARGE CURRENT QUASI-ELASTIC NEUTRAL HYPERON PRODUCTION IN ARGONEUT

by

SAIMA FAROOQ

B.S.Ed., Government College of Education for Science, Pakistan, 2003

M.Sc., University of the Punjab, Pakistan, 2006

AN ABSTRACT OF A DISSERTATION

submitted in partial fulfillment of the
requirements for the degree

DOCTOR OF PHILOSOPHY

Department of Physics
College of Arts and Sciences

KANSAS STATE UNIVERSITY
Manhattan, Kansas

2016

Abstract

This dissertation presents the first topological study of the charge current quasi-elastic (CCQE) neutral hyperon production induced by antineutrinos in the ArgoNeuT detector, a liquid argon time projection chamber (LArTPC) at Fermilab, using 1.20×10^{20} protons-on-target (POT), in the NuMI beam operating in the low energy antineutrino mode. The total cross section for the CCQE neutral hyperon production is reported at the mean production energy of 3.42 GeV. The event yield in data is consistent with the predicted cross section, $\sigma = 2.7 \times 10^{-40}$ cm^2:

$$\sigma(_{CCQE_{\Lambda^0+\Sigma^0}}) = \big(3.7 \pm 1.9(\text{stat.}) \pm 1.5\ (\text{sys.})\big) \times 10^{-40}\ \text{cm}^2.$$

The study sets a 90% confidence level (C.L.) upper limit on the total cross section of CCQE neutral hyperon production:

$$\sigma(_{CCQE_{\Lambda^0+\Sigma^0}}) \quad < \quad 7.3 \times 10^{-40}\ \text{cm}^2 \text{ at } 90\%\ \text{C.L.}$$

ANTINEUTRINO-INDUCED CHARGE CURRENT QUASI-ELASTIC NEUTRAL HYPERON PRODUCTION IN ARGONEUT

by

SAIMA FAROOQ

B.S.Ed., Government College of Education for Science, Pakistan, 2003

M.Sc., University of the Punjab, Pakistan, 2006

A DISSERTATION

submitted in partial fulfillment of the
requirements for the degree

DOCTOR OF PHILOSOPHY

Department of Physics
College of Arts and Sciences

KANSAS STATE UNIVERSITY
Manhattan, Kansas

2016

Approved by:

Major Professor
Tim Bolton

Copyright

Abstract

This dissertation presents the first topological study of the charge current quasi-elastic (CCQE) neutral hyperon production induced by antineutrinos in the ArgoNeuT detector, a liquid argon time projection chamber (LArTPC) at Fermilab, using 1.20×10^{20} protons-on-target (POT), in the NuMI beam operating in the low energy antineutrino mode. The total cross section for the CCQE neutral hyperon production is reported at the mean production energy of 3.42 GeV. The event yield in data is consistent with the predicted cross section, $\sigma = 2.7 \times 10^{-40}$ cm^2:

$$\sigma(_{CCQE_{\Lambda^0+\Sigma^0}}) = \big(3.7 \pm 1.9(\text{stat.}) \pm 1.5\ (\text{sys.})\big) \times 10^{-40}\ \text{cm}^2.$$

The study sets a 90% confidence level (C.L.) upper limit on the total cross section of CCQE neutral hyperon production:

$$\sigma(_{CCQE_{\Lambda^0+\Sigma^0}}) \quad < \quad 7.3 \times 10^{-40}\ \text{cm}^2 \text{ at } 90\%\ \text{C.L.}$$

Contents

List of Figures

Acknowledgments

First, I am thankful to God for providing me the opportunity to pursue my career. He gave me strength and fortitude to travel to the United States to seek my goals.

I would like to express my deepest gratitude and sincere thanks to my Ph.D. advisor, Tim Bolton. Thank you for your patience with me and for always answering my questions with a smile, even if I asked them more than once. Regardless of geographical boundaries, your doors have always been open for me. I enjoy your humor, and it has always given me energy, especially when the times are stressful. Without your support this dissertation would not have been possible. Thank you so much for equipping me with the skills that will surely help me in my future endeavors.

I have been blessed with great teachers throughout my life, and without them, I would not have been in a physics graduate program. I would like to take this opportunity to thank all of them, especially my 10^{th} grade teacher; Neelam Khan. Thank you for being such a great physics teacher, you inspired me to pursue physics, and you are my role model. I was pleasantly surprised and delighted to see you after many years at KSU. I enjoyed our friendship and the time we spent together in Manhattan. Thank you for your constant support and encouragement throughout these years. I also want to say special thanks to Prof. Mujahid Kamran, who was my masters teacher at the University of Punjab, Pakistan. Thank you for your confidence in me and for motivating me to apply for a graduate program in the U.S. I am indebted to you for my academic career.

I want to thank all the members of the ArgoNeuT and MicroBooNE collaborations. Ornella Palamara thank you for helpful comments and discussions; Sam Zeller for many helpful comments; Mitch Soderberg for your guidance; Eric Church for helping me debug my codes when I was a beginner; Tingjun Yang for many enlightening physics conversations; Brian Page for introducing me to the ArgoNeuT and the software.

I would take this opportunity to thank Dr. Amit Chakrabarti for his support during my graduate studies. I owe thanks to the members of High Energy Physics/Cosmology at KSU; Glenn Horton-Smith, Yurii Maravin, Larry Weaver, Bharat Ratra, Andrew Ivanov, Ketino Kaadze and Lado Samushia for your support during my stay at KSU. I want to thank other people/colleagues at KSU; Mikhail Makouski, Sadia Khalil, Shruti Shrestha, Deepak Shrestha, Irakli Chakaberia, Anatoly Pavlov, Sachiko McBride, Sara Crandall, Pi-Jung Chang, Irakli Svintradze and Nikoloz Sklirladze. Sadia, I would never forget the evenings we spent together, and the adventures we had, while at Fermilab. Sara, thank you so much for correcting my thesis, you are so kind to help.

My list is not complete without thanking Mahsana Ahsan and Mansoora Shamim. You both helped me tremendously when I arrived Manhattan amidst your own move from Manhattan. You are the ones who finally made me decide, being a female from Pakistan, to come to the United States. Mansoora, I always cherish the memory that you eventually filed a housing application for me at KSU when I didn't understand the consequences of delaying it. Thank you so much for all the care.

I would also like to recognize the help I got from the staff in the Physics Department; Peggy Matthews, Pamela Anderson, Jane Peterson (I miss you), Kim Coy, and Kimberly Elliott. Thank you for helping with the payroll, travel and housing arrangements for my travel between KSU & Fermilab and during my studies at KSU.

My journey through graduate school would not be the same if I had not met great friends at KSU and Fermilab. I want to thank Shuo Zeng, Bachana Lomsadze, Govind Paneru, Raiya Ebini, Varun Makhija, Chenchen Wang, Joe Grange and Ranjan Dharmapalan for great company and delightful conversations. Thanks to Fatima Anis and Siddique Khan for an awesome time.

Ammi and Abbu, I cannot thank you enough for your sacrifices in letting me go too far from you and encouraging me along the way. I am so grateful for all the values you have instilled in me, especially the tolerance and kindness. The training that I got at home has

enabled me to reach this stage of my life. I am sorry that I have not been able to maintain more frequent contact with you. I hope I can be more responsible in the times to come.

A particular thanks goes to my brother, M. Omer Farooq, for his unconditional support and understanding. Last, but not least, I want to thank my husband, M. Asif Nawaz, for his sacrifices, patience, and encouragement. Over the years you've helped me find my voice. Thank you for putting up with me.

My list remains incomplete. I want to say thanks to all the people who were supportive of me throughout my career.

Dedication

To my parents Farooq Ahmed Uppal and Abida Bano, whose way of life has always been a source of inspiration for me.

Chapter 1

Introduction

This thesis describes a measurement of total cross section of charge current quasi-elastic (CCQE) neutral hyperon production induced by the scattering of antineutrinos by an argon target, at ArgoNeuT detector in Fermilab.

$$\begin{aligned} \bar{\nu}_\ell + p &\rightarrow \ell^+ + \Lambda^0, \\ \bar{\nu}_\ell + p &\rightarrow \ell^+ + \Sigma^0. \end{aligned} \tag{1.1}$$

The study also sets a 90% confidence-level (C.L.) upper limit on the CCQE neutral hyperon production total cross section. The study of this process is important as the existing measurements are sparse and limited by statistics, and the theoretical models vary. Making use of the images from a liquid argon time projection chamber (LArTPC) with unprecedented resolution, this study presents the first topological analysis of CCQE neutral hyperon production in a LArTPC experiment. The knowledge gained by visual scanning of beautiful images of neutrino interactions is crucial to develop and improve reconstruction techniques in the future LArTPC experiments. Occurring only via antineutrinos, these processes can serve as 'antineutrino tagger' in the future bigger detectors with intense beams and longer runtimes.

There are five chapters in this thesis. Chapter 1 gives an introduction to the neutrino, its

properties, neutrino oscillations and relevant measurements, followed by detailed theoretical description of the processes shown in Equation. 1.1. Chapter 2 introduces the general idea of the LArTPC detector technique and associated challenges in its construction and operation. Chapter 3 describes the ArgoNeuT experiment in particular. Chapter 4 presents the neutrino event generation and simulation in the detector. It also describes the LArSoft sofware used for neutrino events reconstruction in the detector. Chapter 5 gives a step-by-step explanation of the analysis and the results.

1.1 Prediction of Neutrino

Neutrinos are one of the most abundant particles in the universe, yet among the least understood. There are trillions of neutrinos passing through the human body every second. Being electrically neutral and almost massless, these weakly interacting particles simply pass through the matter. Neutrino research, spread over decades, has brought many discoveries along with four Nobel prizes to date. In 1920s, many elements were known to have beta decay, in which a heavy radioactive nucleus transforms to a slightly lighter one, with the release of an electron.

$$N^0(A, Z) \rightarrow N(A, Z + 1) + e^-. \tag{1.2}$$

Here N^0 and N are parent and daughter nuclei, respectively and e^- is an electron. For a two-body decay with the parent nucleus at rest, the conservation of energy and momentum requires electron's energy to be a fixed value[1],

$$E_e = \frac{{m_{N^0}}^2 - {m_N}^2 + {m_{e^-}}^2}{2m_N}. \tag{1.3}$$

However, the measurements of electron energy gave a wide continuous spectra instead of a constant value. It was suggested that the spread in the electron energy spectrum could

[1]This thesis employs the unit system used in high energy physics in which the fundamental constants have values $\hbar = c = 1$, and all energies are expressed in GeV or MeV.

be due to the energy losses before the electron was detected, or due to experimental errors. It was also thought that the energy and momentum conservation laws are broken. By the late 1920s, it was more and more evident that this spread is real. In 1930, the idea of the neutrino was suggested by Pauli, who proposed that a light neutral particle (later to be called neutrino) may be involved in β-decay [1]. By adding this new particle, the electron can carry kinetic energy ranging from zero to the maximum allowed, whereas, the other light particle carries the balance. The idea of the neutrino was not taken well until 1934 when Fermi formulated his β-decay model and successfully explained the experimental observations [2]. The actual β-decay equation is as follows (note that it is actually an antineutrino in the final state):

$$n \rightarrow p + e^{-} + \bar{\nu_e}. \tag{1.4}$$

1.2 Discovery of Neutrino

The neutrino was detected in 1956, by Cowan, Reines and colleagues [3]. They used a flux of antineutrinos from Savannah River reactor in South Carolina. An antineutrino produced in beta decay reacts with a proton in the tank of water and $CdCl_2$ and produces a neutron and a positron.

$$\bar{\nu_e} + p \rightarrow n + e^{+}. \tag{1.5}$$

The positron then annihilates with an electron in the medium and produces two photons, which are detected by the scintillator and photomultiplier tubes in the tank. The neutron undergoes neutron capture interaction in the tank, $n + {}^{108}\mathrm{Cd} \rightarrow {}^{109}\mathrm{Cd}^{*} \rightarrow {}^{109}\mathrm{Cd} + \gamma$. The photon produced by the nuclear de-excitation is detected approximately 5 μsec after the $e^{+}e^{-}$ pair-annihilation gammas, therefore producing a distinctive signature of a neutrino interaction. The experiment produced $\sim$3 events per hour. The data was compared with

the data when the reactor was off, and experimentally the neutrino was discovered. A Nobel Prize was awarded in 1995 for this discovery.

Second and third flavors of the neutrino were discovered later: ν_μ at Brookhaven in 1962 [4] and ν_τ at Fermilab in 2000 [5].

1.3 Brief Description of Neutrino

After the discovery of the neutrino, it was natural to measure the properties of this newly discovered particle. Today we know that the neutrino is a spin 1/2 particle that has three flavors, ν_e, ν_μ and ν_τ, and that each one of them has an anti-particle. It interacts via the weak interaction mediated by $W^{\pm}$ and Z^0 bosons; hence, it has very small interaction cross section.

1.3.1 Parity Violation and Helicity

Parity was considered to be a symmetry of all fundamental interactions until 1957 [6] when parity violation was established experimentally in the weak interactions. In the experiment, unstable ^{60}Co atoms are polarized using a magnetic field so that their nuclear spins point in one direction and the direction of outgoing electrons from β-decay is observed. It was discovered that the direction of emitted electrons is almost always opposite to the direction of the spin of the parent nuclei (or to the direction of magnetic field) [7]. This anti-correlation between the direction of electrons and the nuclear spin established that parity (mirror symmetry) is violated in the weak interactions. In order to balance the total spin and momentum in the interaction, the electron kinematics dictate that there must be an accompanied antineutrino with a specific alignment between its momentum and spin vectors. It was determined that the momentum and spin vectors for the neutrino are anti-parallel [8]. The inner product between a particle's momentum and spin vector at any instant is known as its helicity. A neutrino, having its momentum and spin vectors anti-parallel is

called 'left-handed', whereas, an antineutrino with its momentum and spin vectors parallel is called 'right-handed'. With the recent discovery of non-zero neutrino mass, a neutrino or antineutrino can be right-handed or left-handed depending on the frame of reference.

1.3.2 Charge Current and Neutral Current Interactions

When a W boson is emitted (W^+ for neutrino and W^- for antineutrino), the interaction is called a charge current interaction, and a charged lepton of the same flavor as neutrino is emitted to conserve the charge and lepton flavor at the vertex:

$$\nu_\mu + N \rightarrow N' + \mu. \tag{1.6}$$

Neutral current interactions of neutrino were first observed at CERN in 1973 [9]. In these interactions neutrino interacts through an exchange of a Z^0 boson instead of charged $W^\pm$ boson.

$$\nu_\ell + X \rightarrow \nu_\ell + Y. \tag{1.7}$$

1.3.3 Neutrino Mass

Neutrinos were thought to be massless until recently. The next section describes the theory and observations of neutrino oscillations, which prove that neutrinos oscillate between flavors and have non-zero mass.

1.4 Neutrino Oscillations

There is strong evidence that neutrino transform from one flavor to another after traveling a distance. Neutrino oscillations (flavor-transformation) and the resulting non-zero mass of neutrino is one of the very few phenomenon not predicted by the standard model. Neutrino

oscillations are observed for neutrinos created in the sun, the earth's atmosphere, nuclear reactors, and accelerators. This section generally follows the description given in Ref. [10] and briefly presents the theory of neutrino oscillations and the experimental evidence.

1.4.1 Formalism

We start with the leptonic decay: $W^+ \rightarrow \ell_\alpha{}^+ + \nu_i$. Here α is lepton flavor, i.e. α = e, μ, τ, and i is the neutrino mass eigenstate with i = 1, 2, 3. The amplitude of the decay is $U^*_{\alpha i}$, and the eigenstates of weak hamiltonian (flavor eigenstates) can be written as a linear superposition of the eigenstates of total hamiltonian (mass eigenstates) as follows,

$$|\nu_\alpha >= \sum_i U^*{}_{\alpha i} |\nu_i >. \tag{1.8}$$

Here, ν_α is a neutrino with flavor α, U are the elements of the flavor mixing matrix; the 'PMNS' matrix, and ν_i is a neutrino with mass eigenstate of i. In the three neutrino mixing, the PMNS matrix can be written as follows,

$$U = \begin{bmatrix} U_{e1} & U_{e2} & U_{e3} \\ U_{\mu 1} & U_{\mu 2} & U_{\mu 3} \\ U_{\tau 1} & U_{\tau 2} & U_{\tau 3} \end{bmatrix}. \tag{1.9}$$

A neutrino created as ν_α with flavor α in its rest frame evolves in time as,

$$|\nu_\alpha(\tau) >= \sum_i U^*{}_{\alpha i} e^{-i m_i \tau_i} |\nu_i(0) >. \tag{1.10}$$

Here, τ is the neutrino's proper time and m is its mass. The above equation can be written as following for the laboratory frame,

$$|\nu_\alpha(t) >= \sum_i U^*{}_{\alpha i} e^{-i(E_i t - p_i L)} |\nu_i(0) >. \tag{1.11}$$

The term is $e^{-i(Et-pL)}$ is the characteristic phase of the mass eigenstate, where, E is energy, t is time and p is momentum and L is the distance traveled. The neutrino mass is much smaller than its momentum for all practical purposes, so the terms with order higher than two in m_i are ignored, hence, $E_i = \sqrt{p^2 + m_i^2} \approx p + {m_i}^2/2p$. This also implies the neutrino energy $E_i \approx p$ for each mass state i. Also, again using the assumption of negligible neutrino mass as compared to its energy, we have $t \approx L$, where L is the distance propagated in time t. Now the Equation 1.11 becomes,

$$|\nu_\alpha(L) >= \sum_i {U^*}_{\alpha i} e^{-i(m_i^2/2E)L} |\nu_i >. \tag{1.12}$$

A neutrino with initial flavor α can travel a distance L and detected as a neutrino with flavor β.

$$|\nu_\alpha(L) >= \sum_\beta [\sum_i {U^*}_{\alpha i} e^{-i(m_i^2/2E)L} U_{\beta i}] |\nu_\beta >. \tag{1.13}$$

And the probability of transformation from flavor α to flavor β can be written as,

$$P(\nu_\alpha \to \nu_\beta) = | < \nu_\beta | (\nu_\alpha(L) > |^2 = |\sum_i {U^*}_{\alpha i} e^{-i(m_i^2/2E)L} U_{\beta i}|^2, \tag{1.14}$$

$$\begin{aligned} P(\nu_\alpha \to \nu_\beta) = \delta_{\alpha\beta} &- 4 \sum_{i>j} \Re({U^*}_{\alpha i} U_{\beta i} U_{\alpha j} {U^*}_{\beta j}) \sin^2(\Delta m_{ij}^2 \frac{L}{4E}) \\ &+ 2 \sum_{i>j} \Im({U^*}_{\alpha i} U_{\beta i} U_{\alpha j} {U^*}_{\beta j}) \sin(\Delta m_{ij}^2 \frac{L}{2E}). \end{aligned} \tag{1.15}$$

Here, $\Delta m_{ij}^2 = m_i^2 - m_j^2$. Equation 1.15 is for neutrino oscillations. Transforming it for antineutrino oscillations requires replacing the mixing matrix U by its complex conjugate, which changes the sign of the third term in the equation (a negative sign instead of a positive sign). It is worth noting that the third term in the above equation violates charge-parity conservation (CP), and if there is CP violation in neutrino sector, then the probability of neutrino with flavor α to oscillate to a neutrino of flavor β will not be the same as probability

of antineutrino with flavor α to oscillate to an antineutrino of flavor β. This mechanism may explain the large scale CP violation in nature – matter-antimatter asymmetry.

Now, inserting the constants $\hbar$ and c in ${\Delta m_{ij}}^2 \frac{L}{4E}$,

$$\frac{\Delta m_{ij}^2 L}{4E} = 1.27 \frac{\Delta m_{ij}^2 (eV^2) L(Km)}{E(GeV)}. \tag{1.16}$$

and finally the oscillation equation can be written as follows,

$$\begin{aligned} P(\nu_\alpha \to \nu_\beta) = \delta_{\alpha\beta} - 4 \sum_{i>j} \Re({U^*}_{\alpha i} U_{\beta i} U_{\alpha j} {U^*}_{\beta j}) \sin^2(1.27 \Delta m_{ij}^2 \frac{L}{E}) \\ + 2 \sum_{i>j} \Im({U^*}_{\alpha i} U_{\beta i} U_{\alpha j} {U^*}_{\beta j}) \sin(2.54 \Delta m_{ij}^2 \frac{L}{E}). \end{aligned} \tag{1.17}$$

1.4.2 Two Neutrino Oscillation

The two neutrino oscillation case is important as it represents the approximate situation in many experiments. In the case of two neutrino oscillation, the mixing matrix can be simplified as

$$U = \begin{bmatrix} \cos\theta & \sin\theta \\ -\sin\theta & \cos\theta \end{bmatrix}. \tag{1.18}$$

Here, θ is the mixing angle. After substituting the matrix elements in Equation 1.17, one gets the oscillation probability for two neutrino mixing as follows,

$$P(\nu_\alpha \to \nu_\beta) = \sin^2 2\theta \sin^2(1.27 \Delta m^2 \frac{L}{E}). \tag{1.19}$$

And the appearance probability as follows,

$$P(\nu_\alpha \to \nu_\alpha) = 1 - \sin^2 2\theta \sin^2(1.27 \Delta m^2 \frac{L}{E}). \tag{1.20}$$

1.4.3 Three Neutrino Oscillation

The three neutrino mixing matrix can be written as follows,

$$U = \begin{bmatrix} U_{e1} & U_{e2} & U_{e3} \\ U_{\mu 1} & U_{\mu 2} & U_{\mu 3} \\ U_{\tau 1} & U_{\tau 2} & U_{\tau 3} \end{bmatrix} \tag{1.21}$$

$$= \begin{bmatrix} 1 & 0 & 0 \\ 0 & c_{23} & s_{23} \\ 0 & -s_{23} & c_{23} \end{bmatrix} \begin{bmatrix} c_{13} & 0 & s_{13}e^{-i\delta} \\ 0 & 1 & 0 \\ -s_{13}e^{-i\delta} & 0 & c_{13} \end{bmatrix} \begin{bmatrix} c_{12} & s_{12} & 0 \\ -s_{12} & c_{12} & 0 \\ 0 & 0 & 1 \end{bmatrix} \begin{bmatrix} e^{i\alpha_1/2} & 0 & 0 \\ 0 & e^{i\alpha_2/2} & 0 \\ 0 & 0 & 1 \end{bmatrix}$$

$$= \begin{bmatrix} c_{12}c_{13} & s_{12}c_{13} & s_{13}e^{i\delta} \\ -s_{12}c_{23} - c_{12}s_{23}s_{13}e^{i\delta} & c_{12}c_{23} - s_{12}s_{23}s_{13}e^{i\delta} & s_{23}c_{13} \\ s_{12}s_{23} - c_{12}s_{23}s_{13}e^{i\delta} & -c_{12}s_{23} - s_{12}c_{23}s_{13}e^{i\delta} & c_{23}c_{13} \end{bmatrix} \begin{bmatrix} e^{i\alpha_1/2} & 0 & 0 \\ 0 & e^{i\alpha_2/2} & 0 \\ 0 & 0 & 1 \end{bmatrix}.$$

Here, $c_{ij} = \cos\theta_{ij}$ and $s_{ij} = \sin\theta_{ij}$, with three mixing angles θ_{ij} (θ_{12}, θ_{23}, θ_{13}) and δ is Dirac CP-violating phase. α_1 and α_2 are the Majorana CP-violating phases which are non-zero if neutrinos are Majorana particles. There are three mass splittings; Δm^2_{12}, Δm^2_{23}, Δm^2_{13}, however, only two are independent as $\Delta m^2_{12} + \Delta m^2_{23} + \Delta m^2_{13} = 0$.

Three neutrino oscillation can be described in terms of two neutrino oscillation because of the two experimental measurements; θ_{13} is small and two mass splittings are almost equal as compared to the third one (that is, $|\Delta m^2_{32}| = |\Delta m^2_{13}|$). Hence, for example, ν_μ disappearance probability reduces to

$$P(\nu_\mu \to \nu_\mu) = 1 - \sin^2(2\theta_{23})\sin^2(1.27\Delta m^2_{13}\frac{L}{4E}) + \text{sub-leading terms.} \tag{1.22}$$

If the mass of ν_3 is higher than ν_1, the mass hierarchy is called as 'normal' and if the mass of ν_3 is lower than ν_1, then the mass hierarchy is called as 'inverted'. This can be seen

in Figure 1.1. Even though the above equation remains the same for normal and inverted hierarchy (that is, if Δm^2 is replaced by -Δm^2), matter-effects [11, 12] may make the sign observable, as neutrino oscillations get modified in case of neutrinos propagating in matter. Matter effects arise because an electron-neutrino traveling in the medium can interact via W and Z boson, whereas, muon- and tau-neutrinos can only interact via Z at low energy. This effect changes the oscillation probability in the matter as compared to the vacuum. Matter effects are sensitive to the neutrino mass ordering and different for neutrinos and antineutrinos.

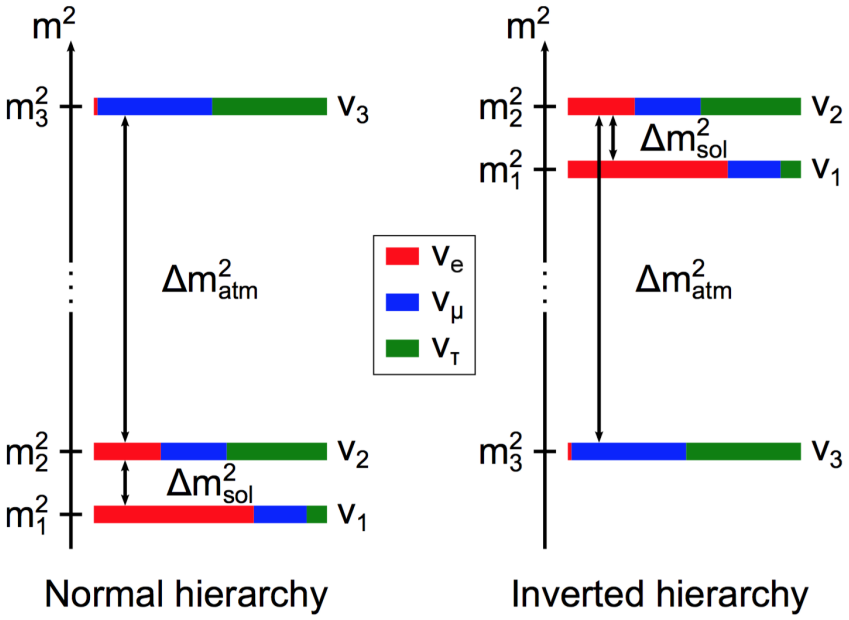

Figure 1.1: *Neutrino mass squared spectra for normal hierarchy (left) and inverted hierarchy (right). Figure from Ref. [13].*

1.4.4 Acquisition of Mass in Standard Model

The standard model does not include right-handed neutrinos or left-anded antineutrinos, thus neutrinos do not have mass. One way of giving mass to the neutrinos is through a 'Dirac mass term' [14], which is by adding a right handed neutrino field ν_R to the model;

$$\mathcal{L}_D = -m_D \bar{\nu_L} \nu_R + h.c. \tag{1.23}$$

Another way of giving mass to the neutrino is via 'Majorana mass term', which may be constructed out of ν_R alone, in which case, we have the right-handed Majorana mass, or out of ν_L alone, in which case we have the left-handed Majorana mass. A Majorana mass term of ν_R is

$$\mathcal{L}_M = -\frac{1}{2} \bar{\nu_R}^C M_R \nu_R + h.c. \tag{1.24}$$

Here m_D and M_R are mass parameters and ν_R^C is the charge conjugate of ν_R and $h.c.$ is the hermitian conjugate of the preceding term. If the neutrino is a Majorana particle, then ν_R and ν_L are related to each other (one is the charge conjugate of the other and vice versa) [15]. Adding this term with the Dirac mass term, one gets,

$$-\mathcal{L} = m_D \bar{\nu_L} \nu_R + \frac{1}{2} \bar{\nu_R}^C M_R \nu_R + h.c. \tag{1.25}$$

After diagonalizing, the neutrino mass matrix is

$$M = \begin{bmatrix} 0 & m_D \\ m_D & M_R \end{bmatrix}. \tag{1.26}$$

and the eigenvalues are

$$\lambda_\pm = \frac{M_R \pm \sqrt{{M_R}^2 + 4{m_D}^2}}{2}. \tag{1.27}$$

λ_+ gives the higher value ($\sim M_R$), which corresponds to heavy neutrino and the λ_- gives the lower value ($\sim -{m_D}^2/M_R$) and corresponds to a light neutrino. This interesting "seesaw" mechanism may explain the tiny observed masses of neutrinos; as one mass gets heavier, the other one gets lighter.

1.4.5 Solar Neutrino Oscillations

Solar neutrinos arise from nuclear reactions in solar core that produce electron neutrinos. The biggest contribution of neutrino flux from sun is produced via so-called 'pp chain', with a smaller fraction produced via the CNO cycle. The solar neutrino spectrum is calculated by the 'Standard Solar Model' (SSM), which gives the neutrino flux from different reactions [16] as shown in Figure 1.2. The highest flux pp chain produces lower energy neutrinos (<0.42 MeV), so detecting them is an experimental challenge. Most of the solar neutrino experiments measure neutrinos from boron-8 reaction; they are rare but are higher energy (<15 MeV).

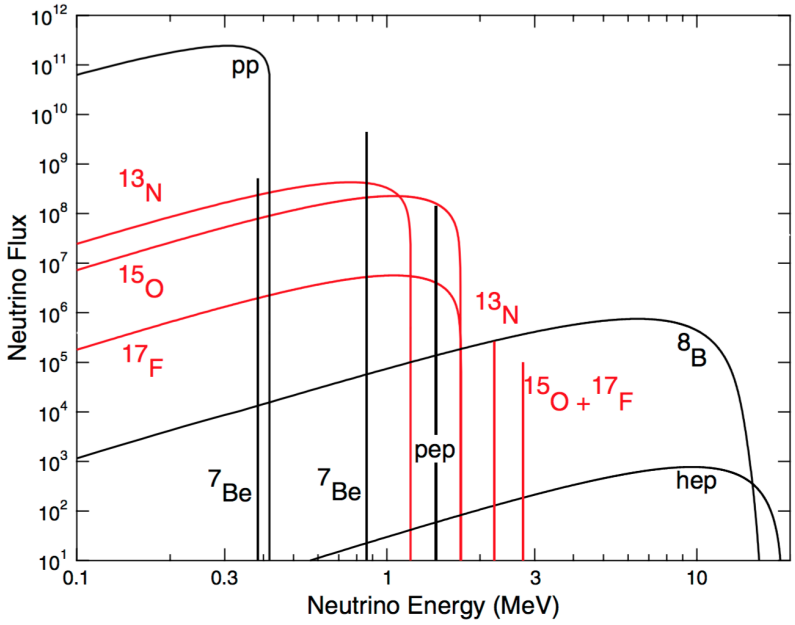

Figure 1.2: *Solar neutrino flux. pp chain in black and CNO cycle in red. The units for continuous spectra are $cm^{-2}s^{-1}MeV^{-1}$ and for Line fluxes are $cm^{-2}s^{-1}$. Figure from Ref. [17].*

Solar neutrinos were first observed in late 1960s in an experiment at Homestake mine in South Dakota by Davis et al. [18]. The experimental setup included a 100,000 gallon tank of common dry-cleaning fluid (C_2Cl_4) placed 4850 feet underground to avoid any interference

of cosmic rays. When an electron neutrino interacts with a clorine-37 atom, it is transformed to radioactive isotope of argon-37 with a production of electron.

$$\nu_e + {}^{37}\mathrm{Cl} \rightarrow {}^{37}\mathrm{Ar} + e^-. \tag{1.28}$$

The solar neutrino flux at earth was measured by counting the number of argon-37 nuclei inside the tank. It was found that only 1/3 of the total predicted flux by SSM is detected by the experiment. This discrepancy between prediction and measurement created the 'Solar Neutrino Problem'. It was thought that there were some mistakes in the experiment or the SSM was wrong. The Homestake experiment was followed by other experiments such as SAGE (Soviet-American Gallium Experiment) in former Soviet Union, and GALLEX (GALLium EXperiment) and GNO (Gallium Neutrino Observatory) in Italy [19, 20, 21] for the same purpose. They used the process

$$\nu_e + {}^{71}\mathrm{Ga} \rightarrow {}^{71}\mathrm{Ge} + e^- \tag{1.29}$$

to detect a neutrino and also observed significant deficit in solar neutrino flux.

The Kamiokande experiment in Japan measured a significant solar neutrino flux deficit [22]. Kamiokande is also the first experiment to reconstruct the neutrinos direction and confirm that they are actually solar neutrinos [23]. It is a Cherenkov detector consisted of 3,000 tons of water tank with light detecting photomultiplier tubes. Cherenkov light is produced when a charge particle moves faster than the speed of light in a medium. Kamiokande detected neutrinos by detecting the electron or muon from the elastic-scattering of solar neutrinos ($\nu_x + \mathrm{e}^- \rightarrow \nu_x + \mathrm{e}^-$, where $x = e, \mu$). One can note that the experiment is more sensitive to the detection of ν_e as the cross section for neutrino-electron scattering is significantly higher than the neutrino-muon.

Unambigious evidence of solar neutrino oscillations came from Sudbury Neutrino Observatory (SNO) experiment in 2001 [24]. Arthur B. McDonald, the director of SNO experiment

was awarded Nobel Prize for Physics in 2015 for the experiment's contributions towards the discovery of neutrino oscillations (and non-zero mass). SNO experiment is also a Cherenkov experiment with a 1 kton vessel filled with heavy water, D_2O, and photomultiplier tubes viewing the vessel. The experiment can measure the following reactions;

$$\begin{aligned} \nu_e + \mathrm{d} &\rightarrow \mathrm{p} + \mathrm{p} + \mathrm{e}^-(CC), \\ \nu_x + \mathrm{d} &\rightarrow \mathrm{p} + \mathrm{n} + \nu_x \ (\mathrm{NC}), \\ \nu_x + \mathrm{e}^- &\rightarrow \nu_x + \mathrm{e}^-(ES). \end{aligned} \tag{1.30}$$

The CC process is sensitive exclusively to ν_e as solar neutrino energies are too low (<18 MeV) to produce a muon or tau (with rest masses of 106 MeV and 1780 MeV, respectively). The NC process, equally sensitive to all neutrino types, allows the measurement of total neutrino flux. The ES process is also sensitive to all neutrino but has reduced sensitivity to ν_μ and ν_τ. Sensitivity to these three reactions allows SNO to determine the electron and non-electron neutrino components of the solar flux. The total neutrino flux was measured to be three times the ν_e flux, confirming the Standard Solar Model and the previous results; neutrinos do not disappear, but transform from one flavor to another.

1.4.6 Reactor Neutrino Oscillations

The KamLAND experiment in Japan, using neutrinos from nuclear power reactors, measured the oscillation parameters and provided the first observation of sinusoidal nature of neutrino oscillations as a function of L/E [25] Figure 1.3. The KamLAND detector uses the neutrinos from 55 different reactors in Japan and has a mean baseline distance of about 180 km. The detector is made of a stainless steel containment vessel with 1,879 photomultiplier tubes lined inside. The inner layer of the detector is a nylon balloon filled with 1 kiloton of liquid scintillator. Like Cowan and Reines experiment, KamLAND also measures inverse β-decay process in order to detect a $\bar{\nu_e}$. ($\bar{\nu_e} + p \rightarrow n + e^+$).

The positron produces a prompt scintillation light signal, whereas, neutron capture provides a delayed signal. Both signals separated by ∼200 μs distinguish between the background and the signal.

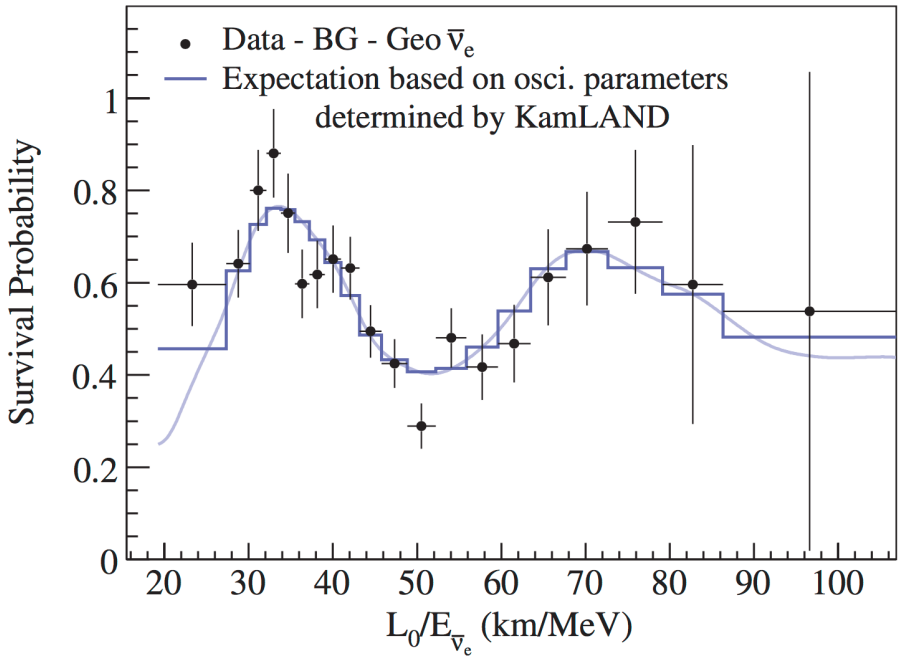

Figure 1.3: *KamLAND result. Figure from Ref. [25].*

Since reactors produce only $\bar{\nu_e}$, KamLAND precisely measures the disappearance of neutrinos, and the neutrino energy spectrum as well. Good energy resolution gives sensitivity to the oscillation frequency measurement, whereas, the solar experiments measure the amplitude of oscillation with higher sensitivity. This can be seen in Figure 1.4, where the KamLAND and solar neutrino experiment results are combined to get an allowed region for oscillation parameters. KamLAND has higher energy resolution and smaller statistical power relative to solar neutrino experiments.

Figure 1.4 shows the contours of allowed regions of parameter space $(\tan^2\theta_{12}, \Delta m^2{}_{21})$ considering three-flavor neutrino oscillations. It includes the data of the solar neutrino experiments SAGE [19], GALLEX [27], GNO [21], Homestake [28], Borexino16 [29, 30], Super-Kamiokande [31, 32, 33] and SNO [26]. Furthermore, the results of the KamLAND

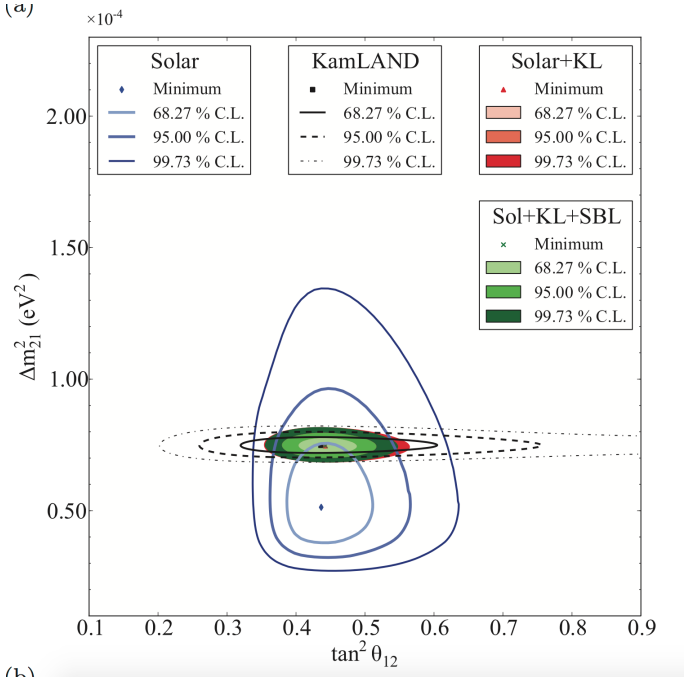

Figure 1.4: *Solar neutrino experiments, KamLAND (KL) and short-baseline (SBL) reactor experiments separate and combined contours of the allowed regions of the parameter space resulting from a three-flavor neutrino oscillation analysis for different confidence levels (C.L.). Figure from Ref. [26].*

experiment [34] are shown, both separately and combined with the solar data.

1.4.7 Atmospheric Neutrino Oscillations

Interaction of cosmic rays (mostly high energy protons) with earth's upper atmosphere produces a shower of hadrons, mostly pions, which produce electron neutrinos and muon neutrinos after decaying to muon and electron as shown below,

$$\begin{aligned} \mathrm{p} + \mathrm{X} &\rightarrow \pi^{\pm} + Y, \text{ (where X and Y are atmospheric molecules)}, \\ \pi^{\pm} &\rightarrow \mu + \nu_{\mu}, \\ \mu &\rightarrow e + \nu_{\mu} + \nu_{e}. \end{aligned} \tag{1.31}$$

The flux of atmospheric neutrinos is smaller than solar neutrinos, but they are higher in

energy and therefore have higher interaction cross section.

The Super-Kamiokande experiment, an enlarged version of Kamiokande experiment, was created to study the solar and atmospheric neutrinos. It consists of a tank containing 50 kiloton of pure water with 11,146 photomultiplier tubes mounted. The detector can identify electrons and muons based on the Cherenkov ring that they produce; however, cannot distinguish between their charge. The experiment measured the zenith angle of the atmospheric neutrinos. The neutrino flux was predicted to be uniform for all zenith angles, in the absence of oscillations, but the contrary was observed. The experiment observed more muon neutrinos coming from the top than the bottom of the earth's atmosphere; whereas the electron neutrinos detected by the detector did not show the same dependence on zenith angle. Somehow, the muon neutrinos were disappearing while traveling through the earth. This result was announced in 1998 and served as the further evidence of neutrino oscillations [35]. The zenith angle distributions of charge current interactions are shown in Figure 1.5, showing the ratio of observed ν_μ events relative to the no oscillations hypothesis in Super-Kamiokande, clearly shows a deficit compared to the distribution if there were no oscillations. Data clearly shows deviation from no-oscillation hypothesis.

1.4.8 Accelerator Neutrino Oscillations

Accelerator neutrinos are produced by accelerated proton beams, the idea is very similar to the production of atmospheric neutrinos. High energy protons hit the beam target and produce pions, which decay to muons and neutrinos. The long baseline experiments can probe the L/E region where atmospheric oscillations are observed. Accelerator based long baseline experiments consists of near and far detectors, with near detector placed near the target of the beam and far detector placed few hundred kilometers far from it. The near detector measures the neutrino beam before oscillation, and the far detector measures the beam after the expected oscillation. Since the measurement depends on comparing two signals, it is very important to make the two detector similar to each other to reduce systematics. There

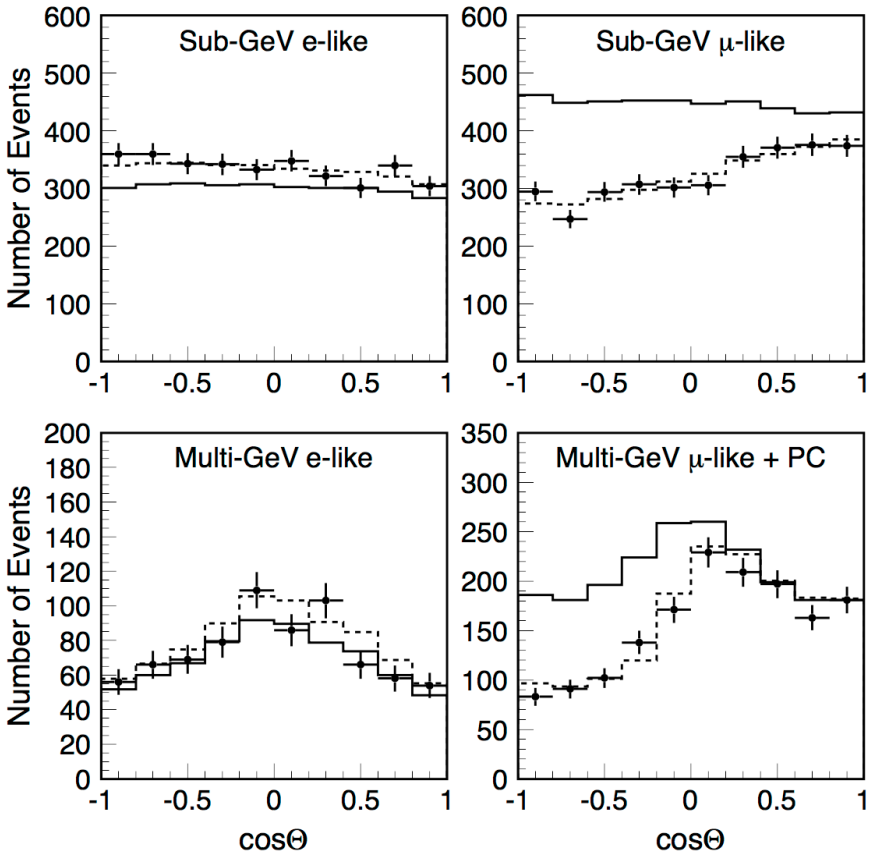

Figure 1.5: *Zenith angle distribution for e-like and μ-like events in Super-Kamiokande. The points show the data, solid lines show the simulation without oscillation and the dashed line is the best-fit expectation for oscillations. Figure from Ref. [36].*

are two types of accelerator based neutrino oscillation experiments, disappearance and appearance experiments. Disappearance experiments measure the deficit in the neutrino flux at the far detector, whereas, appearance experiments detect an appearance of a neutrino flavor in the far detector that was not present at the near detector.

The KEK to Kamioka (K2K) long baseline neutrino oscillation experiment in Japan, was the first to use the accelerator neutrinos to measure the disappearance in the beam of muon neutrinos [37]. The experiment was designed to verify the oscillations observed by

Super-Kamiokande using atmospheric neutrinos. K2K, using a muon neutrino beam of ∼1-2 GeV energy, and a near and far detector separated by 250 km, confirmed muon neutrino disappearance . The experimental results were in agreement with Super-Kamiokande, and later, with MINOS.

The Main Injector Neutrino Oscillation Search (MINOS) experiment is also a long baseline experiment with L = 735 km. MINOS near detector sits at Fermilab, whereas the far detector is located at Soudan, Minnesota. Both the detectors are iron scintillator tracking detectors and are magnetized and can differentiate between neutrino and antineutrino. MINOS is exposed to ν_μ beam and measures ν_μ disappearance and ν_e appearance. Furthermore, the MINOS neutrino beam can be switched to $\bar{\nu_\mu}$ so that also $\bar{\nu_\mu}$ disappearance and $\bar{\nu_e}$ appearance can be studied. MINOS has confirmed K2K and Super-Kamiokande results. In addition, MINOS was able to demonstrate that ν_μ and $\bar{\nu_\mu}$ oscillate analogously [38].

The NuMI Off-Axis ν_e Appearance (NOνA) experiment with its near detector located at Fermilab and far detector in northern Minnesota, separated by 810 km, started operating in 2014. Both detectors are made of highly reflective plastic PVC filled with liquid scintillator. NOνA has recently submitted its first measurements of ν_e appearance [39] and ν_μ disappearance [40].

Atmospheric and accelerator oscillation experiments support ν_μ to ν_τ oscillation observation, although rely on ν_μ disappearance. OPERA is an experiment that has a goal to detect ν_τ. The experiment is located in Gran Sasso National Laboratory in Italy, 730 km from the neutrino source at CERN and detects the oscillation of ν_μ to ν_τ by detecting ν_τ instead of measuring disappearance in ν_μ. The experiment has so far detected 4 ν_τ candidate events [41].

Currently, MINOS at Fermilab and T2K at J-PARC can be considered giving the most precise atmospheric oscillation parameters value from the accelerator experiments [13]. Figure 1.6 depicts the contours of the allowed regions of the $(\sin^2\theta_{23}, \Delta m^2{}_{31})$ parameter space according to MINOS, T2K and a global fit including the Super-Kamiokande data. Since the

sign of $\Delta m^2{}_{32}$ is yet to be measured, both possible mass hierarchy are shown.

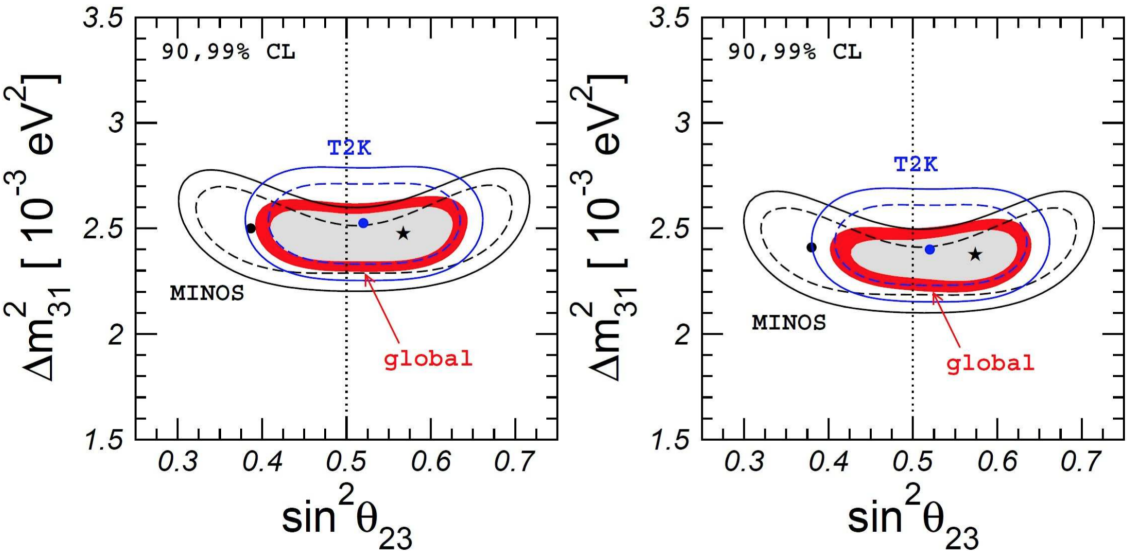

Figure 1.6: *Allowed regions contours of the* ($\sin^2\theta_{23}, \Delta m^2{}_{31}$) *space according to MINOS, T2K and global data. (Left) Normal (Right) inverted mass hierarchy. Figure from Ref. [42].*

1.4.9 Summary

Solar and Reactor based neutrino experiments give the best measured values of $\tan^2\theta_{12}$ and $\Delta m^2{}_{21}$, whereas, atmospheric and accelerator based neutrino oscillation experiments provide the best measured values of parameters $\sin^2\theta_{23}$ and $\Delta m^2{}_{31}$. However, there are still many un-answered questions that need to be answered by the current and future neutrino experiments. These questions are briefly discussed in the following.

1.4.9.1 Mass Heirarchy

Currently, the value of mass squared difference; $\Delta m^2{}_{31}$, is known but the sign of this quantity is yet unknown. In order to measure this, one can compare the ν_μ and $\bar{\nu_\mu}$ oscillations. Due to matter effects, the oscillation probability for neutrinos and antineutrinos are different, so

the long baseline experiments with their neutrino beams passing through earth can make this measurement. Although, this effect can be hard to study because of CP violation effects.

1.4.9.2 CP Violation

As discussed in the previous section, if CP symmetry is violated in neutrino sector, then the oscillation probability of $\nu_\alpha \to \nu_\beta$ will not be equal to $\bar{\nu_\alpha} \to \bar{\nu_\beta}$, however, matter effects can increase or decrease this difference. The future generation experiments, such as DUNE and so called neutrino factories, can study this with their high beam intensities and beamlines of several thousand kilometers.

1.4.9.3 Sterile Neutrinos

The results from LSND experiment in 2001 showed an access of ν_e in $\bar{\nu_\mu} \to \bar{\nu_e}$ appearance measurement. The result could not be explained in the three-neutrino oscillation formalism. As a result, a third mass splitting was considered that followed by a postulate of fourth neutrino, a sterile neutrino. Sterile neutrino does not interact via the Standard Model weak interaction but can mix with three active neutrinos. MiniBooNE result in 2013 showed partial agreement with LSND results based on two-neutrino oscillation model [43]. Several other experiments made such measurements, but currently, all the combined exclusion limits do not completely rule out the existence of sterile neutrinos. More data, covering more parameter space is needed. One of the experiments with the goal to measure ν_e excess signal is MicroBooNE at Fermilab [13].

1.4.9.4 Absolute Neutrino Mass

As discussed before, neutrino mass squared differences are known currently but the absolute masses are yet to be measured. Absolute mass of neutrino can be measured by studying the endpoint region of β-decay spectrum. Non-zero mass of neutrino implies kinematic constraints on emitted electron during the decay. For example, direct measurement of

neutrino mass can come from analyzing the very high precision electron-spectrum from β-decay of tritium. Cosmological data also provides the constants on absolute neutrino mass.

1.4.9.5 Is Neutrino Majorana/Dirac

Another question yet to be answered is the nature of neutrino. If the neutrino is a Majorana particle, then it is its own anti-particle, unlike all other fermions in the Standard Model which are Dirac particles. Neutrino-less double β-decay can be studied to answer this question, the decay can only occur if neutrinos have a non-vanishing mass and are Majorana particles.

1.5 Neutrino Scattering

Neutrinos are one of the most abundant particles in the universe but their interactions are rare; $\sigma(\nu\mathrm{N}) \sim 10^{-38}$ cm^2 as compared to $\sigma(\mathrm{pp}) \sim 10^{-26}$ cm^2. Nevertheless, all properties of neutrinos discussed in the previous section must be inferred from interactions. Depending on the neutrino energy, there are different types of neutrino interactions and the cross-section for each type of interaction is different for free and bound nucleon targets. In case of the bound nucleon target, the kinematics of the outgoing particles is effected by the properties such as nucleon Fermi momentum, binding energy, Pauli blocking and others. Furthermore, the particles produced in the interaction travel through the nuclear medium and re-interact which also changes kinematic distribution of the outgoing particles.

The simplest neutrino interaction is the elastic scattering of neutrino off of a free electron, shown in Figure 1.7. The neutrino and the electron both retain their original flavor. There is no threshold energy for this process as only the momentum and energies of the particles are redistributed. This process is exactly calculated in the Standard Model. In neutrino-nucleon scattering, the momentum transfer, Q^2, to a nucleon determines the resolving power of the neutrino. At low Q^2, a nucleon is a single entity rather than comprised of quarks, whereas, at high Q^2 the nucleon can be excited or single quarks could be resolved. In other words, the

complexity of neutrino interactions with a nucleon increases as Q^2 increases. This section gives a brief overview of the neutrino-nucleon scattering.

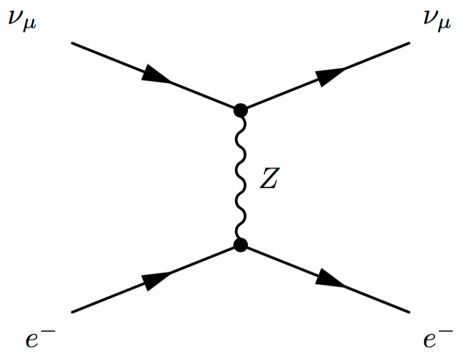

Figure 1.7: *Neutrino-electron elastic Interaction.*

1.5.1 (Quasi-)Elastic Scattering

This is the simplest interaction involving strongly interacting particles, hadrons. In elastic scattering of neutrino with a nucleon, a neutrino elastically scatters off of a nucleon and ejects it from the nucleus; the incident and the final particles are the same. In quasi-elastic scattering, the neutrino converts a neutron to a proton or an antineutrino converts a proton to a neutron (charge current). The nucleon remains intact but is ejected from the nucleus. The signature of this interaction is a charged lepton in the final state and a proton or neutron (without final state interactions). In the neutrino case, a d quark is converted to a u quark (neutron to proton), whereas, in the antineutrino case, a u quark is converted to a d quark (proton to neutron). These processes are shown in Figure 1.8 and Figure 1.9.

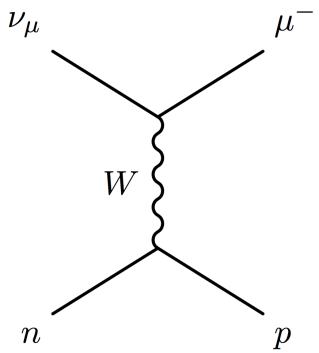

Figure 1.8: *Charge current quasi-elastic Interaction.*

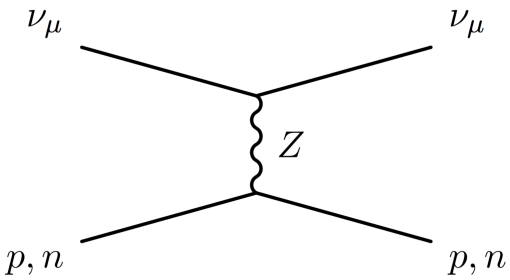

Figure 1.9: *Neutral current elastic Interaction.*

1.5.2 Resonant Scattering

As the squared momentum transfer Q^2 increases, the target nucleon can be raised to an excited state, a resonance, that decays to a nucleon and a pion. The most prominent resonance is the Δ particle, that decays quickly via strong force to a nucleon (proton or neutron) and a pion. In case of the charge current interaction, the signature of this process is a charge lepton along with a nucleon and a pion, whereas, in case of neutral current interaction, the charge lepton is replaced by a neutrino of same flavor as incident neutrino. These processes are also known as resonant single pion production. These interactions can be seen in Figure 1.10.

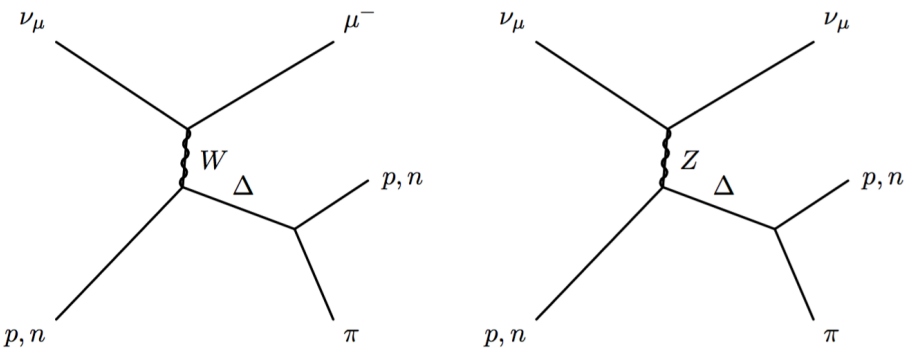

Figure 1.10: *(Left)Charge current resonant Interaction, (Right)Neutral current resonant Interaction.*

1.5.3 Coherent Scattering

In this interaction, a neutrino interacts coherently with the whole nucleus, with small Q^2. The nucleus is left in the ground state and a pion is produced in the interaction along with the charge lepton (charge current) or a neutrino (neutral current). The cross section for this interaction is very small. Figure 1.11 shows coherent scattering.

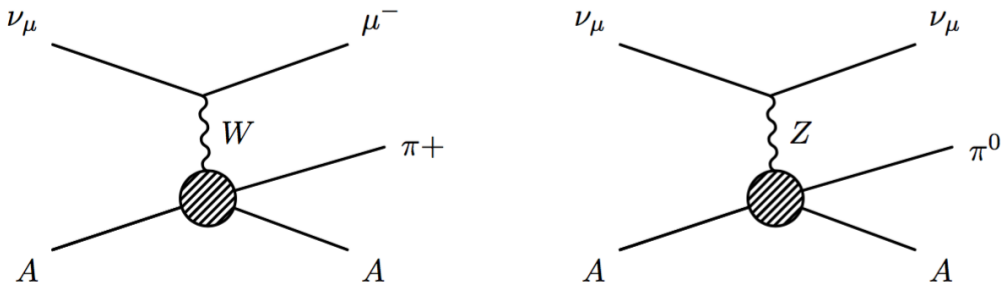

Figure 1.11: *(Left)Charge current coherent Interaction, (Right)Neutral current coherent Interaction.*

1.5.4 Deep Inelastic Scattering

In deep inelastic scattering, enough Q^2 is transferred to the nucleon that the neutrino interacts with the quasi-free quarks in the nucleon. The quark produces a shower of hadrons as it recoils from the neutrino. The final particles produced in deep inelastic interaction include nucleons, pions, strange particles and others. Figure 1.12 shows the deep inelastic interaction. A strange particle is a hadron that contains at least one s quark.

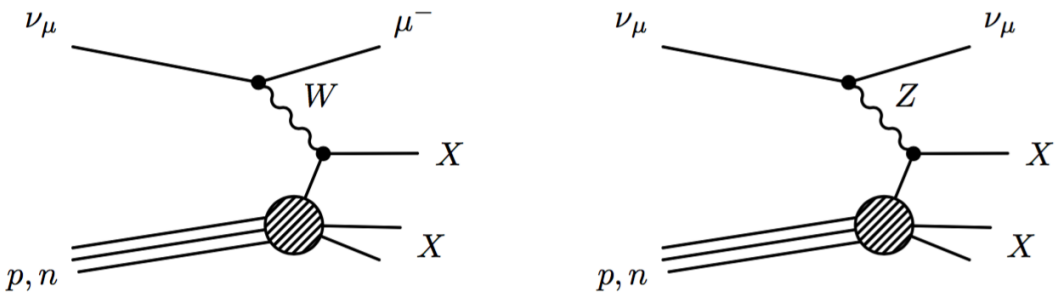

Figure 1.12: *(Left)Charge current deep inelastic Interaction, (Right)Neutral current deep inelastic Interaction.*

1.6 Charge Current Quasi-Elastic (CCQE) Scattering Theory

This section describes the mathematical formalism of charge current quasi-elastic (CCQE) scattering theory followed by the description of Cabibbo-suppressed CCQE scattering according to the NUANCE neutrino event generator [44].

1.6.1 CCQE Scattering

Charge current quasi-elastic scattering of neutrino with nucleon can be shown as the following two processes:

$$\begin{aligned} \nu_\ell + n &\rightarrow \ell^- + p, \\ \bar{\nu}_\ell + p &\rightarrow \ell^+ + n. \end{aligned} \tag{1.32}$$

These processes have been studied since long in the bubble chamber experiments in 1970's and are calculated by C. H. Llewellyn Smith in early 1970's [45].

In most of neutrino experiments, such as, LArTPC experiments, the neutrino target is usually a bound nucleon, so one can write the above processes as follows,

$$\begin{aligned} \nu_\ell + A &\rightarrow \ell^- + A', \\ \bar{\nu}_\ell + A &\rightarrow \ell^+ + A'. \end{aligned} \tag{1.33}$$

Where A is the initial state nucleus and A' is the final state nucleus plus accompanying hadron. The cross section model used in the analysis presented in this study is given by Smith and Moniz [46], where the cross section for both, free and bound nucleon is calculated. The Fermi gas model is used to calculate the effects such as Fermi motion and Pauli blocking in case of a bound nucleon target [44].

1.6.1.1 Smith-Moniz Formalism – Neutrino-Nuclei CCQE Cross Section

Assume the neutrino-bound nucleon scattering as shown in Equation 1.33 as Figure 1.13. One can write

$$q = p - p' = k_2 - k_1. \tag{1.34}$$

Here, p, p', k_1 and k_2 are the 4-momenta of initial and final nucleon and initial and final lepton, respectively. The cross section can be written as

$$d^2\sigma = \frac{{G^2}_F}{2} \frac{1}{2\pi^2} \frac{1}{2|k_1.p|} \frac{dk_2}{2\epsilon_2} \tau_{\mu\nu} W_{\mu\nu}. \tag{1.35}$$

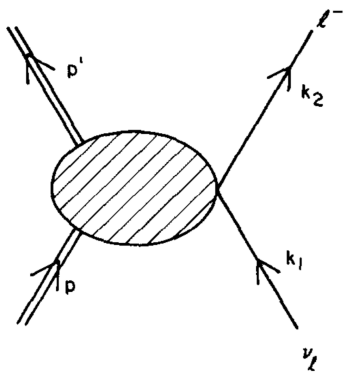

Figure 1.13: *Neutrino scattering on a nuclear target. Figure from Ref. [46].*

The leptonic tensor $\tau_{\mu\nu}$ is given by the following,

$$\tau_{\mu\nu} = 8\big[k_{1\mu}k_{2\nu} + k_{2\mu}k_{1\nu} - (k_1.k_2)\delta_{\mu\nu} - i\epsilon_{\mu\nu\alpha\beta}k_{1\alpha}k_{2\beta}\big]. \tag{1.36}$$

The most general form of hadronic tensor $W_{\mu\nu}$ that obeys Lorentz invariance is defined as,

$$W_{\mu\nu} = W_1\delta_{\mu\nu} + \frac{W_2}{m_T^2}p_\mu p_\nu + \frac{W_\alpha}{m_T^2}q_\mu q_\nu + \frac{W_\beta}{m_T^2}(p_\mu q_\nu + p_\nu q_\mu) + \frac{W_8}{m_T^2}\epsilon_{\mu\nu\sigma\tau}p_\sigma q_\tau. \tag{1.37}$$

Here, the form factor W_j depend only on the scalars q^2 and $q.p$ and the last term corresponds to vector-axial interference. m_T is the target mass. If we use $\frac{k_2}{\epsilon_2}\cos\theta = \cos\chi$, where ϵ_2 is the energy of the charged lepton and θ is the angle between the charged lepton and the incident neutrino (in the process shown in Figure 1.13), then the cross section in the lab frame can be written as,

$$\frac{d^2\sigma}{dk_2 d\Omega_2} = \frac{G^2 k_2^2}{2\pi^2 m_T}\Big\{2W_1 \sin^2(\frac{1}{2}\chi) + W_2 \cos^2(\frac{1}{2}\chi) + \frac{m_l^2}{m_T^2} W_\alpha \sin^2(\frac{1}{2}\chi) + \frac{m_l^2}{m_T \epsilon_2}(W_\beta + W_8) - 2\frac{W_8}{m_T}\sin(\frac{1}{2}\chi)\sqrt{[q^2\cos^2(\frac{1}{2}\chi) + |q^2|\sin^2(\frac{1}{2}\chi) + m_l^2]}\Big\}. \tag{1.38}$$

The sign of the last term (with W_8) will be reversed for the antineutrino reactions. The nuclei hadronic tensor components W_j, are calculated in terms of nucleon hadronic tensor components T_j as follows,

$$\begin{aligned}
W_1 &= a_1 T_1 + \frac{1}{2}(a_2 - a_3)T_2, \\
W_2 &= a_4 + \frac{2w}{|q|}a_5 + \frac{w^2}{|q|^2}a_3 + \frac{1}{2}\frac{q^2}{|q|^2}(a_2 - a_3)T_2, \\
W_\alpha &= \frac{m_T^2}{|q|^2}(\frac{3}{2}a_3 - \frac{1}{2}a_2)T_2 + \frac{m_T^2}{m^2}a_1 T_\alpha + \frac{2m_T^2}{m|q|}a_6 T_\beta, \\
W_\beta &= \frac{m_T}{m}(a_7 + \frac{w}{|q|}a_6)T_\beta, \\
W_8 &= \frac{m_T}{m}(a_7 + \frac{w}{|q|}a_6)T_8.
\end{aligned} \tag{1.39}$$

Where a_j, nuclear form factors are given as follows,

$$\begin{aligned}
a_1 &= \int d\mathbf{k} f(\mathbf{k}, \mathbf{q}, w), & a_5 &= \int d\mathbf{k} f(\mathbf{k}, \mathbf{q}, w)\frac{\epsilon_k k \cos\tau}{m^2}, \\
a_2 &= \int d\mathbf{k} f(\mathbf{k}, \mathbf{q}, w)\frac{k^2}{m^2}, & a_6 &= \int d\mathbf{k} f(\mathbf{k}, \mathbf{q}, w)\frac{k\cos\tau}{m}, \\
a_3 &= \int d\mathbf{k} f(\mathbf{k}, \mathbf{q}, w)\frac{k^2\cos^2\tau}{m^2}, & a_7 &= \int d\mathbf{k} f(\mathbf{k}, \mathbf{q}, w)\frac{\epsilon_k}{m}. \\
a_4 &= \int d\mathbf{k} f(\mathbf{k}, \mathbf{q}, w)\frac{\epsilon_k^2}{m^2},
\end{aligned} \tag{1.40}$$

and T_j; the nucleon hadronic tensor elements are given as follows,

$$
\begin{aligned}
T_1 &= \frac{1}{2}q^2(F_1+2mF_2)^2 + (2m^2+\frac{1}{2}q^2)F_A^2,\\
T_2 &= 2m^2(F_1^2+q^2F_2^2+F_A^2+q^2F_T^2),\\
T_\alpha &= -\frac{m^2}{q^2}T_1 + \frac{1}{4}T_2 + m^2F_S\big[-2mF_1+q^2F_2+(2m^2+\frac{1}{2}q^2)F_S\big]\\
&\qquad + m^2(2mF_A-q^2F_P)\big[-F_T+\frac{1}{2q^2}(2mF_A-q^2F_P)\big],\\
T_\beta &= -\frac{1}{2}T_2 + m^2F_S\big[2mF_1-q^2F_2\big] + m^2F_T\big[2mF_A-q^2F_P\big],\\
T_8 &= 2m^2F_A(F_1+2mF_2).
\end{aligned}
\tag{1.41}
$$

These nucleon form factors will be replaced by Equation 1.43 in the next section while following the Pais treatment [47] for Cabibbo-suppressed CCQE cross section calculation. The W_j are calculated for the target state which is superposition of non-interacting Fermi gases of proton and neutron with individual momentum distributions. The a_j are calculated analytically for Fermi gas model [46] and contain all the nuclear physics in the single particle momentum distributions and energies.

1.6.2 Cabibbo-Suppressed CCQE Scattering

Cabibbo-suppressed CCQE scattering can be regarded as the simplest process after CCQE scattering (expressed in Equation 1.32). The processes can occur as follows:

$$
\begin{aligned}
\bar{\nu}_\ell + p &\rightarrow \ell^+ + \Lambda^0,\\
\bar{\nu}_\ell + p &\rightarrow \ell^+ + \Sigma^0,\\
\bar{\nu}_\ell + n &\rightarrow \ell^+ + \Sigma^-.
\end{aligned}
\tag{1.42}
$$

These processes have been calculated historically by [45, 48, 49, 47] and recently by [50, 51, 52, 53]. There are large variations in the cross section models (see, for example, Figure 1.14 versus Figure 1.15 and Figure 1.16).

The processes shown in Equation 1.42 occur only for antineutrinos (restricted by $\Delta S = \Delta Q$ selection rule) and convert a u-quark to s-quark, transforming a proton into a Λ^0 or Σ^0, or a neutron to a Σ^-. Such processes are relatively rare as they are suppressed by a factor of $\sin^2\theta_c \approx 0.05$, where θ_c is the Cabibbo angle. In other words, the CCQE neutral hyperon production is $\sim \sin^2\theta_c = 0.05$ times the CCQE neutron production. Since the processes involve antineutrinos only, they can be used as 'antineutrino tagger' for the bigger neutrino experiments. The study of such reactions at low energy is interesting as hyperons do not experience Pauli blocking as compared to neutron production in CCQE (see Equation 1.33). In CCQE neutron production, when a proton is converted to a neutron, it cannot stay in the same shell in the nucleus as Pauli-Exclusion principle restricts two identical nuclear particles in a given energy state, and must have an energy above a threshold for the interaction to occur, hence the process is Pauli-blocked at low energies. Hyperons do not see this effect in the nucleus.

This study covers the detection of neutral hyperons produced by the first two reactions shown in Equation 1.42. The interaction involves u-s quark coupling via W^-, which converts a proton to a neutral hyperon; Λ^0 or Σ^0. The minimum threshold neutrino energies for Λ^0 and Σ^0 production are $\sim$ 325 MeV and 425 MeV, respectively. There is a μ^+ and a neutral hyperon (Λ^0 or Σ^0) in the final state of this interaction. Neutral particles are invisible in the detector and can be seen only if they decay to charge particles. The Λ^0 and Σ^0 baryon have masses (1115.683 $\pm$ 0.006) MeV and (1192.642 $\pm$ 0.024) MeV with the decay times of (2.632 $\pm$ 0.020) x10^{-10} s and (7.4 $\pm$ 0.7)10^{-20} s, respectively. The decay times correspond to the decay lengths, for $v < c$, of 7.8 cm and 0.022 nm, respectively. Notice that the mean decay length of Σ^0 is larger than the argon nuclear radius ($\sim 10^{-15}$ m), so it exits the nucleus before decaying to a Λ^0. The longer decay time of Λ^0 is attributed to its weak decay as compared to the electromagnetic decay of Σ^0. Λ^0 decays to $p\pi^-$ 64% of times and to $n\pi^0$ 36% of times, whereas, a Σ^0 decays to Λ^0 100% of the time; which eventually decays to two charge or two neutral particles as mentioned before. The signature of Λ^0 decay is referred

to 'vee' decay as the two charge particles make a shape of letter 'V'. The first observation of Λ^0 was by V. D. Hopper and S. Biswas in 1950 [54] in photographic emulsions.

1.6.2.1 Pais Formalism – Cabibbo-Suppressed CCQE Cross Section

To accommodate the inelasticity and the $|\Delta I| = \frac{1}{2}$ rule for these reactions, the Smith and Moniz model has been extended using the calculation by Pais [47] for such processes. The nucleon hadronic tensor elements calculated by Pais are used instead of those given by Smith-Moniz in Equation 1.41,

$$\begin{aligned} t_1 &= 2M^2 w_1, \\ t_2 &= 2M^2 w_2, \\ t_\alpha &= \frac{M^2}{2}(w_2 + w_{42} w_5), \\ t_\beta &= M^2(-w_2 + w_5), \\ t_8 &= M^2 w_3. \end{aligned} \tag{1.43}$$

where, the w_i are expressed by Pais as follows,

$$\begin{aligned} w_1 &= \frac{1}{4M^2}\left[(q^2 + M_+^2)|g_V^2| + (q^2 + M_-^2)|g_A^2|\right., \\ w_2 &= |g_A - M_- f_A|^2 + |g_V - M_+ f_V|^2 + q^2(|f_V|^2 + |f_A|^2), \\ w_3 &= -2Re g_A^* g_V, \\ w_4 &= -|g_V + M_- h_V|^2 - |g_A + M_+ h_A|^2 + (4M\nu - q^2 + 4M^2)(|h_V|^2 + |h_A|^2), \\ w_5 &= (M_+ g_V - (g^2 + M_+^2) f_V) h_V^* + (M_+ g_A^* - (q^2 + M_-^2) h_A^*) f_A \\ &\qquad + M_-(f_V g_V^* + h_A g_A^*), \\ w_6 &= 0. \end{aligned} \tag{1.44}$$

Here,

$$M_{\pm} = \sqrt{M^2 + 2M\nu - q^2} \pm M, \tag{1.45}$$

where $q^2 = -Q^2$ and $\nu = E_\nu - E_\ell$.

For the general CCQE processes shown in Equation 1.32, one can make the following substitutions,

$$2M\nu \to q^2; M_+ \to 2M; M_- \to 0. \tag{1.46}$$

Smith-Moniz's and Pais's form factors are related as follows,

$$\begin{array}{rcr} \textbf{Pais} & & \textbf{Smith-Moniz} \\ g_V & & F_1 + 2MF_2 \\ f_V & & F_2 \\ g_A & \Longleftrightarrow & -F_A \\ F_A & & F_T \\ h_A & & -F_P \\ h_V & & F_S \end{array} \tag{1.47}$$

One can substitute Equation 1.44, Equation 1.46 and Equation 1.47 in Equation 1.43 to reach the general CCQE result from Smith-Moniz for the processes shown in Equation 1.41. The cross section for the Cabibbo-suppressed CCQE processes as calculated by Pais as function of antineutrino energy is shown in Figure 1.14.

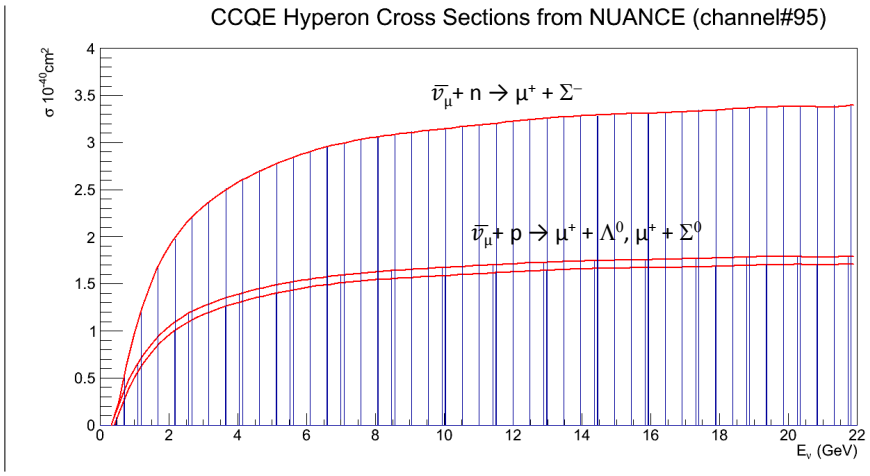

Figure 1.14: *CCQE Neutral Hyperon Production as calculated by Pais and used by NUANCE Event Generator [46, 44, 47].*

1.6.2.2 Experimental Measurements

Cabibbo-suppressed CCQE processes have been studied by bubble chamber experiments such as Gargamelle at CERN [55, 56, 57], Serpukhov SKAT [58] and BNL 7-ft bubble chamber with propane with admixture of freon, freon and hydrogen as neutrino targets, respectively. The results are based on small number of events and hence have large statistical uncertainties. Recently, more intense neutrino beams and bigger size neutrino detectors have opened up the possibility to study these reactions.

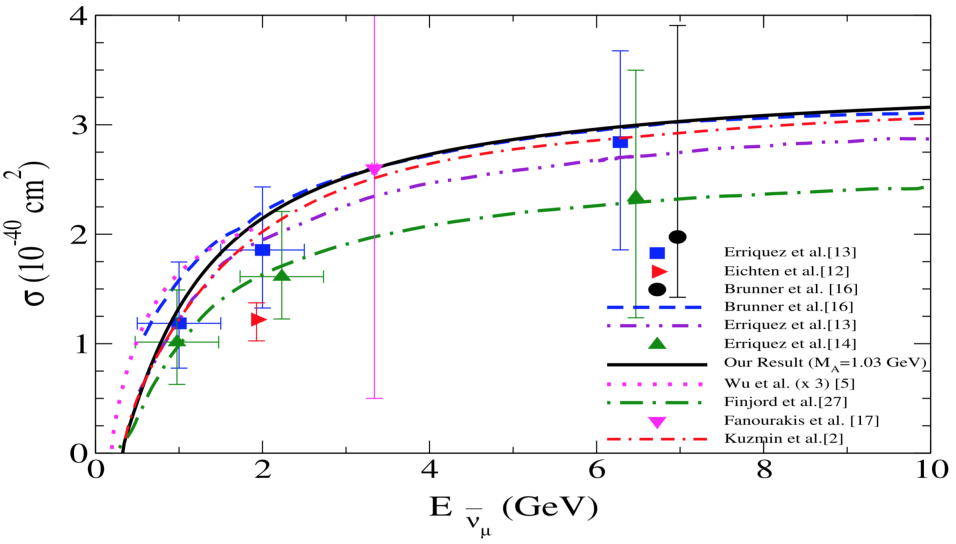

Figure 1.15: *σ versus $E_{\bar{\nu}}$, for the $\bar{\nu}_\ell + p \to \ell^+ + \Lambda^0$ process. Figure from Ref. [53].*

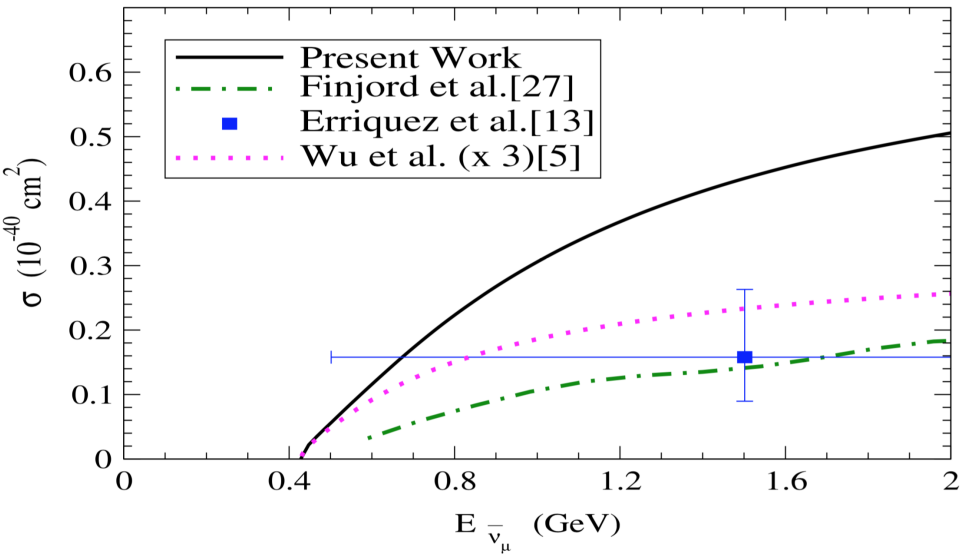

Figure 1.16: *σ versus $E_{\bar{\nu}}$, for the $\bar{\nu}_\ell + p \to \ell^+ + \Sigma^0$ process. Figure from Ref. [53].*

Figure 1.15 and Figure 1.16 show the theoretical calculation by [53] for the $\bar{\nu}_\ell + p \to \ell^+ + \Lambda^0/\Sigma^0$ processes and the corresponding experimental measurements.

1.7 Nuclear Effects

In NUANCE neutrino event generator [44], the primary interaction of a neutrino with a nucleon is given a starting position according to the measured nuclear density distribution [59]. The nucleus is considered an isoscalar sphere with radially-dependent density and Fermi momentum. Hadrons are tracked in steps of 0.2 fm in the nucleus and the interaction probability is calculated at each step using the single-nucleon cross section (pion-nucleon and nucleon-nucleon) and local density. Single-nucleon cross sections and angular distributions come from the HERA data [60, 61, 62]. Elastic interactions in the nucleus are modeled based in the global phase-shift analysis of world data [63]. Any interaction that leaves a nucleon with momentum below Fermi sea are Pauli blocked. Neutral kaons are 50% K_s and 50% K_L, whereas, K_L cross sections are calculated assuming an equal mixture of K^0 and $\bar{K^0}$ with 50% chance of generating a K_s in any interaction. K_s decays immediately. The simulation approximates the hyperons as non-interacting and non-decaying in the nucleus, whereas in the data, the hyperons produced in the nucleus can undergo elastic, quasi-elastic and charge-exchange processes with nucleons [50], such as,

$$\begin{aligned} \Lambda^0 + p &\rightarrow \Lambda^0 + p, \\ \Lambda^0 + n &\rightarrow \Lambda^0 + n, \\ \Sigma^0 + p &\rightarrow \Sigma^0 + p, \\ \Sigma^0 + p &\rightarrow \Sigma^0 + p. \end{aligned} \tag{1.48}$$

Equation 1.48 shows the elastic scattering of a hyperon with a nucleon. The first two processes (quasi-elastic) in the Equation 1.49 tend to increase the Λ^0 cross section and lower the Σ^0 and Σ^- cross section. This effect increases with the increase in the charge and mass number of the nucleus. The Λ^0 depletion is also allowed through the quasi-elastic processes, however, it is limited due to the difference in the masses. The third and fourth processes (charge-exchange) in the Equation 1.49 show the appearance of Σ^+ which

cannot be produced in CCQE processes which are studied in this thesis (see Figure 4.1, channel#95).

$$\begin{aligned} \Sigma^- + p &\rightarrow \Lambda^0 + n, \\ \Sigma^0 + n &\rightarrow \Lambda^0 + n, \\ \Lambda^0 + p &\rightarrow \Sigma^+ + n, \\ \Sigma^0 + p &\rightarrow \Sigma^+ + n. \end{aligned} \tag{1.49}$$

Also, Λ^0 production can also be higher in the data by the decay of Σ^0 in nucleus;

$$\Sigma^0 \rightarrow \Lambda^0 + \gamma, \tag{1.50}$$

but the longer mean life guarantees the decay to be outside nucleus and is ignored in the simulation. The result presented in this thesis is a production cross section of the CCQE neutral hyperons on argon target and is consistent with the NUANCE model.

Chapter 2

LArTPC Technique and Neutrino Detection

This chapter presents the working of liquid argon time projection chamber (LArTPC) and the detection of neutrino using this technique following Ref. [10], where a more detailed description can be found. The LArTPC concept was proposed in the late seventies [64, 65] and has undergone several technical developments in Europe. ICARUS T600 is the first large mass (760 tons) new generation of detector able to combine the imaging capabilities of the old famous bubble chamber with the excellent energy measurement of huge electronic detectors. ICARUS T600 at the Gran Sasso underground laboratory is used to study cosmic rays, neutrino oscillations, and the proton decay [66]. In the USA, the ArgoNeuT detector is the first LArTPC to be exposed to the neutrino beam and serves as a first step for the phased program towards the construction of a massive LArTPC detectors. The planned Short Baseline Neutrino (SBN) Program at Fermilab includes 3 LArTPC detectors; SBND, MicroBooNE, and ICARUS. MicroBooNE already started taking data in late 2015, and the other two will start in 2018 [67].

2.1 LArTPC Concept and Working

The goal of any neutrino detector is to measure the properties of a neutrino, such as its flavor and energy. This can be done by reconstructing the particles that are produced in a neutrino interaction in the detector. LArTPC offers bubble chamber quality images with fine-grained tracking, along with precise calorimetry and excellent background rejection. LArTPCs, because of these qualities, can precisely reconstruct neutrino flavor and energy and enables us to study rare phenomena. Even though a LArTPC provides precise measurements, the underlined idea and working is simple as shown in Figure 2.1.

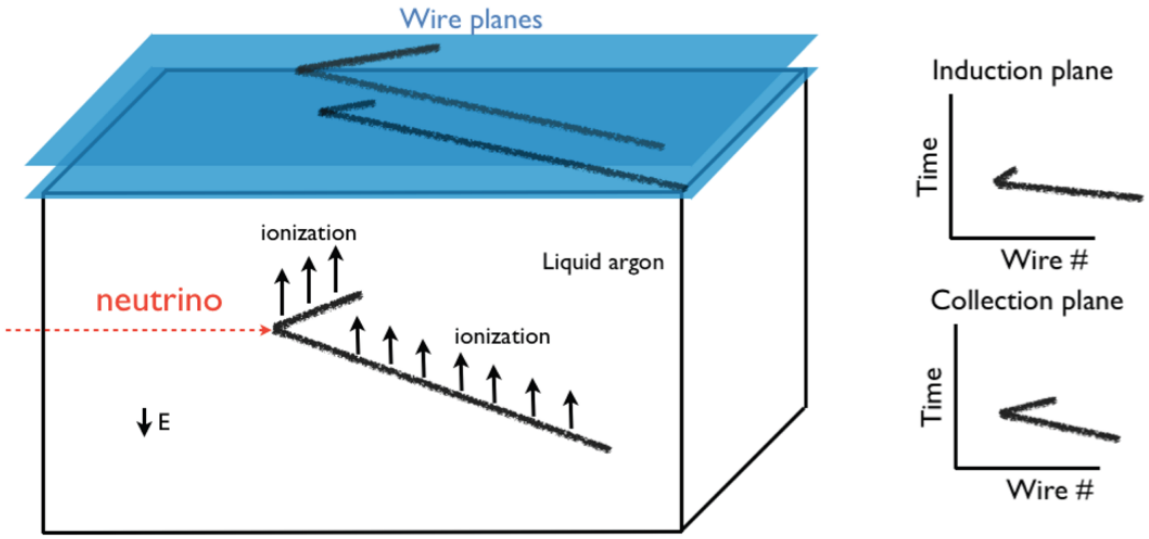

Figure 2.1: *(Left) The LArTPC concept for neutrino detection. (Right) Each wire plane provides a two-dimensional view of an event. Figure from Ref. [68].*

The time projection chamber is filled with liquid argon. When a neutrino passing through the detector medium interacts with an argon atom, it produces other particles as a result of the interaction. These particles quickly travel through the liquid argon and, if charged, produce ion-electron pairs along their way. As argon is a noble gas, this ionization is free

to drift across the chamber. The chamber sits in a constant electric field, so the ionization electron trails separate from the positive ions and drift towards the wire planes, which sense the charge induction or deposition. The wire planes are oriented at an angle to one another. The resulting signals at the wire planes are read out and analyzed. The ionization induces electric current in the 'induction' planes, and finally gets collected by the 'collection' plane. The induction plane's signal is bipolar naturally because the ionization induces current in wires in one direction when it is approaching the plane, and in the opposite direction when it is receding. The signal on the collection plane is by contrast unipolar, as the ionization approaches the plane and is collected there.

Each wire plane provides a two-dimensional view of an event. When the information from both planes is combined along with the time information, one can reconstruct the three-dimensional image of an interaction. In other words, a single plane provides the wire and time coordinates, and matching this information in time among planes gives a three-dimensional view of the neutrino event.

Knowledge of the amount of charge deposition on the wire planes allows for the calorimetric reconstruction, as the amount of the charge deposition is proportional to the amount of the energy a particle deposited in the detector. Scintillation light (with wavelength = 128 nm) is also produced during an interaction, but ArgoNeuT does not use photomultiplier tubes and hence does not detect this light. MicroBooNE makes use of the scintillation light in a neutrino event and can measure more precisely the start time of the interaction. ArgoNeuT obtains the start time of an interaction from the beam timing information. Other than this, scintillation light detection can lower the threshold of minimum reconstructable energy by a detector, and also can provide information for phenomena such as supernova burst neutrino and proton decay.

Properties of argon such as its high density, short radiation length, and high scintillation yield as compared to other noble elements makes it ideal for detecting neutrinos, (see Figure 2.2). High density gives a higher interaction rate, short radiation length helps in

	He	Ne	Ar	Kr	Xe
Boiling Point [K] @ 1atm	4.2	27.1	87.3	120.0	165.0
Density [g/cm^3]	0.125	1.2	1.4	2.4	3.0
Radiation Length [cm]	755.2	24.0	14.0	4.9	2.8
Scintillation [γ /MeV]	19,000	30,000	40,000	25,000	42,000
dE/dx [MeV/cm]	0.24	1.4	2.1	3.0	3.8
Scintillation λ [nm]	80	78	128	150	175

Figure 2.2: *Properties of the stable noble elements, relevant to particle detection. Figure credit: Mitchell Paul Soderberg.*

event containment, and lower electron diffusion helps better track resolution. Argon also withstands high voltages which also makes it a good candidate for TPC. One can see that krypton and xenon are stronger candidates for neutrino detector for the similar reasons; however, argon is relatively cheap and is easier to obtain as it is $\sim 1\%$ of the atmosphere.

A collection plane signal of a neutrino event in ArgoNeuT can be seen in Figure 2.3. The signal is a wire-time view (or in other words a two-dimensional view) with the colors representing the amount of charge deposited on a certain wire at a certain time. Also, the bottom panel in the figure shows the collection plane's signals for a certain wire as a function of time.

For minimum signal attenuation, a careful selection of electric fields in the space between the drift region and the induction plane, and also in space between induction plane and collection plane, is required. For maximum grid electron transparency for an electron traveling from space 1 with electric field E_1 to space 2 with electric field E_2, the ratio of electric field E_1 and E_2 must fulfill the transparency condition [70].

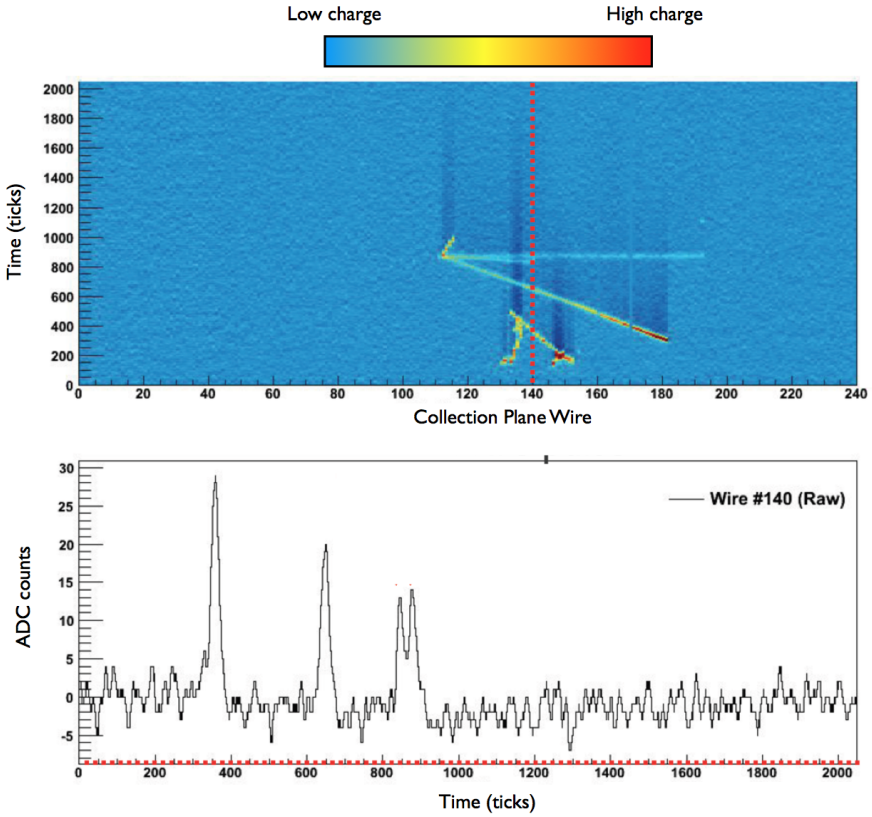

Figure 2.3: *A neutrino event in ArgoNeuT as seen in the collection plane (wire, time) view. The lower panel shows the raw ADC counts as a function of time for wire #140. Figure from Ref. [69].*

$$\frac{E_1}{E_2} > \frac{1+\rho}{1-\rho}. \tag{2.1}$$

Here $\rho = 2\pi r/a$; r is the wire radius, and a is the distance between the wires. This equation can be used for more than two wire planes. Often a 'shield' plane is also employed in addition to the induction and collection planes, separating both of them from the larger drift region. Shield plane serves as a shield for the induction and collection planes, so that they do not have induced charge before the ionization electrons enter the wire plane region. The shield plane, to serve this purpose, must satisfy the following condition:

$$\frac{a}{2\pi s} ln(\frac{a}{2\pi r}) \sim 1. \tag{2.2}$$

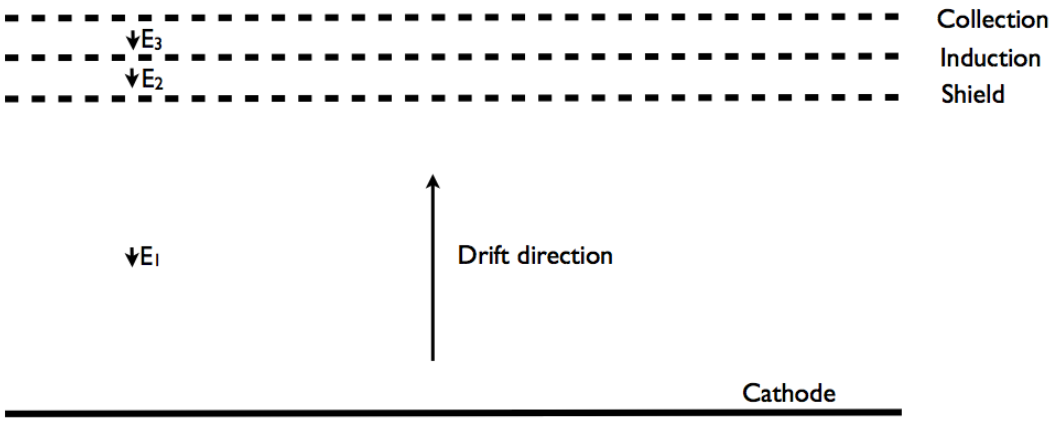

Figure 2.4: *A LArTPC's wire planes and drift regions. Figure from Ref. [10].*

Here, s is the distance between the shield plane and the next plane (induction plane). The shield plane can also help shape the field near the wire planes, and it can also serve as an additional 'wire plane' giving an additional view of an event, thus helping in the three-dimensional reconstruction of an event. ArgoNeuT uses only two planes; the induction and collection. In Figure 2.4, one can see three planes; shield, induction and collection, which make three drift regions with electric field E_1, E_2 and E_3. Here, E_1, E_2, and E_3 are selected to satisfy Equation 2.1, for a certain wire thickness and spacing. The plane spacing is chosen to satisfy Equation 2.2. Note that the collection plane carries a positive voltage, and the cathode carries a negative voltage for the ionization electrons to drift towards the wire planes.

2.2 Calorimetry - Charge to Energy

The amount of charge detected by the wires is directly proportional to the amount of the energy deposited by the corresponding particle in the detector. The stopping particles can be identified by measuring their kinetic energy (energy deposited in the detector) and the distance they traveled in the detector before stopping. Also, the energy deposited per unit length along the track (dE/dx) can be used to differentiate between particles. (see Figure 2.5).

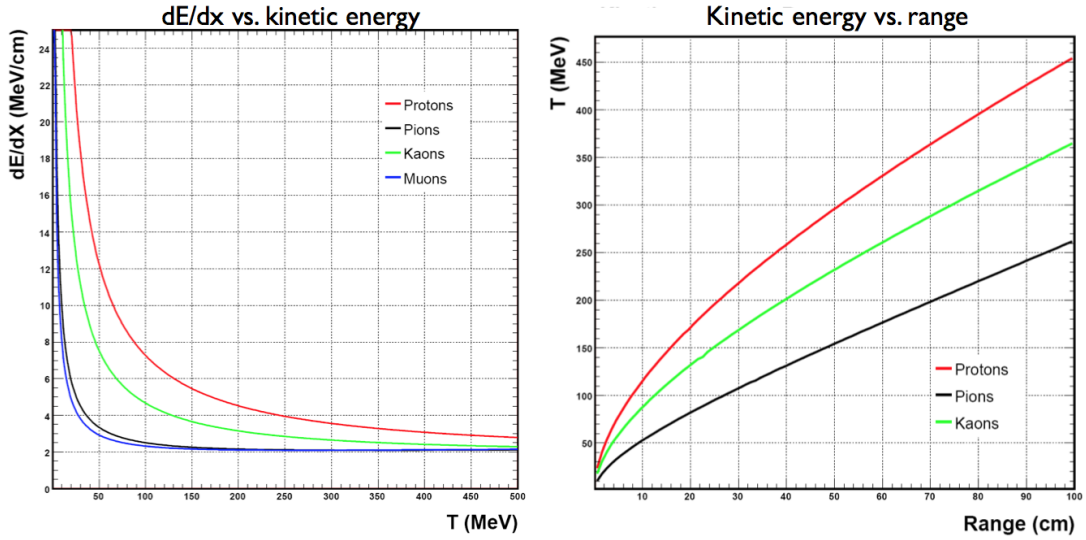

Figure 2.5: *(Left) dE/dx versus kinetic energy and (right) kinetic energy versus range for particles [71].*

The excellent differentiation power of a LArTPC for photons and electrons makes it a vital technique as compared to other traditional types of neutrino experiments. Reconstructing a photon as an electron is a dominant background for signal electron-neutrino events in oscillation experiments. In LArTPCs, energy deposited per unit length by a track produced by a photon (which converts to an electron-positron pair) is approximately double the energy deposited per unit length by a track produced by an electron. This is a very strong discrimination factor that separates photons from electrons. For this purpose, one

uses the first few centimeters of the track, that is, before the electromagnetic shower has started when a track becomes hard to characterize.

To get the energy deposition per unit track length from the charge deposition, after measuring the track orientation, one needs to know the electronic calibration factor (unit ADC/fC) to convert measured ADC counts to charge, and then normalize for the track length to get the charge per unit track length. One also needs the knowledge of charge loss along the drift due to electro-negative impurities. One also needs to take into account the recombination effect, which is the ionization electrons' recombination with ions before they were drifted by the applied electric field. This effect is called as 'charge quenching' which is the function of energy density of the charge and the applied electric field. A semi-empirical formula, Birk's Law [72], takes this effect into account and relates the charge deposited per unit length and the corresponding energy per unit length.

$$\frac{dQ_{cor}}{dx} = A\frac{(dE/dx)}{1 + K_B(\frac{dE}{dx})}. \tag{2.3}$$

Here, Q_{cor} is the corrected charge, and A and K_B are measured constants in a given electric field. The constants are measured at a number of different voltages in LArTPCs [73].

2.3 Challenges

ArgoNeuT is a research and development (R&D) project at Fermilab and serves as a first step for the US program for future kilo-ton scale LArTPCs. There are a number of associated challenges in construction and operation of LArTPCs specially when it comes to bigger sized LArTPCs. Experience gained with ArgoNeuT proved useful for MicroBooNE and will be used for the future experiments.

It should be mentioned that signal processing, devising automatic reconstruction, and analysis tasks for physics with LArTPCs also offer challenges. This is discussed in detail in Chapter 4.

2.3.1 Purity of Liquid Argon

The liquid argon used in LArTPCs needs to be thousands of times more pure than what is available commercially in order to have the minimum charge attenuation and to get the ionization electrons to drift all the way to the anode. The method of achieving pure liquid argon is discussed in Chapter 3 in detail. Argon purity is more challenging for bigger LArTPCs. For example, for a 20 Kilo-ton LArTPC, the drift distance can be estimated to be about 10m. However, the idea of segmented TPC, that is, having multiple drift regions, can make this problem manageable with 2-3 m of drift distances. However, the design of multiple drift region comes at the cost of more readout channels in a TPC.

2.3.2 Safety with Liquid Argon

Working with liquid argon in a confined space offers a safety hazard. The argon gas is a noble gas and not a direct obvious danger to human beings. However, if a few tons of liquid argon is spilled in an enclosed building in an unfortunate event, it can quickly expand to gas form and replace oxygen in the space, and would be threatening for the human beings. Devising measures to avoid such a spill underground is challenging. Filling the liquid argon in the underground detector in a safe way is also a challenge for the bigger detectors. ArgoNeuT uses measures such as gas relief lines that direct the spilled argon from underground to the ground level, oxygen deficiency alarms, slow control monitor (with pressure and temperature sensors), spill containment vessel, etc.

2.3.3 Light Collection

Liquid argon produces scintillation light which can be readily detected. This light can be used as a trigger for the start time of a neutrino interaction, which is very helpful for the non-beam-related phenomenon such as super-nova burst and proton decay. Although the start time of an event can be determined by the time of charge induced on the first

wire plane by the track, this method does not work well in the presence of, for example, cosmic rays within the drift time window. Scintillation light can also help by lowering the minimum reconstructable energy threshold of a detector. Light detection with the resolution of nanoseconds seems necessary for future LArTPC experiments.

There are two main processes of scintillation light production:

$$\begin{aligned} Ar^* + Ar &\rightarrow {Ar^*}_2 \rightarrow 2Ar + \gamma, \\ Ar^* + Ar &\rightarrow {Ar^+}_2 + e^- \rightarrow {Ar^*}_2 \rightarrow 2Ar + \gamma. \end{aligned} \tag{2.4}$$

The first process is called self trapped exciton luminescence, in which, an excited atom of argon, generated as a result of charged particle produced in the neutrino interaction, creates a molecular pair with a neighboring argon atom. Then this molecular pair de-excites and produces a photon. The second process is called recombination luminescence, in which, an argon ion, generated as a result of charged particle produced in the neutrino interaction, recombines with a neighboring argon atom to produce a molecular ion. This molecular ion then breaks apart and de-excites producing a photon. Both processes generate a photon with a wavelength of 128 nm, which is very difficult to detect using conventional photomultiplier tubes (PMTs). These tubes have low transmittance at the given wavelengths. However, a high transmittance glass can be employed, or a wavelength shifter to shift the light into the visible spectrum. MicroBooNE uses 32 8-inch PMTs for the detection of scintillation light. Each PMT is positioned behind a wavelength shifting plate.

Chapter 3

The ArgoNeut Experiment

ArgoNeuT is a research and development project at Fermilab funded by NSF and DOE. It is the first ever LArTPC exposed to a 'low energy' neutrino beam, and just the second to go in the neutrino beam ever [74], providing the neutrino interaction measurements in the 0.5 to 10 GeV range. These energies are the most relevant for the long baseline neutrino oscillation searches. ArgoNeuT serves as a first step for the construction of larger detectors, such as MicroBooNE by providing hands-on experience in operating underground liquid argon recirculation and electronics readout systems. This chapter describes the specifications of the ArgoNeuT experiment following Ref. [10, 75].

3.1 The NuMI Neutrino Beam

The neutrino beam is one of the important parts in accelerator-based neutrino experiments. ArgoNeuT is exposed to the NuMI neutrino beam which is generated from 120 GeV protons from the Main Injector at Fermilab. The production of the neutrino beam requires a series of steps (see Figure 3.1), which are described briefly in the following.

3.1.1 Cockcroft-Walton Pre-Accelerator

In the first step, H^- ions are produced by ionizing compressed hydrogen gas H_2 in the Cockcroft-Walton pre-accelertor. These ions have one proton and two electrons and are accelerated by a positive voltage to reach the energy of 750 KeV.

3.1.2 Linac

Hydrogen ions then enter the linear accelerator (Linac) which is about 160 m long, where an alternately polarized electric field accelerates the ions to the kinetic energy of 400 MeV. Before going to the next step, the negative ions H^- are stripped off of both of their electrons by passing through a carbon foil, so they become single protons.

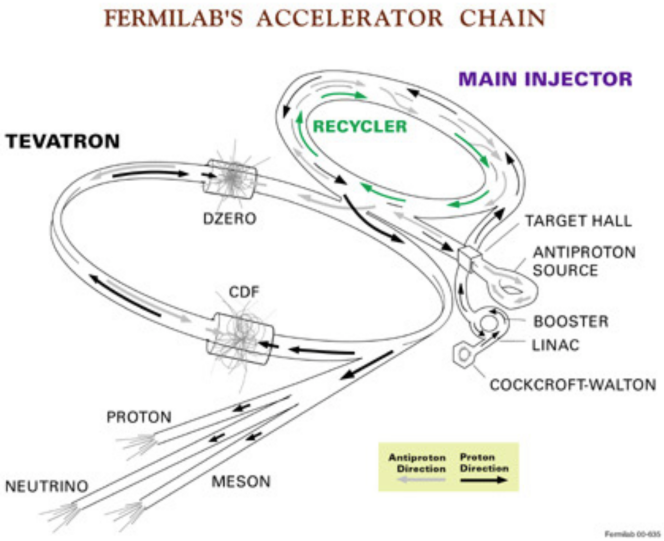

Figure 3.1: *Fermilab's accelerator chain [76]*

3.1.3 Booster

Single protons with a kinetic energy of 400 MeV then enter the Booster, which is a synchrotron accelerator operating at 15 Hz. It is 6 m underground and is 150 m in diameter.

Protons revolve about 20,000 times around the Booster, each time picking up more energy, and finally reaching 8 GeV before leaving the Booster. The booster injects a maximum of 11 batches of protons, each having about 5×10^{12} protons to the Main Injector in about 0.7 seconds.

3.1.4 Main Injector

Protons with 8 GeV of kinetic energy now enter the Main Injector, which is a larger synchrotron operating at 52.81 MHz. It accelerates them to either 120 GeV or (before the Tevatron shutdown) to 150 GeV. Protons with 120 GeV kinetic energy are either sent to the anti-proton source for the Tevatron or to the NuMI beamline. Protons with 150 GeV were sent to the Tevatron. Protons are extracted in a series of pulses, also called spills. Each spill contains 11 batches. Before the Tevatron shutdown, out of 11 batches, NuMI utilized 9 batches, with 2 going to an antiproton source for the Tevatron. After the decommissioning of the Tevatron in 2012, all 11 batches are now delivered to NuMI. Filling the Main Injector with 11 batches takes 0.73 s (1/15s/batch $\times$ 11 batches). They are then accelerated to 120 GeV (from 8 GeV), which takes about 1.5 s. Thus, the Main Injector's cycle time is 2.2 s. Typical extracted intensity of the NuMI beam is about 4.2×10^{13} protons/spill [77].

3.1.5 NuMI Beamline

The NuMI beam is bent downwards at 3.3^0 to point at the MINOS far detector in Soudan, Minnesota. The proton beam from Main Injector hits the graphite target which is placed at 350 m from it [78, 79, 80]. The target is composed of 47 rectangular segments, each 20 mm in length, 6.4 mm in width, and 15 mm in height. The spacing between two neighboring segments is 0.3 mm making the total length of the target equal to 95.4 cm, which corresponds to 1.9 proton-carbon hadronic interaction lengths. Two water-cooled stainless steel tubes run at the top and bottom of each segment. The size and design of the target are selected to maximize the pion production and minimize their re-interaction in the target at manageable

thermal conditions. Figure 3.2 shows a longitudinal cross-section of the NuMI beam target and Figure 3.3 shows the relative positioning of the target and the horn system including the possible trajectories of the particles.

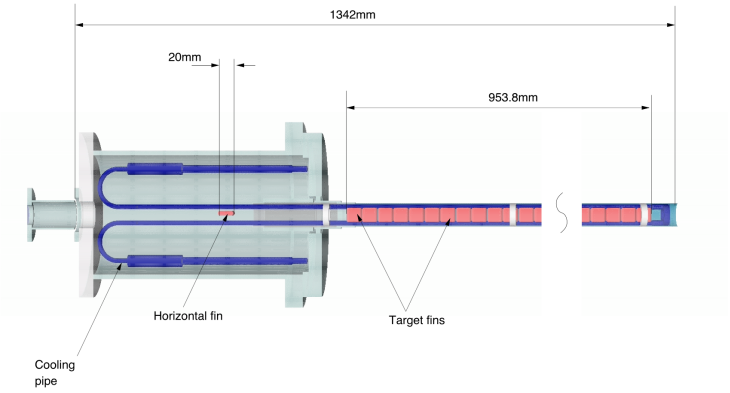

Figure 3.2: *Longitudinal cross-section of the NuMI graphite target. Figure from Ref. [80].*

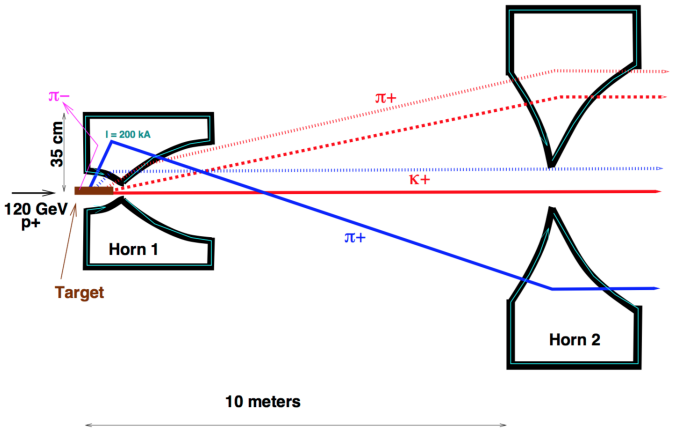

Figure 3.3: *Possible trajectories of the hadrons passing through the two horns. Particles underfocused or overfocused by first horn are further focused by the second horn. Figure from Ref. [80].*

The proton-carbon interaction produces a variety of particles, shown below

$$p + C \rightarrow \pi^{\pm}, K^{\pm} + X. \tag{3.1}$$

These particles are focused or defocused by two magnetic horns with a 30 kG toroidal field. For the low energy configuration of NUMI beam, the graphite target is partially enclosed in the first horn, 50.4 cm covered by the 3.3 m long horn [80, 81]. A second horn, 3.58 m long, is placed about 10 m downstream of the first horn. In forward horn current mode (FHC), the horns focus π^+, which produce primarily a muon neutrino beam ($\pi^+ \rightarrow \mu^+ + \nu_\mu$). If the current is reversed in the horns, π^- will be focused instead and the beam produced will have enhanced antineutrinos.

$$\pi^{+(-)} \rightarrow \mu^{+(-)} + \nu_\mu(\bar{\nu_\mu}). \tag{3.2}$$

Note that the intensity of antineutrinos in a beam will always be smaller than neutrinos because the π^- production rate is smaller than that of π^+ due to charge conservation.

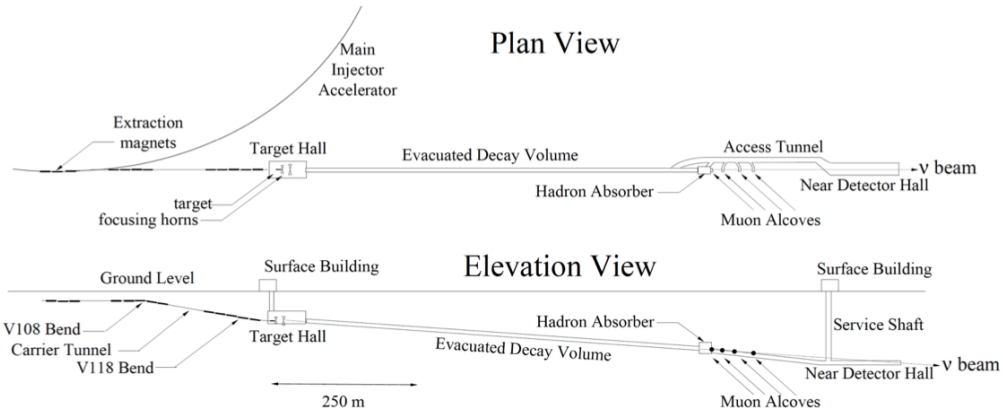

Figure 3.4: *A plain and elevation view of the NuMI beamline. ArgoNeuT was located in the near detector hall and was accessed via the service shaft. Figure from Ref. [80].*

All the particles produced in the proton-carbon interaction at the target, including pions and kaons, travel through a helium filled steel decay pipe, which is 675 m long and 2 m in diameter. This length is equivalent to the decay length of a 10 GeV pion. Here, almost all the hadrons decay into neutrinos. The hadron monitor downstream of the decay pipe detects

any undecayed hardons. The hadron monitor is composed of a set of helium ionization chambers, which detect charged particles via ionization and the information collected is used for beam monitoring [82]. The beam now travels through the hadron absorber (made of steel/aluminum/concrete) which is thick enough to stop all hadrons that have not yet decayed. At this point, the beam is composed of muons and neutrinos, which now enters 240 m of rock, where all muons are stopped, and only neutrinos are left. The beam now enters the MINOS ND hall where ArgoNeuT is situated, a total of 1 km from the NuMI target. There are three ionization chamber muon monitors which monitor the flux and orientation of the muons. The first is placed just after the absorber, whereas, the second and third are placed 12 m and 30 m downstream of the first, respectively. The information from the muon monitors is used to predict the pion and kaon spectrum and also to estimate neutrino and antineutrino spectrum in the beam. A schematic diagram of the NuMI beamline along with plain and elevation view can be seen in Figure 3.4, 3.5.

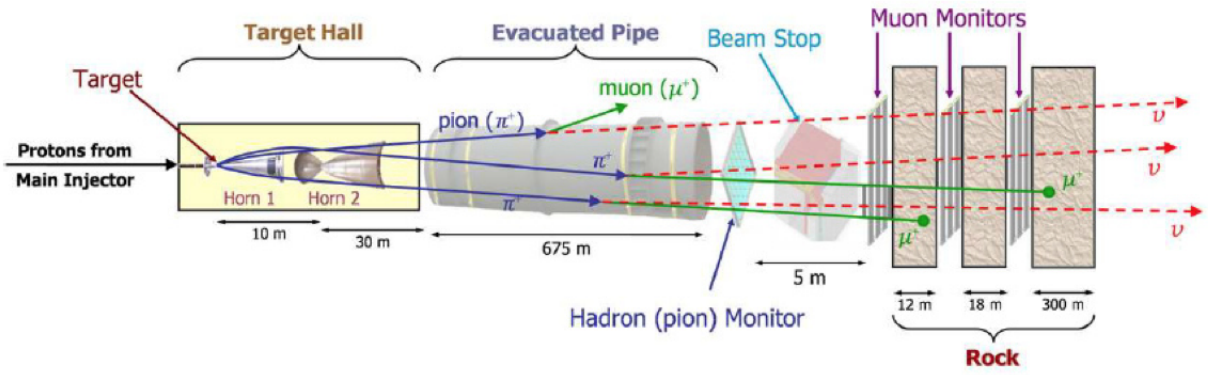

Figure 3.5: *Elevation view of the NuMI beamline. 120 GeV protons from FNAL Main Injector enter from the left. Figure from Ref. [80].*

The relative placement of the target and horns, and the magnitude of horns current (and the consequent magnetic field) alters the beam energy spectrum. The NuMI target is placed on rails and can be moved with respect to the horn system. Higher energy pions

have a shallower angle due to the lorentz boost, and they are slightly focused by the horn system. Inserting the target slightly inside the horn will focus higher angle, lower energy pions towards the decay pipe. This creates a lower average neutrino energy beam. The NuMI beam has three energy configurations, low, medium and high (see Figure 3.6). All of the ArgoNeuT physics run was in the low-energy configuration.

In neutrino mode, the NuMI beam is composed of 91.7% ν_μ, 7% $\bar{\nu_\mu}$ and 1.3 % $\nu_e + \bar{\nu_e}$. In antineutrino mode, the beam is composed of 39.9% $\bar{\nu_\mu}$, 58.1% ν_μ and 2% $\nu_e + \bar{\nu_e}$ [83].

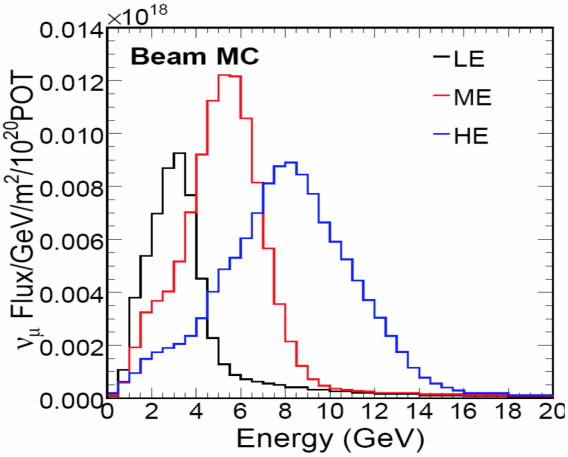

Figure 3.6: *Neutrino energy spectra at 1040 m from the NUMI target with 10 m horn separation. Target inside the horn (LE), or retracted 1 m (ME), or 2.5 m (HE). Figure from Ref. [84].*

3.2 The Physics Run

ArgoNeuT started with the cosmic ray commissioning run on the surface in summer 2008 in the Proton Assembly Building (PAB) at Fermilab, and later started its operation underground with the cosmic ray and beam neutrino commissioning run in Spring 2009 in MINOS near detector (ND) hall. The commissioning runs helped with various aspects of the experiment such as dead or noisy wires, low purity, poor recirculation rate, etc.

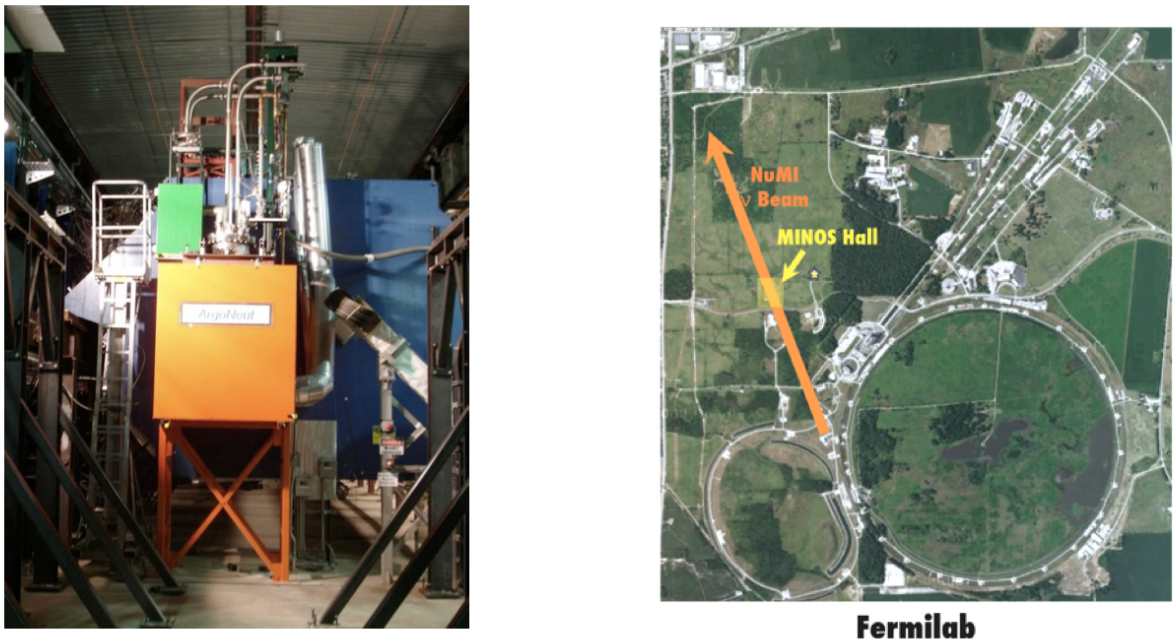

Figure 3.7: *(Left) The fully instrumented ArgoNeuT detector in the beamline. (Right) An aerial view of Fermilab showing NuMI beam and MINOS hall location. Figure from Ref. [75].*

ArgoNeuT's physics run began in September 2009 after the Fermilab accelerator complex summer shutdown was over. ArgoNeuT was situated at about 1.5 m upstream of MINOS ND [85]. Figure 3.7 and Figure 3.8 show the ariel view of the Fermilab and MINOS ND Hall and the position of ArgoNeuT in the MINOS ND hall. The general specifications of the ArgoNeuT can be seen in the table in Figure 3.9. During the operation of ArgoNeuT, The Minerva experiment [86] was installed just upsteam of ArgoNeuT.

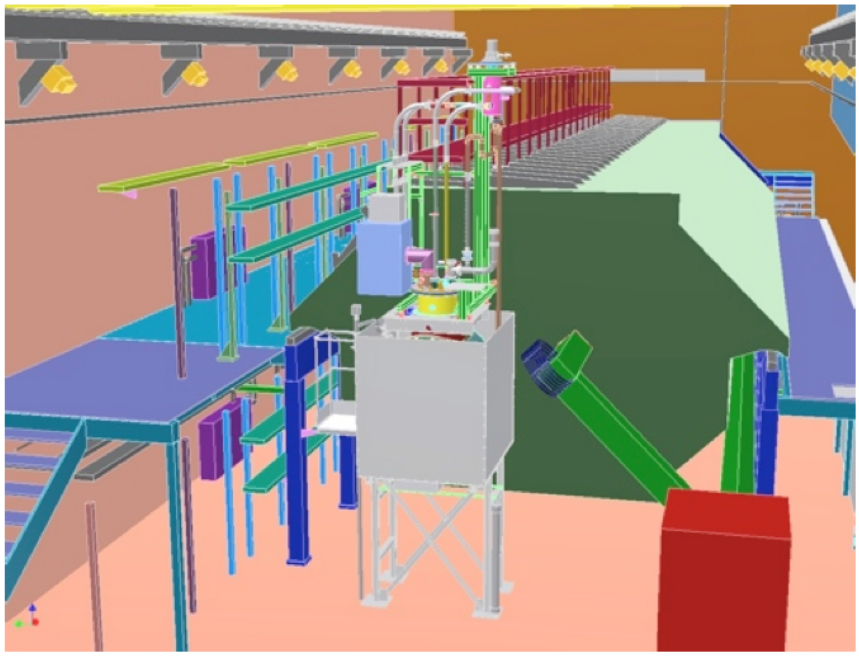

Figure 3.8: *The position of ArgoNeuT in MINOS near detector hall. ArgoNeuT, inside the gray box, can be seen just upstream of the MINOS near detector. Figure from Ref. [75].*

Cryostat volume	550 liters
TPC volume	175 liters
# Electronic channels	480 (240/plane)
Wire spacing	4 mm
Electronics style (temperature)	JFET (293 K)
Max. drift length (time)	47 cm (~330 μs)
Light collection?	No

Figure 3.9: *ArgoNeuT specifications*

ArgoNueT's physics run concluded in late February 2010. In its more than five month run, it took neutrino-mode beam data for about two weeks, and antineutrino beam for about

four and a half months. The entire run was in the 'low-energy' NuMI beam configuration, and the detector collected a total of about 1.335×10^{20} protons-on-target (POT). Out of this total, about 0.1×10^{20} were in the neutrino mode and about 1.25×10^{20} in the antineutrino mode. The uptime for the experiment in terms of POT delivered was about 86%, which included the two-week downtime in October 2009 because of a commercial cryocooler failure. Figure 3.10 shows the POT received as a function of time for ArgoNeuT. Excluding the cryocooler failure time, the uptime for the experiment was about 95% for the whole physics run. The MINOS near detector was operational for about 90% of the ArgoNeuT's physics run.

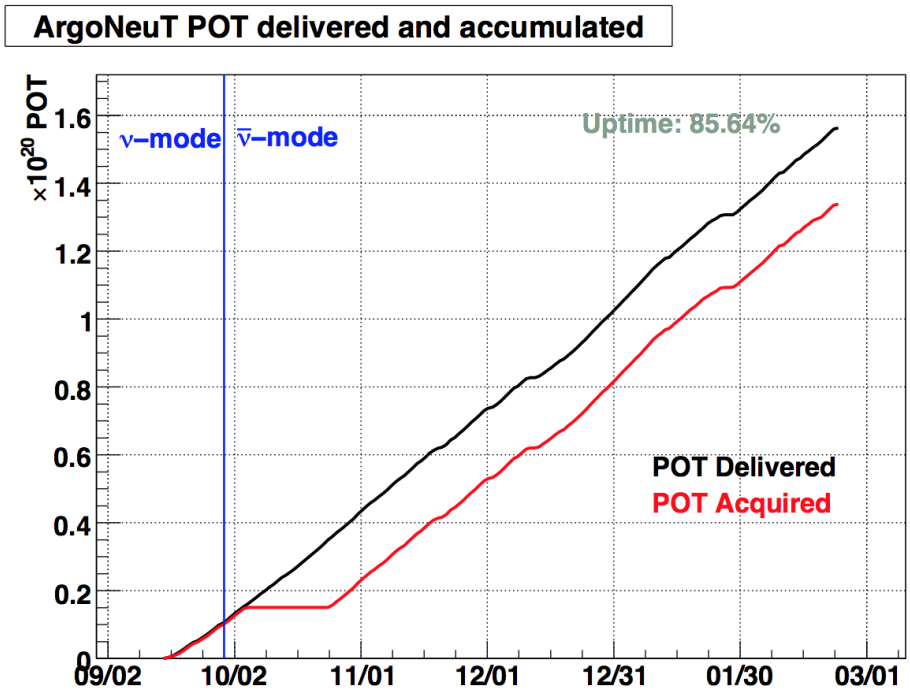

Figure 3.10: *The ArgoNeuT physics run in terms of delivered/acquired protons on target (POT) as a function of date, spanning 2009/2010. The ∼2 week downtime in October was due to a cryocooler failure. Figure from Ref. [75].*

3.3 The Detector

3.3.1 Cryostat anad Cryocooler

ArgoNeuT consists of an inner and outer cryostat, which are cylindrical in shape and have convex end-caps. The liquid argon is contained in the inner cryostat, which is made of stainless steel with a volume of 550 litres. The length and diameter of the inner cryostat are 130 cm and 72.6 cm, respectively. It is surrounded by a thick layer of vacuum insulation that is created between the inner and the outer cryostat. It was kept at a pressure of 10^{-3} - 10^{-4} torr for the full physics run. The outer cryostat has a length of 163 cm and diameter of 106.7 cm. The geometric axis of the cryostat is horizontal and is aligned with the NuMI beam axis.

The cryostat has a chimney located on top of it which is partially vacuum jacketed. It has multiple functions, including providing access to the signal wires of the TPC, internal instrumentation and holding the pipes for the re-circulation and high voltage feedthrough.

A single stage commercial cryocooler, a copper heat exchanger, and helium-based compressor keep the argon in the liquid state at a constant temperature of 88 K inside the cryostat. The liquid argon that boils off goes vertically up about 3 m above the cryostat to the cryocooler, is re-condensed, and sent back to the liquid argon volume at the bottom of the cryostat passing through one of the three pipes and a vacuum insulated pump. Out of three pipes, two have argon filters installed, whereas, one is a bypass pipe, (see Figure 3.15). On rare occasions, the re-condensed argon is forced through the by-pass pipe. Usually during the re-condensation, the bypass is closed, and the liquid argon uses one of the pipes with a filter. The whole system of filters and pipes is vacuum insulated.

A number of temperature and pressure sensors installed on the inner and outer cryostat, cryocooler, and filters along with the heaters throughout the volume make a feedback loop. This loop is controlled by the slow control software to maintain a constant temperature and pressure along with a constant re-circulation rate. If the pressure decreases below 2.0

PSIG, heaters attached to the cryocooler starts and its cooling power would be reduced. On the other hand, if the pressure increases this value, the heaters will automatically be dialed down, and the cooling increases. A screenshot of remotely controllable slow-control software for ArgoNeuT experiment is shown in Figure 3.11.

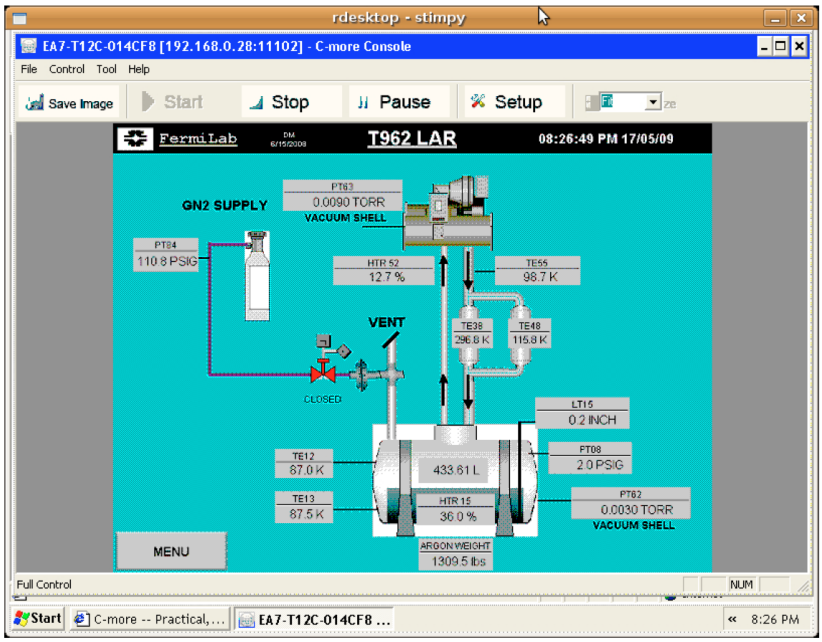

Figure 3.11: *A screenshot of the remotely controllable cryosystem monitoring software. Figure from Ref. [75].*

There are relief lines for the argon to expand and escape safely in case of boiling. All of the relief lines go to the common vent pipe, which runs up to the ground surface from the MINOS ND hall. In the case of any major accident, the outer cryostat and surrounding containment vessel, see the orange box in Figure 3.7, (which is equipped with oxygen deficiency sensor and fans) serve as containers for the spilled liquid argon.

3.3.2 Time Projection Chamber

The ArgoNeuT time projection chamber (TPC) is rectangular in shape with dimensions $47.5 \times 40 \times 90$ cm^3 ($\sim$ 175 liters). It sits inside the inner cryostat. The box of TPC is

made of G10, and all the inner conductors are made of copper. The longest side of the TPC is horizontal to the ground and is approximately parallel to the beam axis, whereas, the ionization electron's drift direction is perpendicular to the beam. The maximum drift distance is 47.5 cm, which is the distance between the negative cathode and the first wire plane which is grounded. ArgoNeuT has three wire planes, the first one, called the 'shield plane', is closest to the cathode, and has 226 wires that are at 90^0 to the beam axis. This plane serves to shape the electric field near the anode and also prevents the induction of current on the two outer planes due to drifting ionization electrons through the TPC. In principle, this plane can also serve as an additional readout plane, but in ArgoNeuT it is not instrumented. The second plane, with 240 wires oriented at $+60^0$ with respect to the beam axis, is called the 'induction plane'. The third plane, with 240 wires oriented at -60^0 with respect to the beam axis, is called the 'collection plane'.

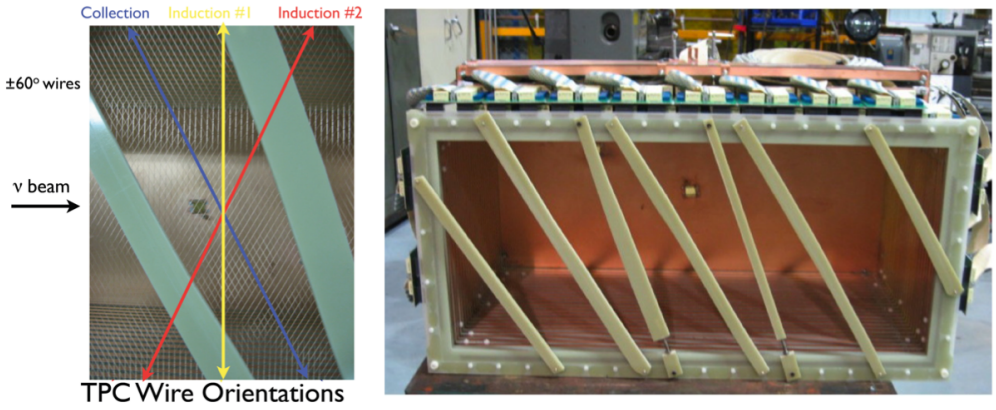

Figure 3.12: *(Left) The orientation of the ArgoNeuT TPC's wire planes. (Right) The fully assembled TPC. Figure from Ref. [10].*

The signal is produced once the ionization electrons traveling from the drift region cross the shield plane. At this time, a current is induced in the induction plane in one direction, and, as the ionization electrons pass the induction plane and move away from it (towards the collection plane), a current in the opposite direction is induced in the induction plane.

Hence, the induction plane's signal is a bipolar pulse. The ionization electrons finally get collected at the collection plane producing a unipolar signal there. The spacing between the wires in each plane in 4 mm and the spacing between the planes is also 4 mm. The wire planes and fully assembled TPC can be seen in Figure 3.12.

Figure 3.13: *A look inside the TPC. The solid copper sheet is the cathode plane and the copper strips lining the TPC are the field cage rings. The TPC frame (i.e. what the copper is attached to) is composed of G10. Figure from Ref. [75].*

There is a constant electric field of 500 V/cm throughout the drift region of the TPC. There are 23 copper field rings placed 1 cm apart, each 1 cm wide, along the edge of the TPC, from the cathode to the first wire plane. A resistor chain through each field ring from the -25 kV cathode ensures a uniform electric field throughout the TPC. The interior of the TPC can be seen in Figure 3.13. The fully instrumented TPC ready to be inserted into the inner cryostat can be seen in Figure 3.14.

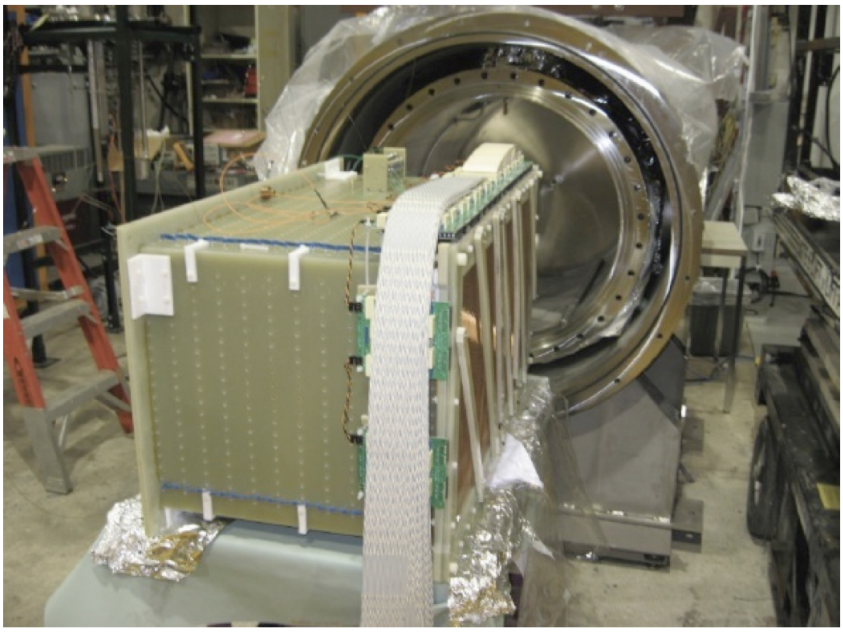

Figure 3.14: *The fully instrumented TPC ready to be inserted into the ArgoNeuT inner cryostat. Figure from Ref. [75].*

3.3.3 Purification System

It is crucial in a LArTPC experiment that the liquid argon is kept pure so that the ionization electrons can reach the wire planes with minimum loss. Electronegative impurities in the liquid argon cause the charge attenuation during the drift. The increase in concentration of impurities decreases the electron lifetime τ_e, for example, for the oxygen, $e^- + O_2 \rightarrow O_2{}^-$,

$$\frac{1}{\tau_e} = k_e[O_2]. \tag{3.3}$$

Here, $[O_2]$ is the oxygen-equivalent concentration representing the total concentration of electro-negative impurities. It is expressed in the unit of parts-per-billion (ppb). k_e is the rate constant of the electron attachment process to electro-negative impurities, which depends on the applied electric field in the TPC. For example, for an electric field of 0.5

kV/cm, $k_e \simeq 3.1$ ppb^{-1}ms^{-1} [87], the drift velocity of electrons corresponding to this electric field is about 1.6 mm/μs. Now, for the drift distance of 47.5 cm in ArgoNeuT, the drift time is 294 μs and the electron lifetime needs to be 425 μs for about 50% of charge attenuation, which corresponds to the impurity concentration of about 0.8 ppb. Commercially available liquid argon has few-parts-per-million oxygen-equivalent concentration. However, ICARUS [88] and FNAL [89], using filtration methods, have shown the electron lifetime in excess of 10 ms.

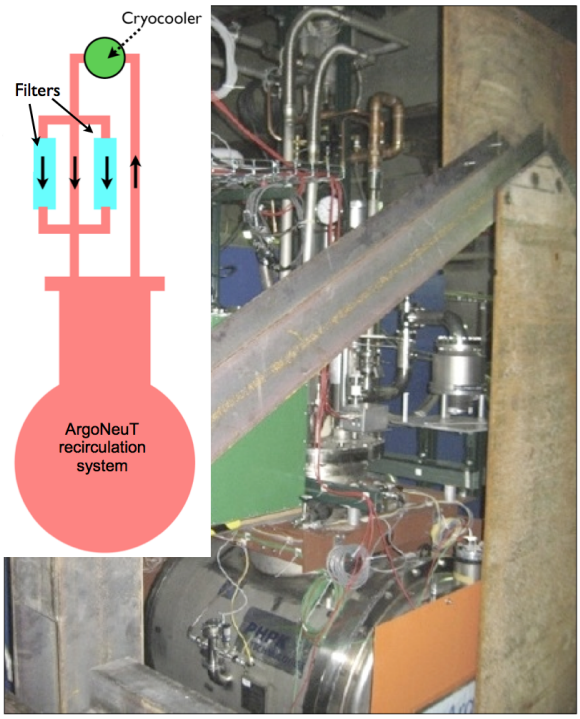

Figure 3.15: *The ArgoNeuT experiment during the physics run. (Inset) A drawing of the fully contained ArgoNeuT recirculation system featuring a cryocooler and two liquid argon filters. Argon gas goes up to the cryocooler and liquid argon comes back down through the filters before returning to the cryostat. Figure from Ref. [10].*

The filtration technique used by the ArgoNeuT experiment is based on the work pioneered by the ICARUS collaboration [90]. The ArgoNueT filters are made of activated-copper-coated alumina granules [91] inside of a flange cylindrical nipple with steel caps on

each side. The steel caps allow the liquid argon to flow through while keeping the granules inside of the filter. Each filter, having a 2.5 inch diameter and 24 inches in length, corresponding to about 2 L of volume, was wrapped in about 8 inches of fiberglass for insulation. The filters are re-insulated by a weak vacuum of 100-200 torr in the recirculation system and are installed just downstream of the cryocooler in the ArgoNeuT's closed loop recirculation system. Because of their porous structure, O_2 absorption is very large, as well as H_2O absorption via molecular trapping. The filter's efficiency reduces with time, as it gets saturated with electronegative impurities and the electron lifetime decreases (as measured by the purity monitor). A dew point monitor senses the concentration of water vapor in the argon exiting the filter, which serves as an effective status indicator for off-line regeneration of the filter. When a filter gets saturated, the circulation is switched to the other filter, and the saturated filtered is regenerated, see Figure 3.15.

The argon that boils off of the liquid argon surface, goes up to the cryocooler and gets condensed there. In the liquid form, it is pushed by gravity and pressure to pass through the filter, finally entering the cryostat at the bottom. The recirculation flow rate of the system is about 1.6 L/hr/L (LAr volume per unit time per unit volume of the filter), which corresponds to the full volume (about 550 L) recirculation every 7-8 days. Further detail about ArgoNeuT filtration method can be found in [89].

3.3.4 Purity Monitor

The purity monitor in ArgoNeuT is installed just on top of the TPC inside the cryostat. It monitors the recirculation system and allows the instantaneous determination of the liquid argon purity, although with high systematics. A number of measurements over the course of days can determine the general trend and the rate of the purity (increasing or decreasing). These measurements also help with filter issues and also determine if the initial argon fill was successful.

A schematic diagram of purity monitor is shown in the Figure 3.16. It is designed based

on the Ref. [92]. The purity measurement process starts with shining light from a Xenon flash lamp that is outside the cryostat to the inside via optical fibers which are pointed towards the gold photocathode of the purity monitor. The photoelectrons from the photon-gold interaction drift through the field cage of the purity monitor (about 100 V/m) and are detected at anode about 10 cm away. Comparing the signals from cathode and anode using an oscilloscope allows to determine the level of ionization attenuation across the drift distance. If the purity is infinite (infinite electron lifetime), the signals from the cathode and anode would appear to be equal and opposite after accounting for a slightly different electronic readout response of the cathode and anode.

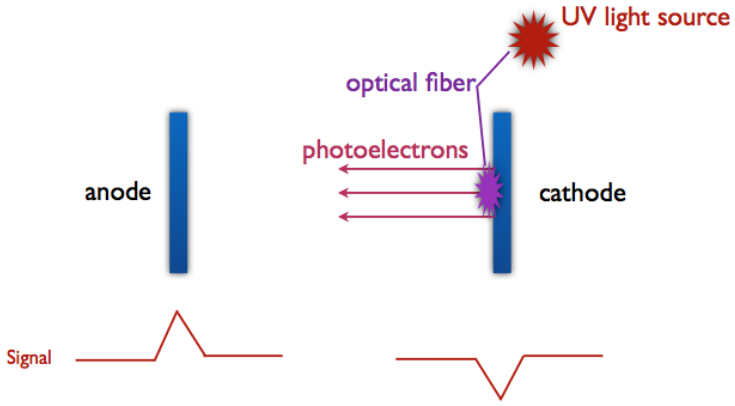

Figure 3.16: *The purity monitor concept. The cathode and anode signals, separated in time, are compared in order to determine the electron lifetime, a measure of purity, of the liquid argon. Figure from Ref. [10].*

The electron lifetime τ and electron drift time are related by the following:

$$\frac{Q_{anode}}{Q_{cathode}} = e^{-t/\tau}. \tag{3.4}$$

Where Q_{anode} and $Q_{cathode}$ are proportional to the anode and cathode pulse heights respectively. A purity monitor oscilloscope automatically determines the electron lifetime given the electron drift time using a program that employs peak-finding techniques for the

signal of the anode and cathode. The program fits the exponential decay to the signal in order to account for the electronics signal response.

The electronegative impurity concentration in the liquid argon can be written as [87]

$$\frac{d[e]}{dt} = -k_s[S][e]. \tag{3.5}$$

Here, $[S]$ is the electronegative impurity concentration, $[e]$ is the electron concentration, t is time, and k_s is the attachment rate constant for electrons.

The solution to the above equation can be written as

$$[e(t)] = [e_0]e^{-k_s[S]t}, \tag{3.6}$$

or

$$\frac{Q_{anode}}{Q_{cathode}} = e^{-k_s[S]t}. \tag{3.7}$$

Here, after accounting for a few conversion factors, Q_{anode} and $Q_{cathode}$ correspond to $[e_0]$ and $[e_t]$. Now, one can solve the two equations and get a relation between the electron lifetime and electronegative impurities as follows

$$[S] = \frac{1}{35k_s\tau}. \tag{3.8}$$

The unit of $[S]$ is usually a molar fraction. For liquid argon, it is 35 mol/L (or e.g. ppt), and the unit of τ is seconds. An electron lifetime of 750 μs (typical for ArgoNeuT in neutrino-mode run) corresponds to an oxygen-equivalent electronegative impurity concentration of 400 ppt.

3.3.5 Electronics Readout

There are three planes in ArgoNeuT, out of which two are instrumented to read the electronic signals of the charge deposition by the drifting ionization electrons. These planes are called the 'induction' plane and 'collection' plane. The un-instrumented plane is called the 'shield plane'. The induction and collection planes each have 240 wires which are made of Beryllium-Copper Alloy #125 and have a diameter of 0.006 inches. The shield plane has 226 wires. The bias voltage distribution cards (BVDCs) provide the filtered voltage to the wire planes with a 100 MΩ resistor by a Lecroy DC power supply. A capacitor is connected in series with the signal to decouple the DC bias voltage from the AC signal output. Each BVDC is connected to 24 TPC wires and connects to the wire frame with two 12 pin connectors. Each BVDC sends the output signal to the feedthrough circuit board, about 9 feet away, via ribbon cables. The signal from the feedthrough is sent to a dual FET charge integrating amplifier and then through a series of high and low pass filters. The final amplified and filtered signal is now sent to a set of 32 channel ADF-2 modules for digitization, which samples the waveform at 198ns/sample. Once the DAQ system is triggered by the NuMI beam spill clock, each channel records 2048 ADC samples with a 10-bit resolution. The total readout time for a single trigger or a single beam spill is about 400 μs which is higher than the total drift time in TPC (333 μs). This allows pre/post sampling and helps in removing spurious tracks (background) that originate outside the beam spill window. Figure 3.17 shows the ADF2 module, FET charge integrating amplifier with filters and BVDC, and Figure 3.18 shows ArgoNeuT's power supply and the shield cage for the feedthrough and preamplifiers.

3.3.6 MINOS Near Detector

MINOS is a long-baseline neutrino experiment with near and far detectors exposed to the NuMI neutrino beam. The MINOS ND sits at Fermilab 100 m underground, just upstream of ArgoNeuT, whereas, the far detector is 735 km downstream in the Soudan Mine in

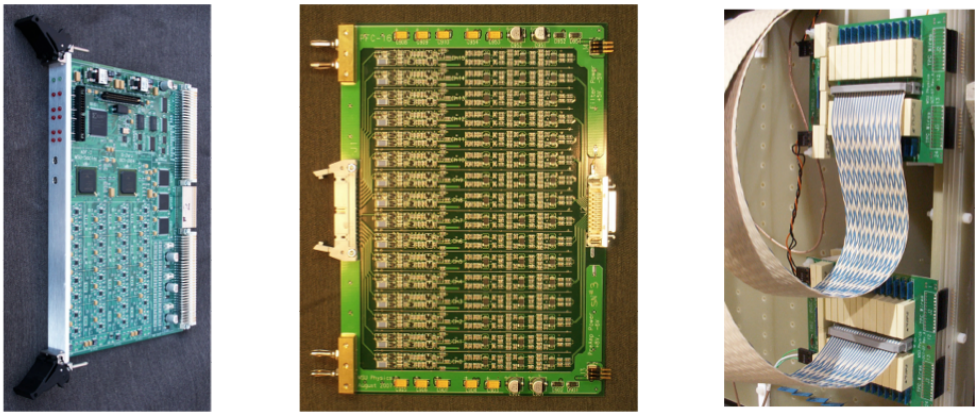

Figure 3.17: *(Left) An ADF2 digitizer card, which samples at 5 MHz (2048 samples/channel). (Middle) The FET preamplifier and filters. (Right) A set of bias voltage distribution cards. Figure from Ref. [75].*

northern Minnesota. ArgoNeuT uses the MINOS ND measured values of momentum and charge of muons exiting its TPC and entering the MINOS ND; therefore, MINOS ND is briefly discussed here.

The MINOS near detector is a 980 ton magnetized steel and scintillator tracking calorimeter. The detector with a sandwich design of alternating layers of steel and scintillator is a 3.8 m high and 4.8 m wide squashed octagon with a length of 16.6 m. There are 282 steel planes in the detector, each 2.54 cm thick and attached with 1 cm thick plastic scintillator. Each pair of steel and plastic scintillator is separated from the adjacent pair by 2.54 cm. Each layer of scintillator is rotated by 90^0 with respect to the previous one to help with a three-dimensional event reconstruction. The NuMI beam is horizontally off center from the detector as shown in Figure 3.19. In the first 120 planes, every fifth plane is fully covered with the scintillator whereas the intermediate four are partially covered, that is, only on the beam centered side of the detector. For the rest of the planes in the detector, again, every fifth plane is fully covered with scintillator, but the intermediate four have no scintillator coverage at all. The upstream part of the detector is used to measure the energy of

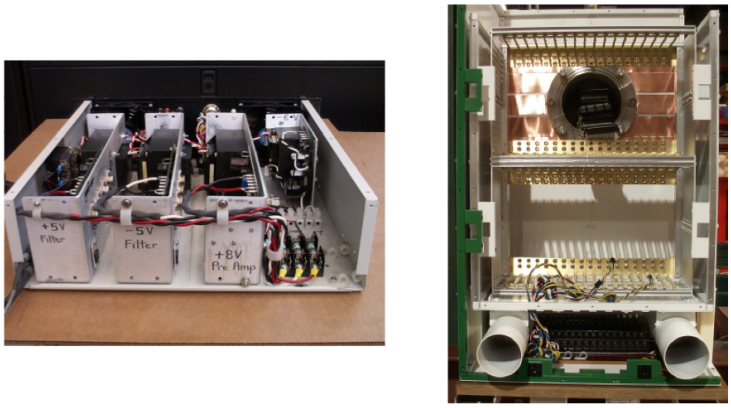

Figure 3.18: *(Left) The ArgoNeuT electronics custom power supply. (Right) The RF shielding cage used to minimize noise on the feedthrough and preamplifiers. Also shown is the preamplifier cooling mechanism (with remote ducts). Figure from Ref. [10].*

hadronic showers; hence, it is more finely instrumented and is called the 'calorimeter'. The downstream part of the detector serves as a muon tracker and is called the 'spectrometer'. The idea behind it is that a neutrino interaction in the calorimeter region produces a muon (in case of charged current muon neutrino interaction) that travels to the downstream end to the spectrometer and is fully reconstructed.

The detector sits in an average toroidal magnetic field of 1.3 T produced by a coil of current-carrying cables that pass through a hole along the length of the detector . The hole is 55.8 cm offset from the center of the planes and the detector is positioned in such a way that the beam is centered halfway between the left vertical edge of the detector and the hole, (see Figure 3.19). The magnetized detector allows to determine the charge and momentum of a particle by using the direction and amount of curvature of the particle traveling in the magnetic field.

MINOS ND employs scintillator strips that are made of polystyrene covered with reflective coating of polystyrene 85% and TiO_2 15% by weight. Wavelength shifting (WLS) fibers are grooved 2 mm deep in the middle of each scintillator strip. When a charged par-

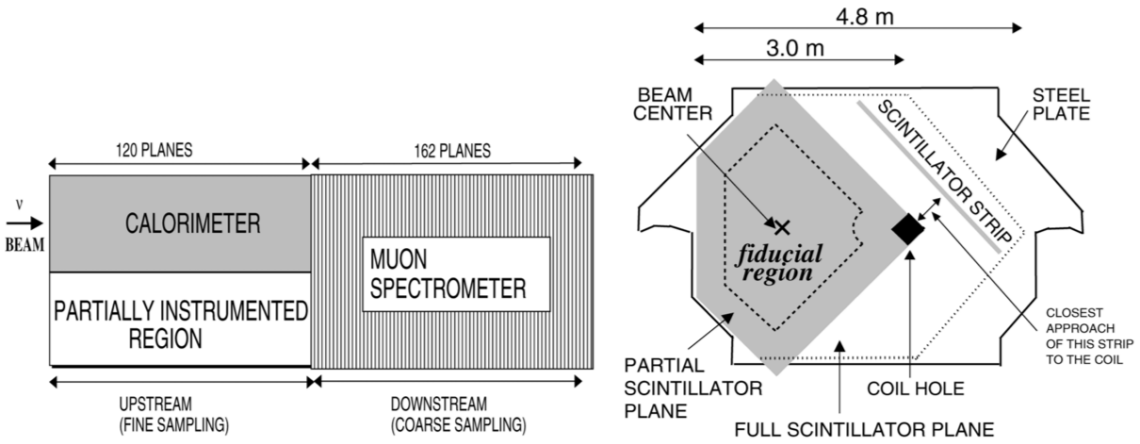

Figure 3.19: *(Left) The regions of the MINOS ND, as used by the MINOS experiment. (Right) The MINOS plane configurations. The beam and fiducial volume are centered around the middle of the partially instrumented planes, left of the coil [93].*

ticle travels through the scintillator strip, UV light peaked at 420 nm is produced which is absorbed by the WLS fibers. The WLS fibers re-emit the light at a wavelength of 470 nm and carry it to the end of the strip where it is carried to the photomultiplier tubes via clear fibers, (see Figure 3.20).

The MINOS detector plays a significant role in the full reconstruction of muons that exit the ArgoNeuT TPC and enter MINOS ND. The muon energy resolution $\Delta E_\mu/E_\mu$ varies smoothly from 6% to about 13% for the muons with energy higher than 1 GeV [94]. Most of the muons that are produced by the NuMI beam neutrino interactions range out in MINOS ND, so they are precisely reconstructed using the range in the detector. If a muon exits MINOS ND, it can be fully reconstructed measuring the amount of its curvature in the magnetic field.

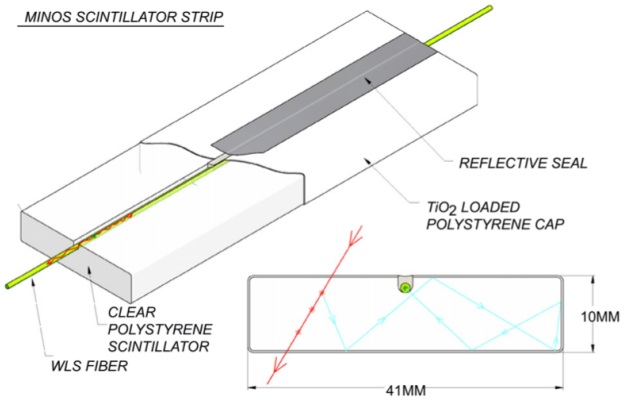

Figure 3.20: *MINOS scintillator strip concept [85].*

Chapter 4

Generation, Simulation and Reconstruction of Neutrino Events

The software used in ArgoNeuT for the neutrino event generation, simulation and reconstruction is called liquid argon software (LArSoft). It includes a neutrino event generator that provides simulated final state particles outside the nucleus that are then fed into the detector simulation, where they propagate through the detector medium producing simulated ionization electrons. The simulation also includes the drifting of the ionization electrons to the detector's wire planes along with the diffusion and the electronic response model of the planes. The particles that exit the ArgoNeuT TPC are simulated to propagate outside the TPC until they reach the front face of the MINOS near detector (if forward going). The trajectories of particles in ArgoNeuT and MINOS near detector are simulated and reconstructed like data. The simulation plays a vital role in improving the reconstruction algorithms, determining the reconstruction efficiency, the proper selection cuts for physics analyses. LArSoft also gives a number of modules to the user for reconstruction of neutrino events. In the following, the neutrino event generation, simulation and reconstruction as handled by LArSoft is described in detail. The neutrino event simulation and reconstruction sections generally follow the description given in Ref. [10].

4.1 Neutrino Event Generation

ArgoNeuT uses the NUANCE [44], GENIE [95] and NuWro [96] neutrino event generators in order to generate neutrino interactions with argon target. The work presented in this study corresponds to the neutrino interactions from the NUANCE neutrino event generator software which includes the charge current quasi-elastic neutral hyperon production as one of the interaction channel. NUANCE has been customized for ArgoNeuT detector and it gives the neutrino event rates, final state particles exiting the nucleus and their kinematics. The generator produces 99 neutrino/antineutrino interactions channels corresponding to different interaction types, ranging from 100 MeV to 10^3 GeV. All the 99 neutrino/antineutrino interaction channels are given in a table in Figure 4.1.

4.1.1 Quasi-Elastic Cross Section Model in NUANCE

NUANCE uses cross section models that are specific to the interaction types. Since the nucleons are in the bound state in a neutrino experiment, the Fermi gas model has been used (Fermi motion and Pauli blocking), where a uniform initial momentum density (up to a user-specified maximum value) and a negative binding energy is assigned to the bound nucleon. There is a threshold momentum for bound nucleon above which it can exit the nucleus and the reaction can occur. Therefore, in the absence of any final state interactions (in the nucleus), the minimum momentum carried by the nucleon exiting the nucleus must be equal to the threshold value. NUANCE accounts for the lepton masses for all interaction types [44].

NUANCE uses the relativistic Fermi gas model of Smith and Moniz [46] for the quasi-elastic interactions (charge and neutral current two-body interactions with nucleons). The model gives cross section for both free and bound state nucleons, using identical form factors for both cases. For free nucleon target the binding energy is set to zero along with its initial momentum distribution as a delta function at zero [44].

#	CC / NC	Reaction
Cabibbo–allowed quasi–elastic scattering from nucleons		
1	CC	$\nu_\mu n \to \mu^- p$ ($\overline{\nu}_\mu p \to \mu^+ n$)
(Quasi–)elastic scattering from nucleons		
2	NC	$\nu_\mu n \to \nu_\mu n$ ($\overline{\nu}_\mu n \to \overline{\nu}_\mu n$) $\nu_\mu p \to \nu_\mu p$ ($\overline{\nu}_\mu p \to \overline{\nu}_\mu p$)
Resonant single pion production		
3	CC	$\nu_\mu p \to \mu^- p \pi^+$
4	CC	$\nu_\mu n \to \mu^- p \pi^0$
5	CC	$\nu_\mu n \to \mu^- n \pi^+$
6	NC	$\nu_\mu p \to \nu_\mu p \pi^0$
7	NC	$\nu_\mu p \to \nu_\mu n \pi^+$
8	NC	$\nu_\mu n \to \nu_\mu n \pi^0$
9	NC	$\nu_\mu n \to \nu_\mu p \pi^-$
10–16		Corresponding $\overline{\nu}_\mu$ processes
Multi–pion resonant processes		
17	CC	$\nu_\mu p \to \mu^- \Delta^+ \pi^+$
18	CC	$\nu_\mu p \to \mu^- \Delta^{++} \pi^0$
19	CC	$\nu_\mu n \to \mu^- \Delta^+ \pi^0$
20	CC	$\nu_\mu n \to \mu^- \Delta^0 \pi^+$
21	CC	$\nu_\mu n \to \mu^- \Delta^{++} \pi^-$
22	NC	$\nu_\mu p \to \nu_\mu \Delta^+ \pi^0$
23	NC	$\nu_\mu p \to \nu_\mu \Delta^0 \pi^+$
24	NC	$\nu_\mu p \to \nu_\mu \Delta^{++} \pi^-$
25	NC	$\nu_\mu n \to \nu_\mu \Delta^+ \pi^-$
26	NC	$\nu_\mu n \to \nu_\mu \Delta^0 \pi^0$
27	NC	$\nu_\mu n \to \nu_\mu \Delta^- \pi^+$
28–38		Corresponding $\overline{\nu}_\mu$ processes
39	CC	$\nu_\mu p \to \mu^- p \rho^+(770)$
40	CC	$\nu_\mu n \to \mu^- p \rho^0(770)$
41	CC	$\nu_\mu n \to \mu^- n \rho^+(770)$
42	NC	$\nu_\mu p \to \nu_\mu p \rho^0(770)$
43	NC	$\nu_\mu p \to \nu_\mu n \rho^+(770)$
44	NC	$\nu_\mu n \to \nu_\mu n \rho^0(770)$
45	NC	$\nu_\mu n \to \nu_\mu p \rho^-(770)$
46–52		Corresponding $\overline{\nu}_\mu$ processes
53	CC	$\nu_\mu p \to \mu^- \Sigma^+ K^+$
54	CC	$\nu_\mu n \to \mu^- \Sigma^0 K^+$
55	CC	$\nu_\mu n \to \mu^- \Sigma^+ K^0$
56	NC	$\nu_\mu p \to \nu_\mu \Sigma^0 K^+$
57	NC	$\nu_\mu p \to \nu_\mu \Sigma^+ K^0$
58	NC	$\nu_\mu n \to \nu_\mu \Sigma^0 K^0$
59	NC	$\nu_\mu n \to \nu_\mu \Sigma^- K^+$
60–66		Corresponding $\overline{\nu}_\mu$ processes
67	CC	$\nu_\mu n \to \mu^- p \eta$
68	NC	$\nu_\mu p \to \nu_\mu p \eta$
69	NC	$\nu_\mu n \to \nu_\mu n \eta$
70–72		Corresponding $\overline{\nu}_\mu$ processes
73	CC	$\nu_\mu n \to \mu^- K^+ \Lambda$
74	NC	$\nu_\mu p \to \nu_\mu K^+ \Lambda$
75	NC	$\nu_\mu n \to \nu_\mu K^0 \Lambda$

#	CC / NC	Reaction
76–78		Corresponding $\overline{\nu}_\mu$ processes
79	CC	$\nu_\mu n \to \mu^- p \pi^+ \pi^-$
80	CC	$\nu_\mu n \to \mu^- p \pi^0 \pi^0$
81	NC	$\nu_\mu p \to \nu_\mu p \pi^+ \pi^-$
82	NC	$\nu_\mu p \to \nu_\mu p \pi^0 \pi^0$
83	NC	$\nu_\mu n \to \nu_\mu n \pi^+ \pi^-$
84	NC	$\nu_\mu n \to \nu_\mu n \pi^0 \pi^0$
85–90		Corresponding $\overline{\nu}_\mu$ processes
Deep Inelastic Scattering		
91	CC	$\nu_\mu N \to \mu X$
92	NC	$\nu_\mu N \to \nu_\mu X$
93–94		Unused
95	CC	Cabibbo–supp. QE hyperon production: $\overline{\nu}_\mu p \to \mu^+ \Lambda$ $\overline{\nu}_\mu n \to \mu^+ \Sigma^-$ $\overline{\nu}_\mu p \to \mu^+ \Sigma^0$

#	CC / NC	Reaction
Coherent / diffractive π production		
96	NC	$\nu_\mu A \to \nu_\mu A \pi^0$ $(\overline{\nu}_\mu A \to \overline{\nu}_\mu A \pi^0)$
97	CC	$\nu_\mu A \to \mu^- A \pi^+$ $(\overline{\nu}_\mu A \to \mu^+ A \pi^-)$
ν–e elastic scattering		
98	–	$\nu_\mu e \to \nu_\mu e$ $(\overline{\nu}_\mu e \to \overline{\nu}_\mu e)$
ν–e inverse μ decay		
99	CC	$\nu_\mu e \to \mu^- \nu_e$

Figure 4.1: *Channels in NUANCE Event Generator.*

In order to calculate the cross section for the charge current quasi-elastic hyperon production, the Smith and Moniz model has been extended by Pais [47] to account for the inelasticity of the interaction and the $|\Delta I| = 1/2$ rule. Relevant mathematical description about the cross section can be found in Sec. 1.5.

4.1.2 Setting up NUANCE for ArgoNeuT

NUANCE neutrino event generator software, which has been previously used for carbon and oxygen targets, is modified to be used for an argon target, and specifically for the ArgoNeuT detector. The changes made in the original source are setting a target with A = 40 for argon, with 18 protons and 22 neutrons, a nucleon binding energy = 29.5 MeV, Fermi momentum of proton = 242 MeV, and Fermi momentum of neutron = 250 MeV. The density of argon is set to 1.396 g/cm^3. The detector shape is also set to a cube of size 47.5 cm $\times$ 40 cm $\times$ 90 cm, which are the x, y and z dimensions of the ArgoNeuT detector, respectively. It is also important to mention that based on very high resolution of LArTPC detectors, automatic decay of particles inside the nucleus is stopped. A LArTPC can resolve a secondary detached (decay) vertex, whereas other experiments using NUANCE, such as MiniBooNE, do not have this sensitivity.

4.1.3 Quasi-Elastic Cross Sections Parameters in NUANCE

NUANCE uses the Smith and Moniz model for the generation of quasi-elastic interactions. The axial and the vector form factors are set to $M_A = 0.990$ GeV and $M_V = 0.840$ GeV in the software, which match with those in the widely used GENIE neutrino event generator. A description of cross section parameters for all the interactions in NUANCE can be found in [10].

4.1.4 Event Kinematics from NUANCE

The output from NUANCE includes a list of particles along with their particle codes (according to Particle Data Group convention), tagged as either -1 (initial state particle), -2 (final state particle before interactions) or 0 (the final state particle after interactions). Detector simulation uses only the particles with the status code of 0. Event kinematics such as the position of the neutrino interaction (primary vertex), total energy and direction cosines of the particles are also given. The output also includes a NUANCE channel number for each event.

4.2 Neutrino Event Simulation

4.2.1 Particles Propagation in Detector Medium with Geant4

Using the Geant4 software package, the 'final state particles after interaction' from NUANCE are simulated in the detector and are propagated through the detector medium, including the TPC, inner and outer cryostat, chimney, containment vessel and the first plane of the MINOS near detector. Figure 4.2 shows the geometry of ArgoNeuT simulated in Geant4. Particles undergo the relevant physical processes as they travel through the detector until they reach the kinetic energy of 100 keV. Three dimensional voxels (pixels in 3D of volume $0.03 \times 0.03 \times 0.03$ cm^3 each) record the ionization electron cloud.

4.2.2 Electron Drift and Signal Simulation at the Wire Planes

After the voxels record the ionization, the next step is to drift the ionization to the wire planes and the simulation of the signals. Longitudinal and transverse diffusion constants are used to account for the diffusion while the ionization is drifted towards the wire planes. The amount of diffusion depends on the time it takes the ionization to reach the wire planes (which depends on the drift distance and the electric field). Effects of recombination are also

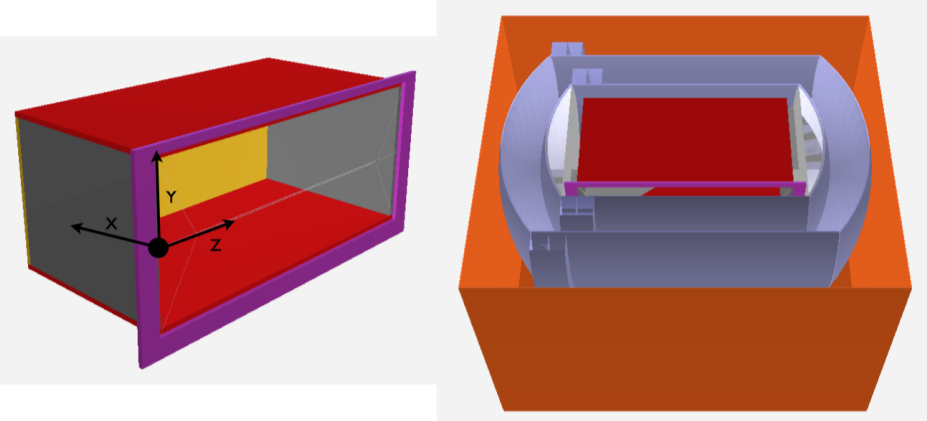

Figure 4.2: *(Left) The ArgoNeuT TPC simulated in Geant4, cathode shown in yellow color and the wire planes are in purple. The origin of the ArgoNeuT TPC is also shown. (Right) The ArgoNeuT TPC along with inner and outer cryostat as simulated in Geant4. Neutrino beam enters from the left side. MINOS first plane (not shown) is also simulated in Geant4. Figure from Ref. [10].*

simulated (See Equation 2.3) [72, 73]. Finally the total number of electrons (after diffusion and recombination) reaching a wire is calculated at the position of the wire plane(s) and then registered to the respective wire. The electron cloud now has a wire number and the range of the time ticks associated to it along with the number of electrons (charge). The response shapes of induction and collection planes are then convolved with the charge in order to obtain raw digit ADC counts. Simulated electronic noise is added to the wires as a final step of simulating electron drift and signal response of wire planes. Noisy or dead wires in the actual detector are given zero ADC counts for all the time samples in both data and simulation.

4.2.3 Through Going Muon Simulation

Muons that enter the ArgoNeuT detector from upstream can contaminate a signal sample if the vertex is reconstructed inside the ArgoNeuT TPC. The MINOS near detector keeps track of muons entering the detector with each NUMI trigger. A properly normalized set

of these data muons is taken and, using the reconstructed kinematics of these muons from MINOS near detector, through going muons are simulated in the ArgoNeuT detector. For the simulation, these muons are placed just upstream of the front face of ArgoNeuT detector, with their kinematics from MINOS near detector and are propagated through the medium using the Geant4 software package.

4.3 Neutrino Event Reconstruction

The amount of data available for each event in a LArTPC detector is enormous. The detector offers excellent spatial resolution along with precise calorimetric information. As mentioned before, LArSoft is used to simulate and reconstruct events in LArTPC detectors. The software, developed from scratch, is kept detector 'agnostic' and is being constantly developed. In the software, the reconstructed quantities are referred to as objects, and generally a user has more than one algorithm to choose from in order to reconstruct an object. In the following, only the objects reconstructed (and the algorithms used to do that) in this analysis are discussed.

4.3.1 Raw Data Deconvolution - Data Calibration

Digitally recorded data from DAQ electronics has the information of charge deposition on wires as a function of time. These raw waveforms are subjected to deconvolution and noise filtering.

Induction plane signals are bipolar in a LArTPC, and two separate charge depositions on a wire close in time can appear as a single charge deposition. In collection plane, the signal is unipolar, but it is followed by a negative overshoot and exponential return to the baseline, which can effect the height of a nearby signal on the same wire. A fast Fourier transform (FFT) [97] is used for the raw data deconvolution, which outputs unipolar induction plane signals, corrected baseline in collection plane, and the identification of overlapping (in time)

charge depositions in both planes.

An empirically produced basic signal shape is employed for each wire in ArgoNeuT. For this purpose, thousands of long muon tracks that are almost parallel to the wire planes are used. In the process, the delta rays were neglected so as not to shift the basic pulse to a wider shape. This method accounts for effects of electron drift as well as electronic noise. A FFT with the narrowest signal considered as a delta function input to it, gives a good first order approximation for both planes. Base signal shapes can be better determined in future using the information about track angle with respect to the wire planes. Figure 4.3 shows the base signal shapes for induction and collection planes.

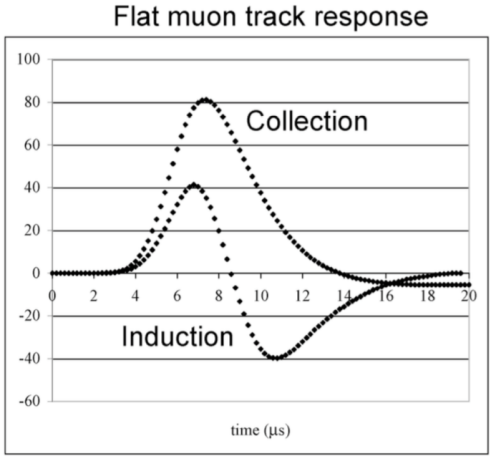

Figure 4.3: *The base signal shapes for Induction and Collection planes of ArgoNeuT detector as determined by an analysis of a large sample of muons parallel to the wire planes. Figure from Ref. [10].*

The results of raw data calibration can be seen in Figure 4.4, where three consecutive wire's signals are shown before and after calibration. One can see that after calibration, the induction signal has a unipolar shape, separate charge depositions close in time (on a wire) are identified, and baseline shift due to the negative portion of induction signal for the adjacent charge deposition is corrected.

The deconvolution process also includes a frequency filter. High frequency noise com-

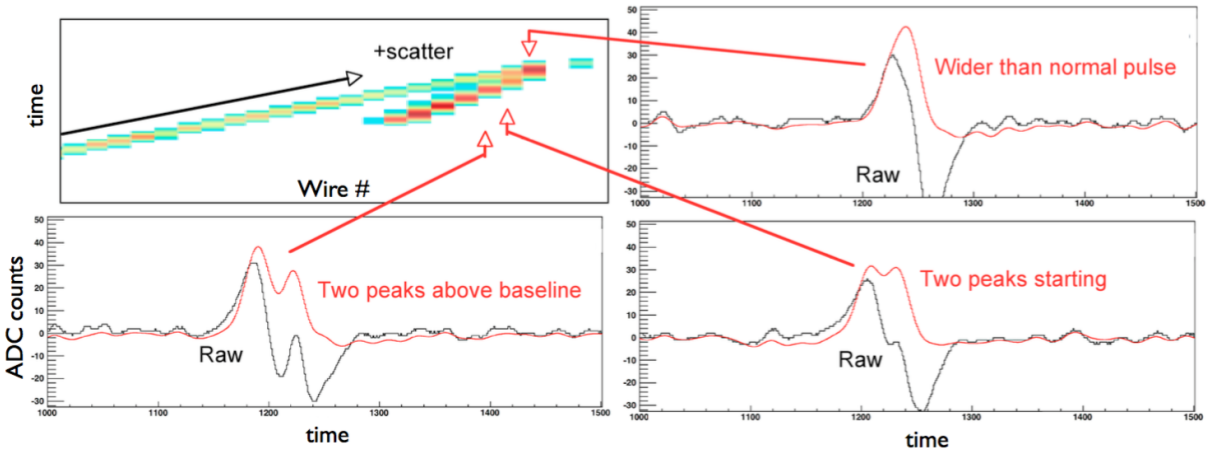

Figure 4.4: *(Upper left) Induction plane of ArgoNeuT with two deconvoluted tracks. (Upper right, lower right, lower left) The raw (black) and deconvoluted (red) wire signals in time from the three consecutive wires with overlapping hits. Figure from Ref. [75].*

ponent that has been amplified by the FFT is filtered using a high frequency filter. The induction plane filter uses an analytic function that keeps the low frequencies (signal) and removes the high frequency (noise), whereas, for the collection plane, a Weiner filter [98] is used, which assumes known signal and noise spectra and thus deals with the low frequency baseline shift. The resulting waveforms are smooth and unipolar.

4.3.2 Hit Finding

The deconvoluted waveform is the input to the hit finding. One needs to know the interesting regions in the waveform that can be characterized as hits (ADC, time) on a wire. Using a Gaussian-shape approximation, the hit finding algorithm finds hits on individual wires. The process begins with finding a local minimum in the (time, ADC) space of the wire. Once the local minimum is found, the algorithm looks for local maximum in the increasing time. If the local maximum is above a certain threshold, the area is identified as a hit. The algorithm then scans the space towards the higher time to find the local minimum. The time distance between the two local minima is considered as the time width of the hit. The

algorithm repeats this whole process until the full time window for an event is scanned.

After the time widths of the hit are known, the algorithm uses Gaussian fits to determine the characteristics of a hit. The fit needs seed parameters that need to be carefully selected for the fit to converge. The seed value of time width of the hit or hit width parameter comes from the typical hit widths in the data, which is different for induction and collection plane. The seed for the time position of the hit is the time of local maximum. For single hits, the hit amplitude is set to the local maximum. In case of n multiple hits (overlapping hits), n Gaussians are fit to the n consecutive hits in the waveform, and the amplitude is set to the signal height plus any contribution from the neighboring hits via linear approximation. The measured height of a hit can written be as

$$O_i = A_j f(t_j - t_i; w). \tag{4.1}$$

Here, O_i is the observed height of the hit in consideration and A_j is the actual or true height of the adjacent hits. The function $f(t_j\text{-}t_i;w)$ is the normalized model signal with width w. The function f evaluates the model pulse at the peak time of adjacent hits and determines the effect of nearby hits on the amplitude of the hit under consideration. The above equation can be considered as $\vec{O} = M\vec{A}$, where M is a matrix that carries values of f evaluated at each point. Each hit has a unique value of its central time, start time, end time, width, signal amplitude among other measurements.

4.3.3 Density-Based Cluster Finding

Next step after reconstruction of hits is to group them together based on their position and density to make a new object, a *cluster*. The clustering of hits is done following the procedure of 'density-based spatial clustering of applications with noise' (DBSCAN) [99]. The hits are clustered in each wire plane separately. A hit q is 'directly density-reachable' from another hit p if it is with in a given neighborhood ϵ and if p has a sufficiently higher

density of hits around it. ϵ is modified to incorporate slight difference in the resolution in wire and time directions. Another case is, a hit q is 'density-reachable' from hit p if there is a series of consecutive hits p_i (p_1,....p_n), such that $p_1 = p$ and $p_n = q$, and each $p_i + 1$ is directly density-reachable from p_i. It can be noted that one hit can be directly density-reachable from the other hit but not vice versa. This can happen if one hit is surrounded by sufficient number of hits but the other is not. Based on this possible asymmetry, a new definition is required; two hits p and q are density-connected if there is another hit k such that both hits p and q are density-reachable from k. The algorithm takes an arbitrary hit p and finds all the hits that are density-reachable from hit p. The hit inside a cluster are called core hits, whereas, the ones at the border of the cluster are called border hits. Once the algorithms finds a complete cluster, it moves on to the hits that are yet not associated with any cluster, until all the hits are considered. Figure 4.5 gives examples for the definitions of direct density-reachable, density-reachable and density-connected. Figure 4.6 gives an example of the cluster reconstruction via DBSCAN in ArgoNeuT's collection plane.

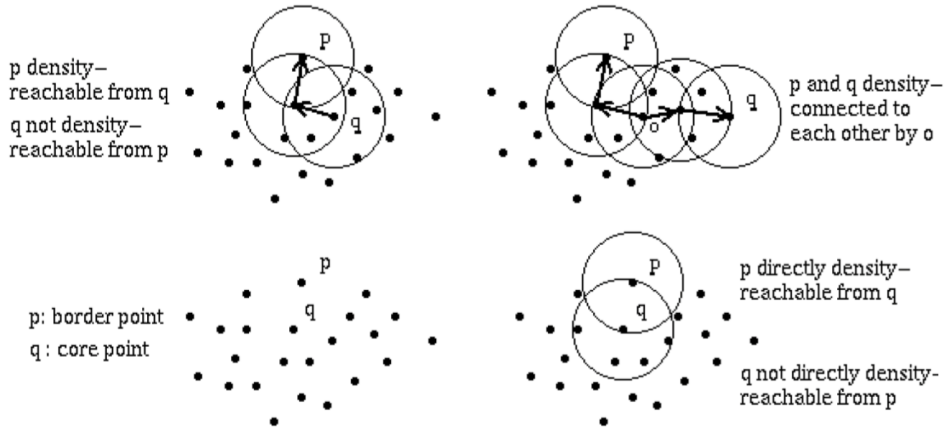

Figure 4.5: *DBSCAN definitions. Figure adapted from Ref. [99].*

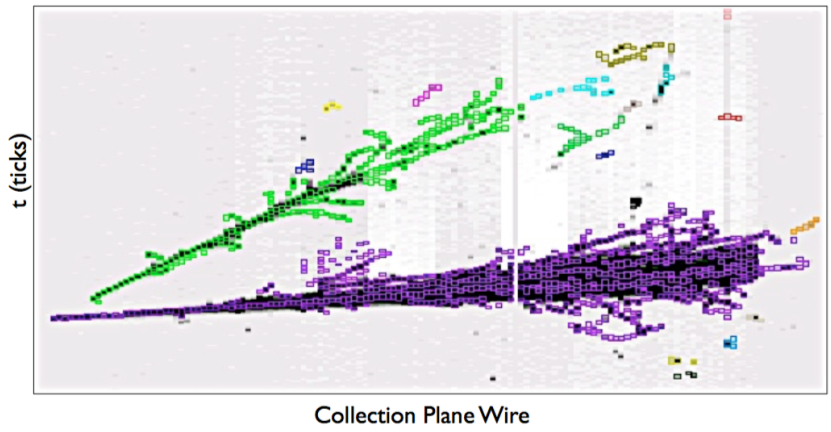

Figure 4.6: *DBSCAN algorithm at work on a neutrino event. Raw data shown in grey, distinct colors correspond to distinct clusters. Figure from Ref. [75].*

4.3.4 Line-Like Cluster Finding

Since ArgoNeuT is not a magnetized detector, particle trajectories are expected to be line-like. A simple linear regression to find the line-like clusters from density-based clusters would be too simplistic for the events with more than one track and or noisy clusters. The density-based clusters of even a straight track can be tricky because of multiple factors, such as, multiple Coulomb scattering, delta ray production, dead or noisy wires, non-uniformities in the electric field in the TPC, and others. The Hough transform [100] is used to find the line-like clusters in the ArgoNeuT.

A Hough transform creates a parameter space that is filled based on the locations and weights of points in an image. This parameter space is called a 'Hough accumulator', composed of cells of finite dimension. The algorithm defines a line $r = x\cos\theta + y\sin\theta$ for each (x, y) in an image. The line defines a unique sinusoidal wave for each (x, y) in the (r, θ) plane. If the curves for two (x, y) points are overlaid together, the intersection point in the (r, θ) plane defines a line that passes through both the points in (x, y) (See Figure 4.7). Each (x, y) point is added to the accumulator (r, θ) space and the cells with weight above certain threshold serve as the line candidates. A cell with the highest weight (highest number of

curve crossings) is found and a candidate line is formed by using the center-of-mass of the 3×3 cell window with the cell having highest weight at the center. This process is repeated, each time considering hits that are not associated to a line yet, until a threshold is reached or the maximum number of lines to be reconstructed is reached. It is important to note that a Hough transform can break a single line-like cluster to more than one. This is because the segments have slightly different slopes and intercepts, or in other words, there are more cells to choose from the Hough accumulator.

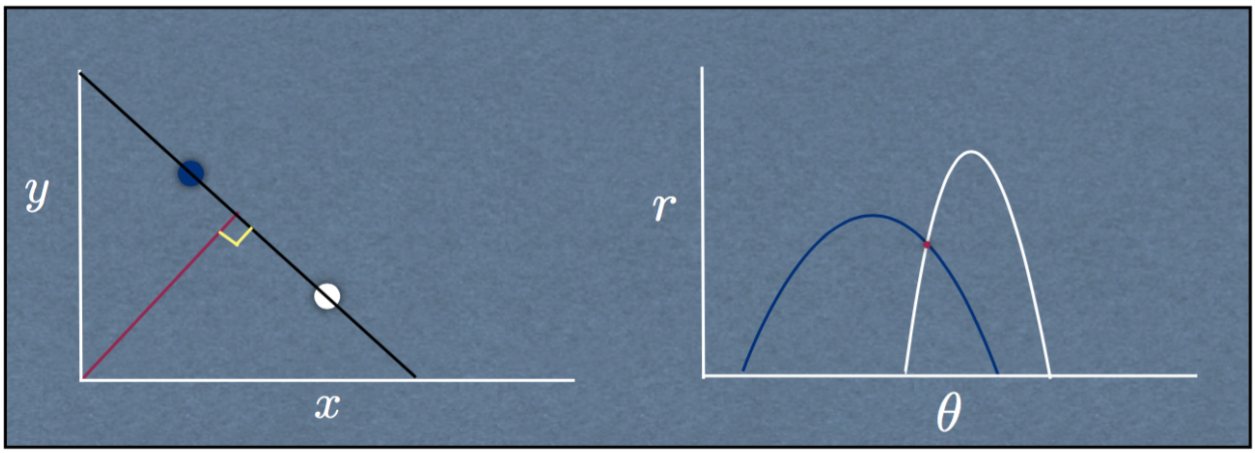

Figure 4.7: *(Left) Two point in (x, y) plane. (Right) The points parametrized in (r,θ) plane. The intersection point of the curves correspond to a line that passes through both points in (x, y). Figure from Ref. [10].*

4.3.5 Two Dimensional Line Merging

As mentioned in the previous section, the Hough transform, with its high resolution in r and θ can split a single line-like track to more than one cluster. Since, these two dimensional line-like clusters are used to reconstruct three dimensional tracks, it is vital to merge the clusters together based on their similar slopes and proximal endpoints. A simple algorithm is employed in LArSoft to merge the broken clusters together and make 'merged-lines' if they have similar slopes and their end points are in proximity. Figure 4.8 shows an example

of line merging in LArSoft.

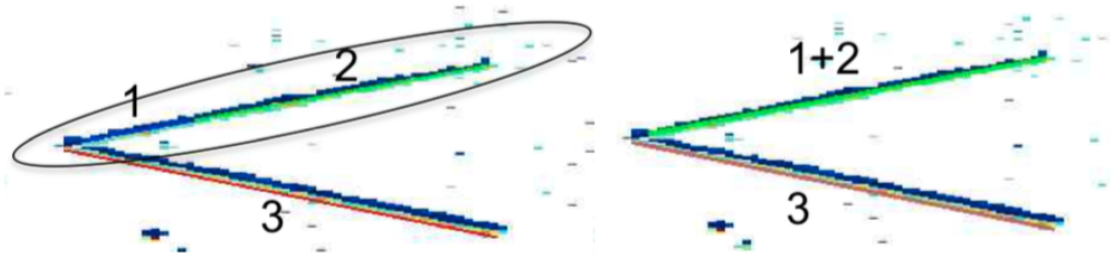

Figure 4.8: *(Left) Three hough line clusters; #1 in blue, #2 in green and #3 in red. (Right) Two merged-lines after merging hough line clusters. Figure from Ref. [10].*

4.3.6 3D Tracking

The (two dimensional) clusters can be matched between two wire planes in order to reconstruct 3D tracks. At the end of this step of reconstruction, one has a three dimensional image of an event. After accounting for the pre-samplings and the drift distance between two planes, the clusters are matched based on their start and end point time coordinates in each plane. After the two clusters are matched between the planes, a 3D track with its direction cosines is reconstructed. After reconstruction of a 3D track direction, hit-by-hit matching (similar to clusters end point matching) is done to produce 3D space points (x, y, z) which give a high resolution 3D image of an event. The coordinates of a space point are calculated as follows;

$$\begin{aligned} x &= tv_d, \\ y &= \frac{v-u}{2\cos\alpha}, \\ z &= \frac{v+u}{2\sin\alpha} - \frac{Y}{2\tan(\alpha).} \end{aligned} \tag{4.2}$$

Here, u and v are the wire coordinates (in cm) for induction and collection planes, respectively. v_d is the drift velocity of the ionization charge in the TPC, Y is the height of the TPC and α is the absolute value of the angle of the wires with respect to the vertical.

4.3.7 Matching ArgoNeuT Tracks with MINOS Tracks

Due to the small size of the ArgoNeuT detector, most of the muons produced in the TPC exit the detector and enter the MINOS near detector. In order to get the information about the muons produced in the TPC, the tracks reconstructed by MINOS offline analysis code [101] have been used. For a stopping track, the momentum is reconstructed by measuring its total deposited energy in the detector; whereas, for a non-stopping track, the momentum is determined by its curvature in the magnetized MINOS near detector. MINOS's magnetic detector also allows to determine the charge of the track. A track is matchable if the Z vertex of a track is within 20 cm of the center of first MINOS plane. ArgoNeuT and MINOS tracks are selected on a spill-by-spill basis using the common time stamp from the accelerator division. After this broad selection of matchable tracks from ArgoNeuT and MINOS near detector, a set of criteria based on the tracks' direction and their relative position is applied. According to ArgoNeuT's definition, a track stops in MINOS if it stops in the instrumented region of MINOS. ArgoNeuT's interpretation of reconstructed variables from MINOS differs slightly from the interpretation used by MINOS experiment. Figure 4.9 and Figure 4.10 show the schematic diagrams of ArgoNeuT simulation and reconstruction, in addition to MINOS reconstruction.

4.3.8 Vertex Finding

Merged-lines (called 'line merger clusters' or 'clusters' from now on) are used to reconstruct two-dimensional vertices in each wire plane. The vertex finding algorithm finds multiple vertices per wire plane and then matches them in two wire planes to find three-dimensional vertices.

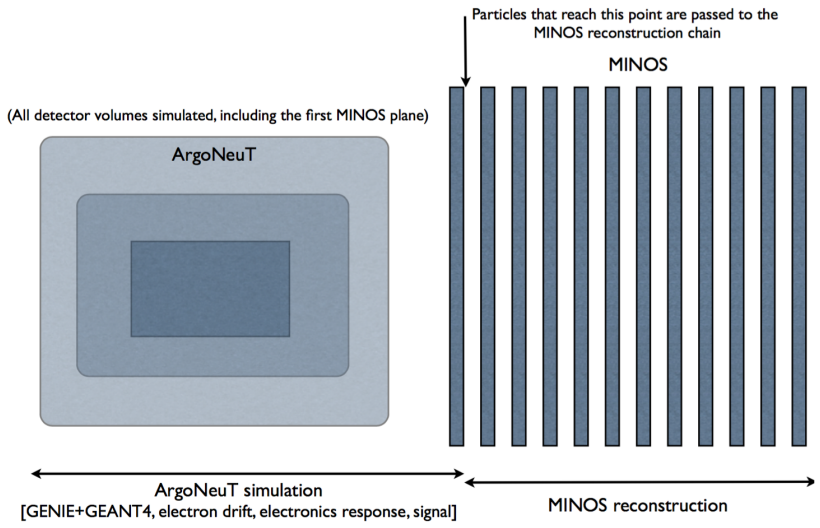

Figure 4.9: *The ArgoNeuT simulation corresponding to TPC, inner and outer cryostat. The figure is not to scale. Figure from Ref. [10].*

The algorithm, as a first step, sorts the clusters in each view in descending length. Then it starts with picking the MINOS matched track (and the two-dimensional clusters it is associated with), or otherwise the longest cluster in a wire plane with its start point as a candidate for vertex. Vertex fitting is done in each plane separately. A straight line fit is performed on the beginning part of all the clusters since most of the tracks in ArgoNeuT are straight (at least in the beginning); however, line fitting is iterated three times, each time throwing away the hits that have high incremental χ^2 values with respect to the straight line fit. This is to reject the delta ray hits and other noise hits. Wire number coordinate of a hit is converted to time ticks. Errors in hit times are incorporated for each plane; whereas, error in wire number is considered to be zero. After filtering the hits in a cluster, it is 'accepted' for vertexing if it has more hits than a minimum threshold number.

The two-dimensional start point of the first accepted cluster in a plane is interpreted as a 'guessed vertex' and distance of closest approach between a cluster and guessed vertex is calculated for each cluster. Clusters with distance of closest approach greater than a

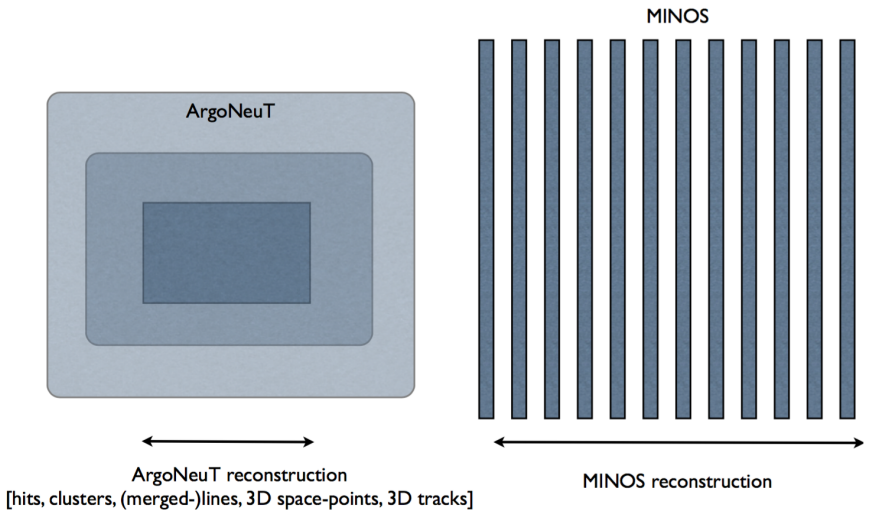

Figure 4.10: *The ArgoNeuT reconstruction applied to both simulation and data. The figure is not to scale. Figure from Ref. [10].*

threshold are not considered for the vertex finding. A vertex χ^2 is defined as a squared sum of distance of closest approach of clusters weighted by their error. Minimizing the χ^2 gives the best fit coordinates of a vertex in two dimensions. The vertex is re-fitted two more times, each time using the best fit coordinates of a vertex from previous fit as a guessed vertex. Figure 4.11 shows vertex finding algorithm at work for an ArgoNeuT simulated event.

For technical description of vertex finding, let us assume a straight line cluster (blue line in Figure 4.12) in one of the wire plane whose x-axis is the wire numbers in ticks and y-axis is the time tick. The cluster makes an angle θ with the horizontal and has an intercept 'c'. Say we have a guessed vertex at point 'C' with coordinates (v_x, v_y). The distance of closest approach; μ from the guessed vertex to the straight line cluster is given by,

$$\mu = c\cos\theta - v_y\cos\theta - v_x\sin\theta. \tag{4.3}$$

One can write $\theta = \tan^{-1} m$, where m is the slope of the straight line cluster. Therefore, Equation 4.3 can be written as

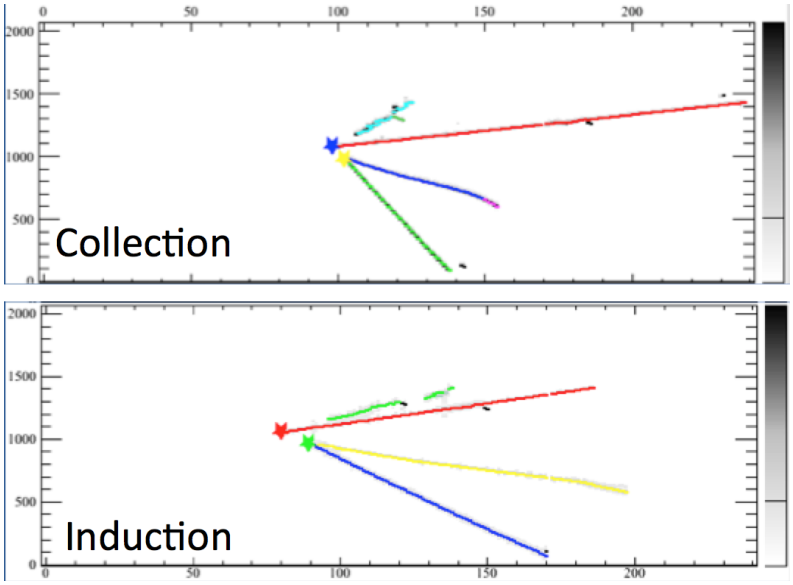

Figure 4.11: *An example simulated event showing reconstructed vertices in an event. Distinct colored lines and stars show distinct clusters and vertices, respectively. Two vertices are reconstructed in each view.*

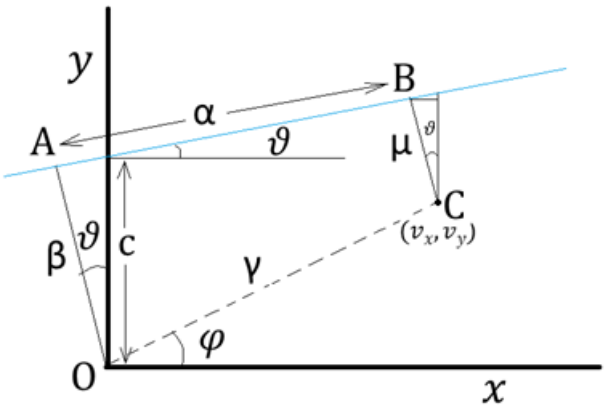

Figure 4.12: *Straight line cluster (in blue) in a wire plane. x-axis is wire numbers converted to ticks and y-axis is time ticks. Point C represents a guessed vertex. μ is the distance of closest approach from guessed vertex to the straight line cluster.*

$$\mu = c\cos(\tan^{-1} m) - v_y \cos(\tan^{-1} m) - v_x \sin(\tan^{-1} m). \tag{4.4}$$

And the uncertainty in the distance of closest approach σ_μ can be written as

$$\sigma_\mu = \sqrt{(\cos\theta)^2\sigma_c^2 + (\frac{1}{1+m^2}[-c\sin\theta + v_y\sin\theta + v_x\cos\theta])^2\sigma_m^2}, \tag{4.5}$$

where σ_c and σ_m are the errors on the intercept c and slope m respectively of the straight line fit of a cluster and are calculated while line fitting.

Using the above expressions, one can write the vertex χ^2 of a cluster i as follows

$$\chi_i^2 = \frac{\mu_i^2}{\sigma_{\mu_i}^2} = \frac{(c_i\cos\theta_i - v_y\cos\theta_i - v_x\sin\theta_i)^2}{(\cos\theta_i)^2\sigma_{c_i}^2 + (\frac{1}{1+m_i^2}[-c\sin\theta_i + v_y\sin\theta_i + v_x\cos\theta_i])^2\sigma_{m_i}^2}. \tag{4.6}$$

Total vertex χ^2 if n clusters are added to the vertex is

$$\chi^2 = \sum_{i=1}^{n}(\frac{(c_i\cos\theta_i - v_y\cos\theta_i - v_x\sin\theta_i)^2}{(\cos\theta_i)^2\sigma_{c_i}^2 + (\frac{1}{1+m_i^2}[-c\sin\theta_i + v_y\sin\theta_i + v_x\cos\theta_i])^2\sigma_{m_i}^2}). \tag{4.7}$$

Minimizing the above equation gives best fit values (v_x, v_y) for the vertex. The algorithm iterates the whole process for the clusters that are not yet associated with a vertex, until a maximum number of clusters in a wire plane is reached. Vertices are then matched between two planes to reconstruct three-dimensional vertices.

4.3.9 Calorimetric Reconstruction

Once a three-dimensional track is reconstructed, calorimetric reconstruction can be done in order to identify the corresponding particle. This has been discussed in Section. 2.2. Calorimetry uses electronic readout from the collection plane for the measurements as it gives the higher gain.

The calorimetry algorithm uses three-dimensional tracks to determine the track pitch, which is the effective length of the track as seen by a single wire. The corresponding hits of a track are used to determine the amount of charge deposited per unit track pitch. The amount of charge received by the wires is reduced due to the two effects: absorption, which is charge loss due to electronegative impurities in the detector, and recombination, which

is the recombination of ionization electrons with argon ions before they are separated by the applied electric field. The recombination effect is often called charge quenching. The correction for both of these effects is applied to calculate the actual total charge deposited by a track per unit track pitch. Birk's Law [72, 73] is used to calculate the amount of energy deposited by a track per unit length (dE/dx), which is summed over a track to get the total amount of energy deposited by a track. Once charge deposition/loss per unit track length and total energy deposited by a track is known, one can do the particle identification. If a track stops in the detector, looking at the total energy deposited by the track versus its range can give a significant information about the particle that corresponds to the track. Also, the energy loss profile, dE/dx, as a function of residual range of a track also gives valuable information about the particle identification. The Figure 4.13 shows the curves for different particles using Geant4 simulation, overlaid by points for a track reconstructed by calorimetry module.

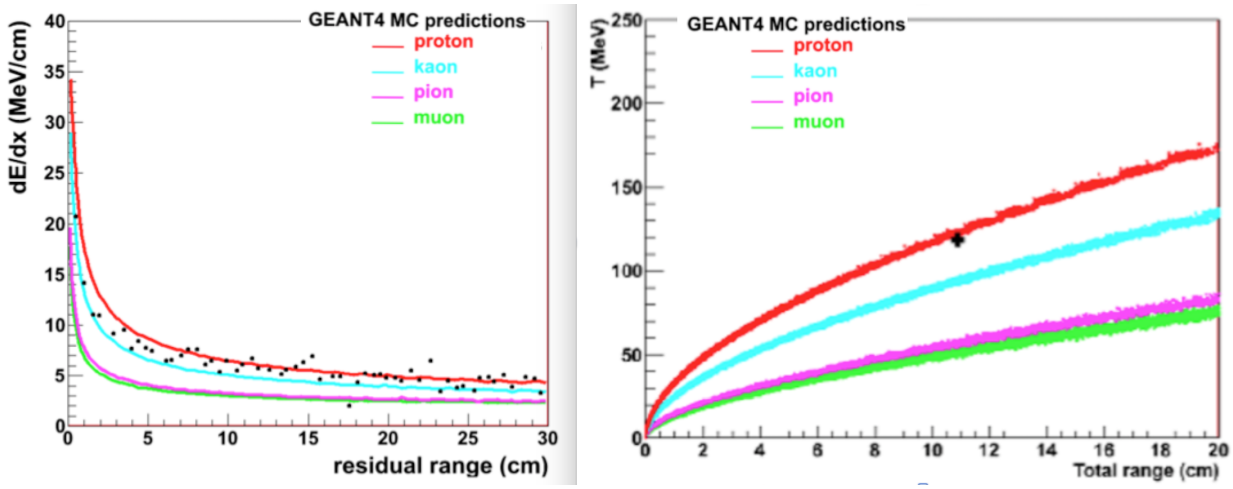

Figure 4.13: *(Left) Simulated energy loss per unit track length as a function of residual range (distance from the stopping point) for different stopping particles. The plot is overlaid by the point of a track reconstructed by the calorimetry module. (Right) Simulated kinetic energy as a function of range (distance traveled before particle stops) of different particles. Figure from Ref. [75].*

Chapter 5

Analysis

5.1 Introduction

This study is the first measurement of charge current quasi-elastic (CCQE) neutral hyperon production cross section in a LArTPC detector. In this interaction, a proton is converted to a hyperon. The interaction can be expressed as follows;

$$\begin{aligned} \bar{\nu_\mu} + p &\rightarrow \mu^+ + \Lambda^0, \\ \bar{\nu_\mu} + p &\rightarrow \mu^+ + \Sigma^0. \end{aligned} \tag{5.1}$$

This process is a Cabibbo-supressed process and has been studied sparsely. The interaction has been studied in past in 1970s with bubble chamber experiments. The Λ^0, being a weakly decaying strange particle with a relatively long decay time, decays to two charge particles $p\pi^-$, or two neutral particles $n\pi^0$. The Σ^0 electromagnetically decays to a photon and Λ^0 which eventually decays as mentioned above. This analysis is based on the topological properties of the Λ^0 decay – a detached secondary vertex with two tracks originating from it, in addition to a primary vertex with one or two tracks – and makes full use of the high quality images of neutrino interactions in a LArTPC. The events in which a CCQE neutral hyperon finally decays to the charge particles is the 'signal' for this analysis. Other neutrino

experiments, such as MiniBooNE, which is a Cherenkov light detector is not sensitive to the event topology of this type of interaction.

The NUANCE neutrino event generator has been modified for the argon target and ArgoNeuT detector and is interfaced with the LArTPCs' software; LArSoft. This allows for full detector simulation and the matching of ArgoNeuT's exiting muons to MINOS ND. This chapter describes the procedure followed in the analysis and the results. The cross section measurement for the processes shown in Equation 5.1 can be written as;

$$\sigma(_{CCQE_{\Lambda^0+\Sigma^0}}) = \frac{f \times (N_{data} - N_{bkg})}{\phi \times N_{targ} \times \epsilon}. \tag{5.2}$$

Here, N_{data} is the number of data events that pass all analysis cuts, N_{bkg} is the predicted number of background events, ϕ is the total antineutrino flux. N_{targ} is the number of targets in fiducial volume of the detector, ϵ is the efficiency of all analysis cuts. f is the correction for the branching fraction of hyperon decay to the neutral particles.

5.2 Analysis Steps

The analysis is conducted in two steps. The first step is automatic neutrino events reconstruction by the LArSoft modules, whereas the second step involves visual scanning. The analysis uses about five months of data from ArgoNeuT when the NUMI beam was in antineutrino-mode. Figure 5.1 shows the energy spectrum of the MC neutrino and antineutrino events in the antineutrino-mode run. One can see that the antineutrinos in the antineutrino beam are lower in energy as compared to the neutrinos. Figure 5.2 shows the energy spectrum of a sample of MC 'signal' events.

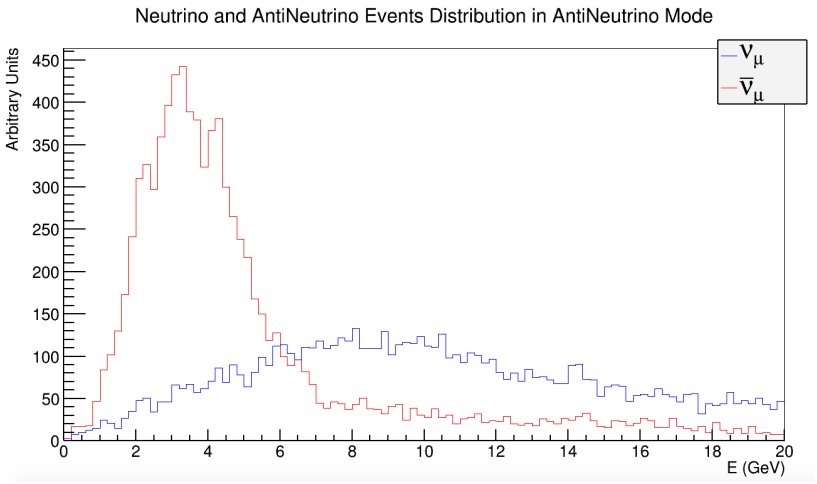

Figure 5.1: *An MC sample showing energy spectrum of neutrino and antineutrino events in the antineutrino-mode run of ArgoNeuT.*

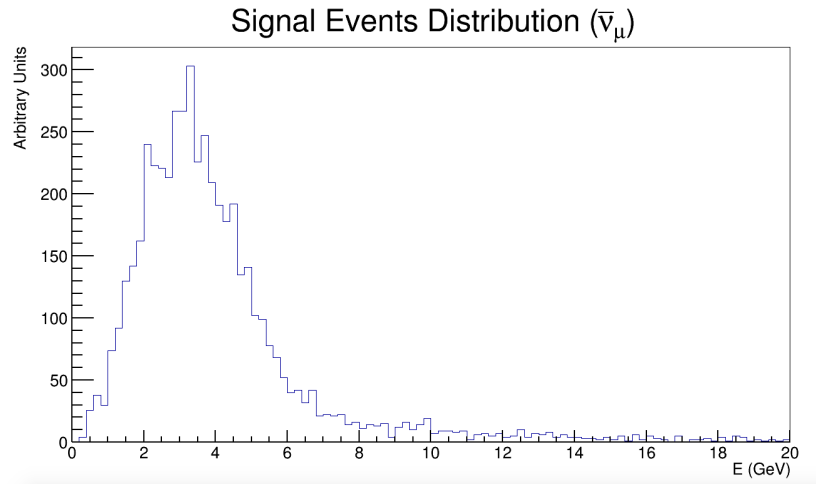

Figure 5.2: *An MC sample showing energy spectrum of signal events in the antineutrino-mode run of ArgoNeuT.*

5.2.1 Automatic Reconstruction

The first part of the analysis is based on automatic reconstruction and filtering of events based on automatic reconstruction cuts. The events generated by the NUANCE event generator are simulated in the detector and are passed through the full reconstruction chain

of ArgoNeuT. The muon track is matched with the MINOS near detector (MND) which gives its momentum and charge sign. The automatic cuts are aimed to keep as much of the signal events as possible and reject most of the background events. This is a difficult task for a weak signal like that expected for Λ^0. The reconstruction cuts require that the

1. The primary vertex is reconstructed inside the fiducial volume of TPC, defined as [3 $<$ x $<$ 44, -16 $<$ y $<$ 16, 6 $<$ z $<$ 86], with all dimensions in cm.

2. More than 1 Linemerger clusters are reconstructed in each wire view.

3. Track matching with MND (with +ve charge and non-zero momentum reconstructed by MND) ($\bar{\nu}_\mu$ events).

4. The MND matched track starts inside the fiducial volume of TPC.

Requiring more than one Linemerger cluster in each view rejects $\bar{\nu}_\mu$ CCQE events (which often have a single μ^+ and no other charged tracks). Requiring MND matching with positive charge rejects neutral current (NC) and ν_μ interactions. Fiducial volume cuts are selected in order to reject events that are near the edges of the TPC, where the electric field is non-uniform or those which have a through-going muon(s) that are not created by a neutrino interaction inside the TPC. Figure 5.3 shows the difference between the true and the reconstructed X, Y and Z vertex for all the MC events that pass automatic cuts. Gaussian fits are applied to the plots in order to understand the vertex resolution. The tails in Y and Z correspond to mis-reconstructed space points generated while matching hits between two planes. The shift in the X is due to the start time of an event in the MC, which is anywhere between 10 μs of NUMI beam window. Z coordinate of the reconstructed vertex is shifted towards the higher value, which is a result of vertexing that prefers MINOS matched track start point as its guessed vertex. Note that the vertex resolution for all three coordinates is at the sub-cm level.

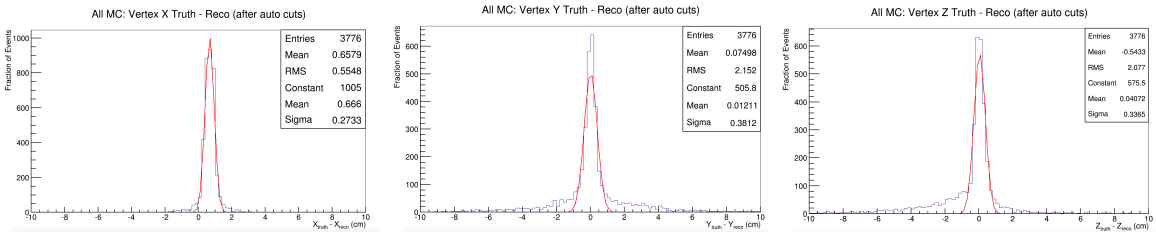

Figure 5.3: *Difference between the true and reconstructed X (left), Y (center) and Z (right) vertex of all events that pass automatic cuts.*

The X vs Z vertex distribution (top view of the detector) and X vs Y vertex distribution (downstream face view of the detector) of all the data passing automatic cuts are shown in Figure 5.4 and Figure 5.5, respectively. The X, Y and Z vertex distributions of the data and MC passing all automatic cuts are shown in Figure 5.6, Figure 5.7 and Figure 5.8. The fiducial volume cut of 6 cm (upstream) in the Z direction helps reject the through-going muons; however, one can see that they are not fully removed from data (see Figure 5.8). Through-going muons are not simulated in MC and are removed from the data later via visual scanning. More data is shifted towards higher X values, this is also because of through-going muons that are parallel to the cathode where electric field non-uniformities tend to break the track into more than one and a vertex is reconstructed.

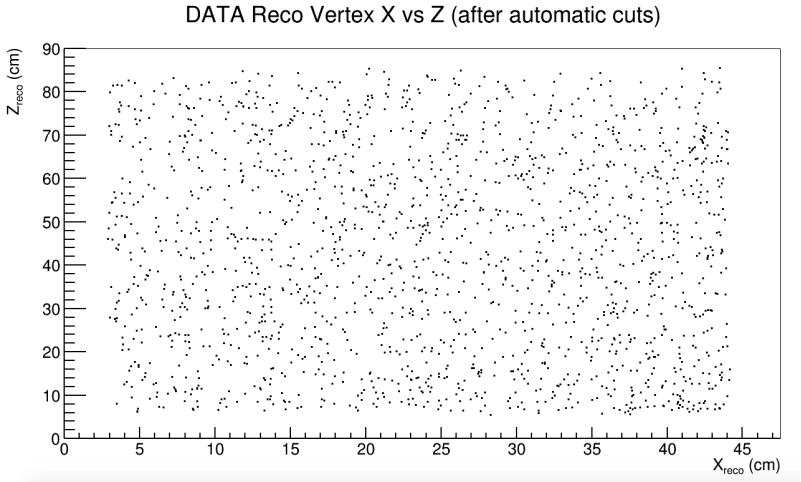

Figure 5.4: *X vs Z vertex distribution of all data events that pass the automatic cuts.*

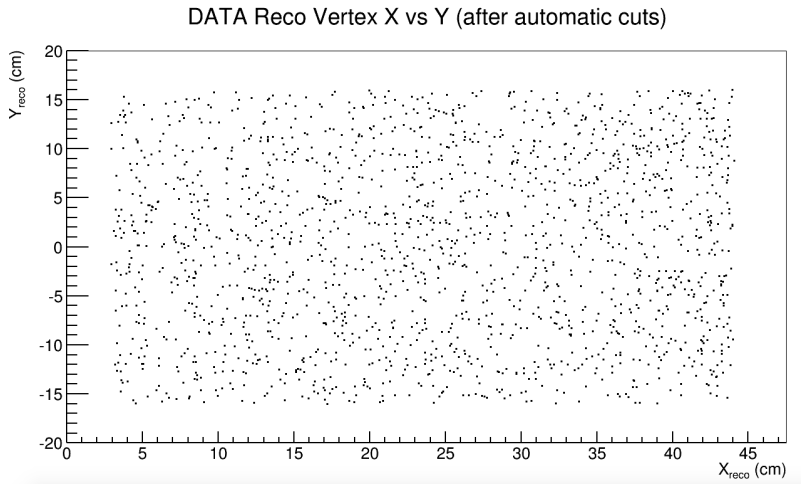

Figure 5.5: *X vs Y vertex distribution of all data events that pass the automatic cuts.*

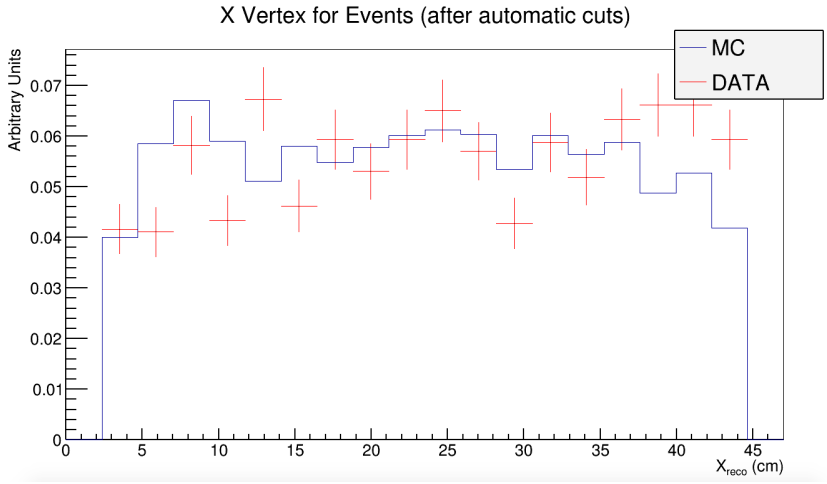

Figure 5.6: *X vertex distribution for reconstructed data and MC that pass automatic cuts. Data and MC plots are both normalized to one.*

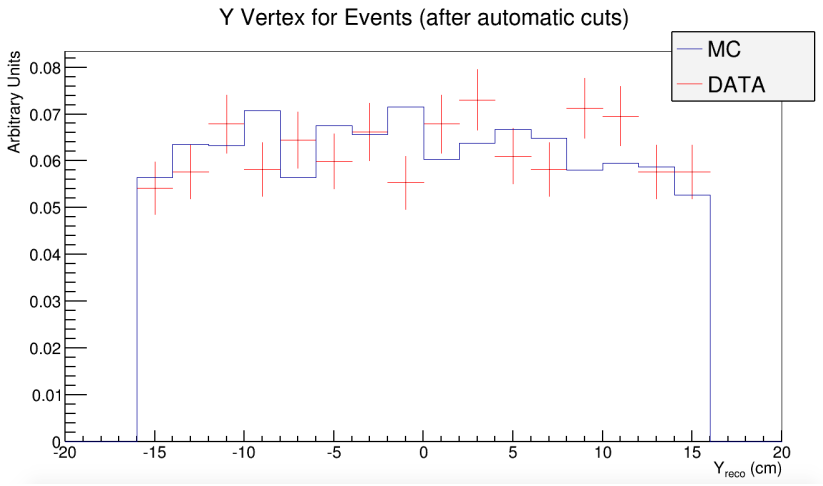

Figure 5.7: *Y vertex distribution for reconstructed data and MC that pass automatic cuts. Data and MC plots are both normalized to one.*

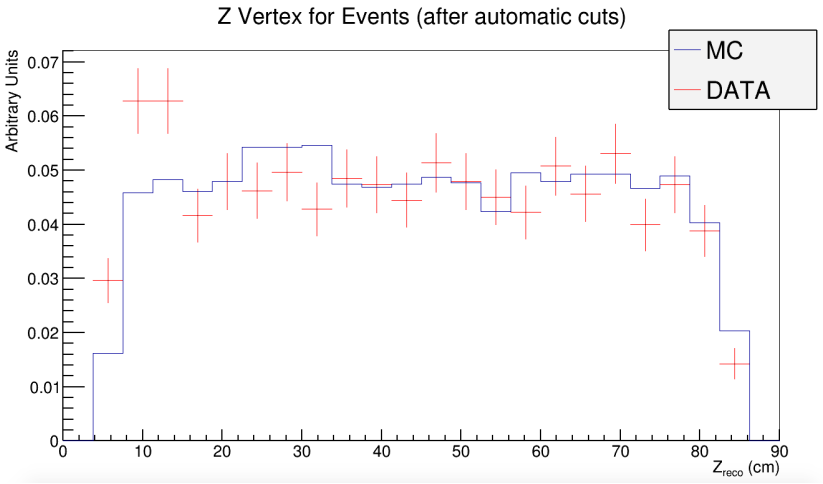

Figure 5.8: *Z vertex distribution for reconstructed data and MC that pass automatic cuts. Data and MC plots are both normalized to one. Through going muons entering the detector are not simulated and are removed from data while visual scanning.*

Track matching with MND is an important element of this analysis, as mentioned before. It helps reject NC background and also helps select antineutrino events based on the charge reconstruction by MND. An ArgoNeuT track that is exiting the TPC is projected to the MND and the cuts are selected based on MC to avoid any wrong match between the tracks.

The angle between the projected ArgoNeuT track and the MND track must be less than 0.4 rad, and the radial distance between them at the MND must be less than 27 cm. Figure 5.9, show the relative size and position of the ArgoNeuT and MINOS detectors. Figure 5.10 shows ArgoNeuT display with a track from ArgoNeuT exiting the TPC and entering MINOS, being matched with the negatively charged track in MINOS. One can also see other tracks in the MINOS for the spill. In case there is more than one match for an ArgoNeuT track, the best match is taken based on the least value of $\Delta r/\cos\theta$; here, Δr is the radial distance between ArgoNeuT projected track and the MND track, and θ is the angle between them. After the geometric matching between tracks is complete, a non-zero momentum and a positive charge reconstruction of the track is required.

Figure 5.11 shows the muon momentum for data and MC events as reconstructed by the ArgoNeuT. Total muon momentum is obtained by adding three measurements; energy deposited in the ArgoNeuT TPC, energy lost between the ArgoNeuT and MND, and the energy deposited in the MND. MND measures the muon momentum which corresponds to the momentum when the muon enters the MND detector. ArgoNeuT corrects for the muon momentum by measuring the energy deposited by a muon as it travels through the TPC, whereas the energy lost by muons between two detectors is estimated using a Geant4-based study. Figure 5.12 shows the energy loss of muon as a function of distance traveled between the two detectors (through the inner and outer cryostat to the MND). The non-linear functionality of energy loss is attributed to the non-homogeneous composition of the materials between the detectors. The muon energy loss is also correlated with its angle but a stronger correlation is found with the distance. The energy lost by a muon traveling a known distance between the two detectors is calculated using the linear fit parameters. Figure 5.13 shows the muon angle for data and MC events as reconstructed by ArgoNeuT. The difference in distribution is due to -3.3^0 difference in neutrino beam angle in MC and data. The MC beam is pointed at 0^0 whereas the NUMI beam is pointed at -3.3^0 to reach the MINOS far detector in Soudan, Minnesota. The effect of the difference in MC and data

is calculated by assigning weights to the MC events in muon angle bins and is assigned as systematic error to the final measurement.

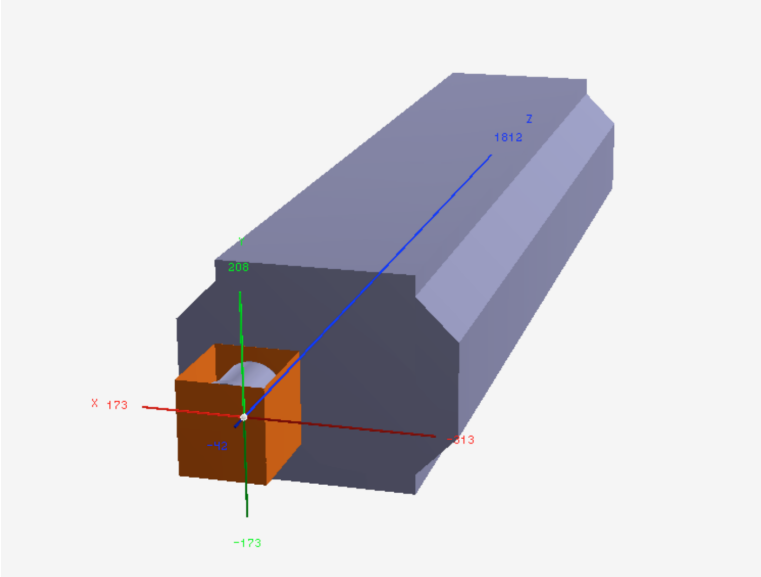

Figure 5.9: *ArgoNeuT (orange) and MINOS (purple); an image showing their relative size and position in the MINOS ND hall at Fermilab. Figure is taken from Ref. [102].*

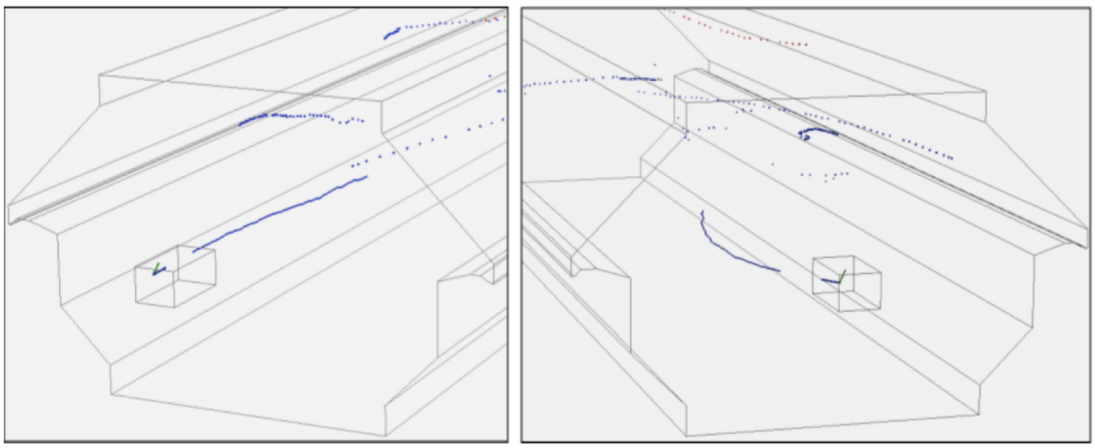

Figure 5.10: *ArgoNeuT's event display, showing tracks in ArgoNeuT and MINOS detectors. A negatively charged track is matched between ArgoNeuT and MINOS. Other tracks in both detectors are also visible for the same spill. Figure from Ref. [75].*

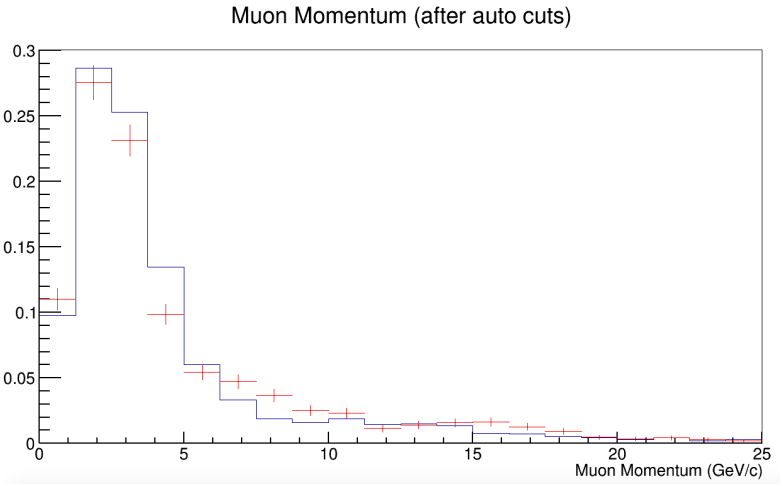

Figure 5.11: *Distribution of muon momentum for all data and MC events that pass the automatic cuts. Data and MC plots are both normalized to one.*

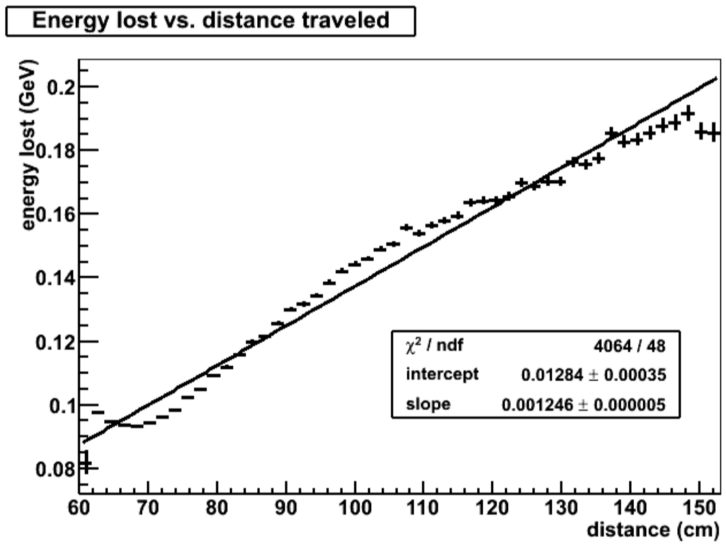

Figure 5.12: *Energy lost by a muon as a function of distance traveled between ArgoNueT TPC and MND as predicted by Geant4-based study. The non-linear functionality is attributed to the non-homogeneous composition of materials between the two detectors. Figure from Ref. [102].*

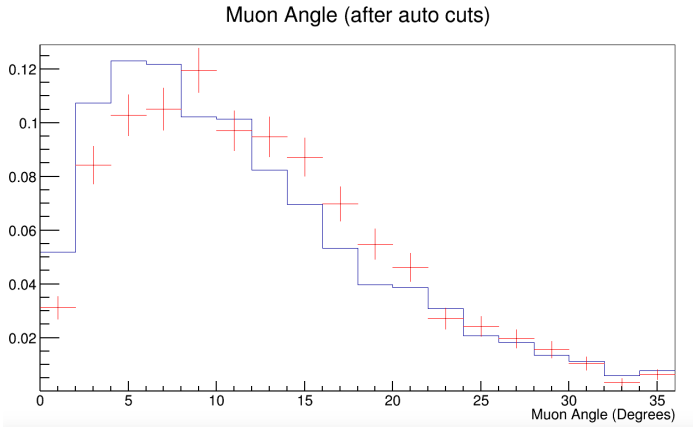

Figure 5.13: *Distribution of muon angle for all data and MC events that pass the automatic cuts. Data and MC plots are both normalized to one.*

The effect of all automatic cuts is 78.7% signal acceptance (ϵ_{cuts}) and 81.3% background rejection. Remember that the 'signal' is defined as the event where a neutral hyperon eventually decays to a proton and a pion. The branching fraction of a Λ^0 or Σ^0 to decay to the charge particles is 63%. After applying all the automatic cuts, a data sample of 1753 events is selected. Figure 5.14 shows the signal acceptance and background rejection rates for the cuts in this analysis.

Cuts	Description	Signal Acceptance	Background Rejection	Data
Automatic Reconstruction Cuts	FV, MM μ^+, MM track begins in FV, Clusters in each view > 1	78.7%	81.3%	1753
Scanning Cuts	Primary tracks = 1,2 Secondary tracks = 2 Detached vertex = 1, 2 Reject events with 2 showers	75.7%	98.6%	36

Figure 5.14: *Signal acceptance and background rejection rates along with the number of data events after each cut.*

Figure 5.15 shows the distribution of number of reconstructed tracks in MC and data after all automatic cuts. Figure 5.16 and Figure 5.17 show the distribution of number of Linemerger clusters in Induction and Collection wire view for MC and data after all automatic cuts, respectively. Figure 5.18 shows the distribution of exiting tracks in MC and data after all automatic cuts. A track is an exiting track if its end point is within 3 cm of the TPC boundary. The data and MC are in agreement. All the plots are normalized to one.

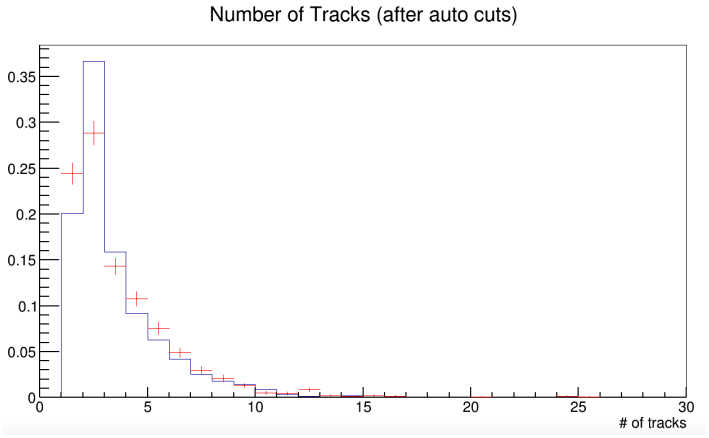

Figure 5.15: *Number of tracks distribution for data and MC after all automatic cuts. Data and MC plots are both normalized to one.*

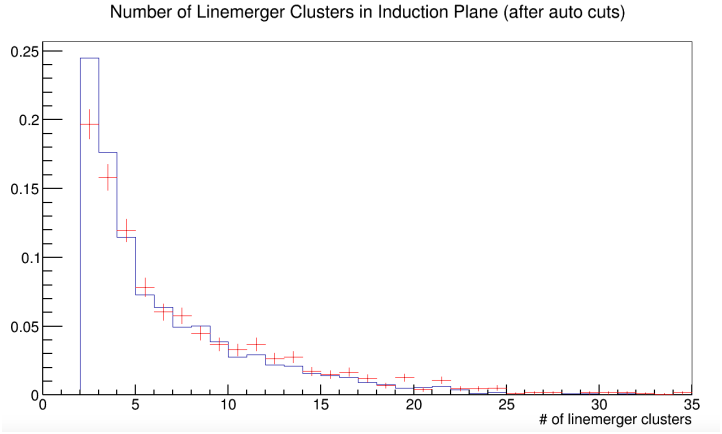

Figure 5.16: *Distribution for the number of Linemerger clusters in Induction wire plane for data and MC after all automatic cuts. Data and MC plots are both normalized to one.*

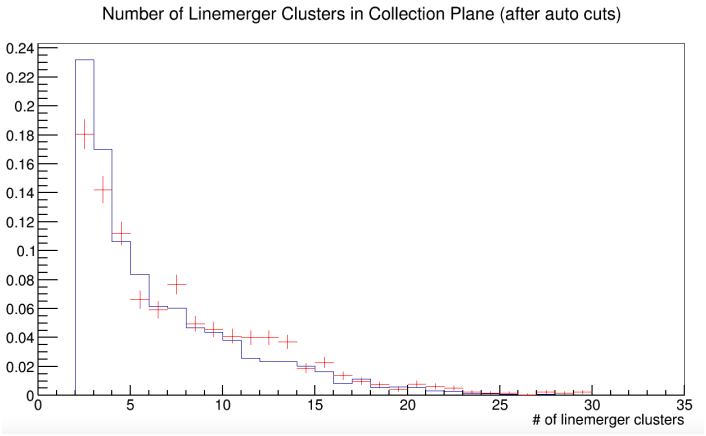

Figure 5.17: *Distribution for the number of Linemerger clusters in collection wire plane for data and MC after all automatic cuts. Data and MC plots are both normalized to one.*

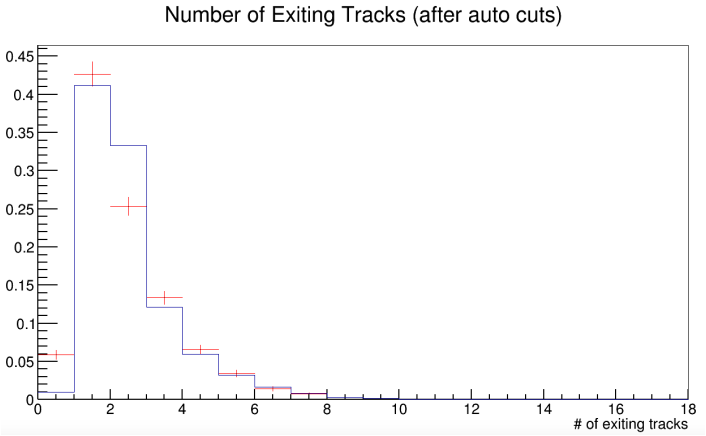

Figure 5.18: *Distribution for the number of exiting tracks for data and MC after all automatic cuts. Data and MC plots are both normalized to one.*

5.2.2 Visual Scanning

The second step of the analysis is the visual scanning. Events that pass the automatic cuts are visually scanned by a scanner. During the visual scanning the scanner is asked to fill in the topological information about the event. The ArgoNeuT event display showing a CCQE Λ^0 event and a scan window that scanner fills for each event is shown in Figure 5.19 and

Figure 5.20, respectively.

The scanning process proceeds as follows; the scanner zooms-in to the primary vertex and counts and records the number of primary tracks. He or she then looks for any detached vertex in the event. If located, the scanner counts the number of tracks from the detached vertex (named as secondary tracks) and record the information in the scan window. In the case of more than one detached vertices, the scanner picks up the vertex that has the most straight tracks originating from it. Event display tool also allows the scanner to reject events with through-going muons by finding the 3D start point of the track and determine if it the track is entering.

1. 1 or 2 primary tracks,
2. exactly 2 secondary tracks,
3. no 2 or more showers.

are selected. After applying these scanning cuts, 36 data events are selected.

A very simple example MC event (CCQE Λ^0) is shown in the Figure 5.19, where one can see a detached vertex having two secondary tracks originating from it. The scanner will fill the information as 1 primary track, 1 detached vertex, 2 secondary tracks in an event, with checking No in the '2 or more Showers in Event' field. A set of 1081 MC events that pass all automatic cuts is scanned using the same rules as on data. The efficiency of picking up the signal events (ϵ_{scan}) is 75.7% whereas the background rejection rate is 98.6%. The smaller efficiency of picking up rather simple topology signal events is attributed to when the hyperon decays very close to the primary vertex. If the primary and detached tracks are very close and also parallel to each other in the wire plane, the scanner can only distinguish between them if the start point of both is at least three hits apart. The signal selection and background rejection rates predict 10 signal events and 20 background events for the MC scaled to 1.2 x 10^{20} protons-on-target (POT) in the final selected data sample.

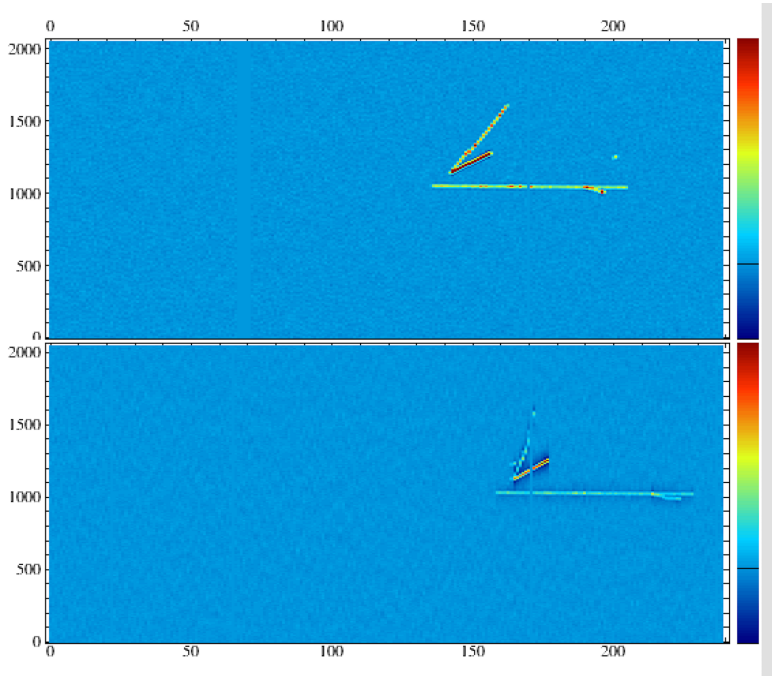

Figure 5.19: *ArgoNeuT MC, CCQE Λ^0 production. A detached vertex is visible with two secondary tracks.*

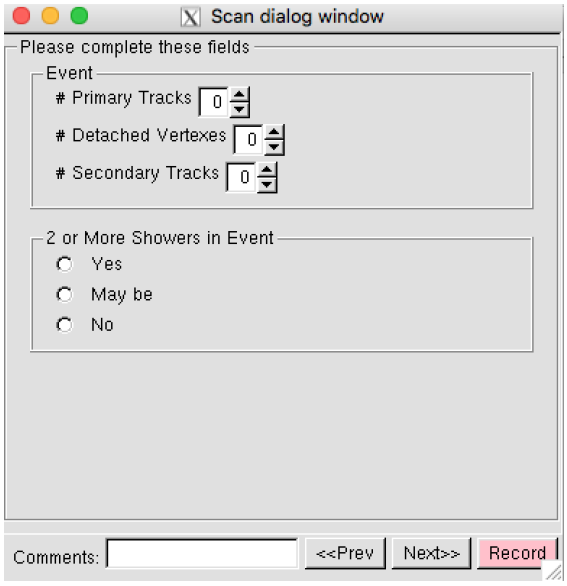

Figure 5.20: *Scan window, the fields are filled by the scanner during the visual scanning of the neutrino events.*

Figure 5.21 shows the distribution of number of reconstructed tracks for MC and data events after they pass the scanning cuts. The distributions of Linemerger clusters are seen in Figure 5.22 and Figure 5.23 for induction and collection wire plane after scanning, respectively. Also, the distribution of exiting tracks for MC and data events that pass all scanning cuts is shown in Figure 5.24. According to MC prediction, the decay particles in the signal events, a proton and a pion from a neutral hyperon, both exit the TPC 40% of times: 19% events have only the proton exiting, 10% of events have only pion exiting; and both the proton and pion stop in the TPC in 31% of events. Figure 5.25 - Figure 5.31 show few ArgoNeuT data events selected after the scanning cuts.

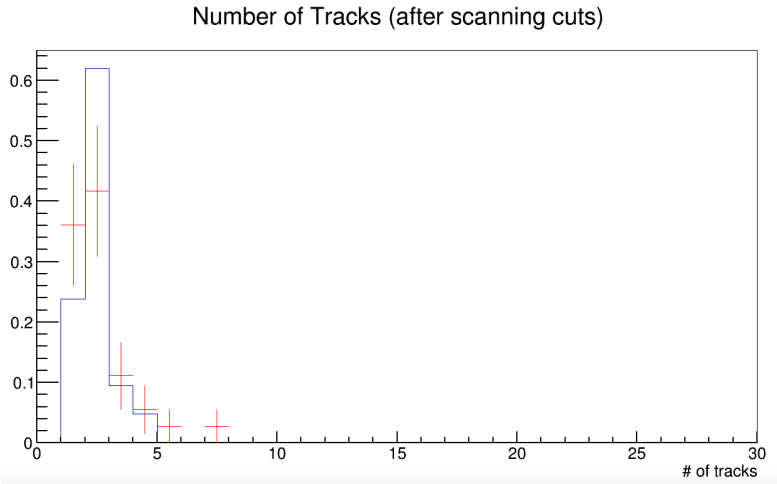

Figure 5.21: *Number of tracks distribution for data and MC after scanning cuts. Data and MC plots are both normalized to one.*

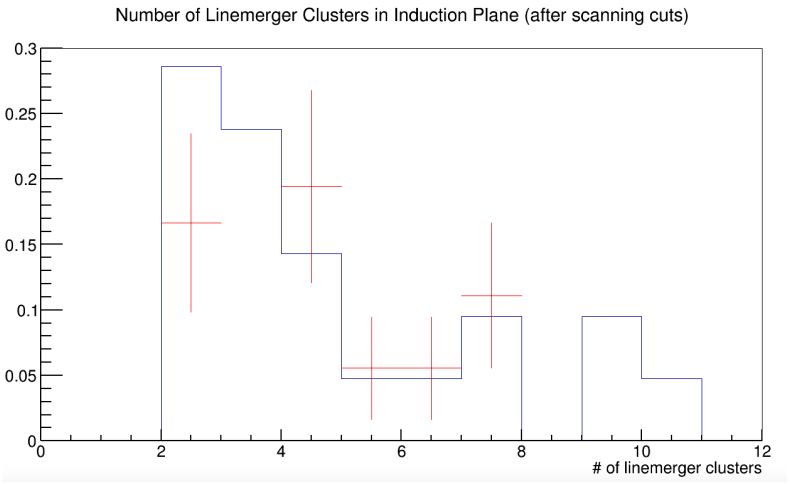

Figure 5.22: *Distribution for the number of Linemerger clusters in induction wire plane for data and MC after scanning cuts. Data and MC plots are both normalized to one.*

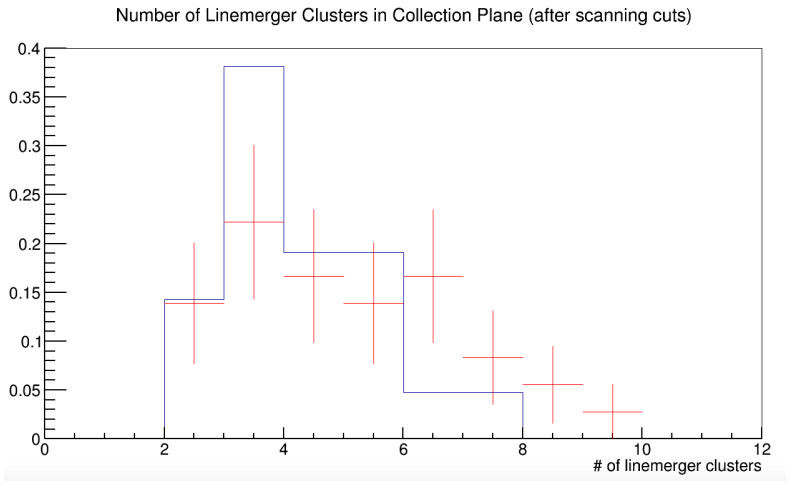

Figure 5.23: *Distribution for the number of Linemerger clusters in collection wire plane for data and MC after scanning cuts. Data and MC plots are both normalized to one.*

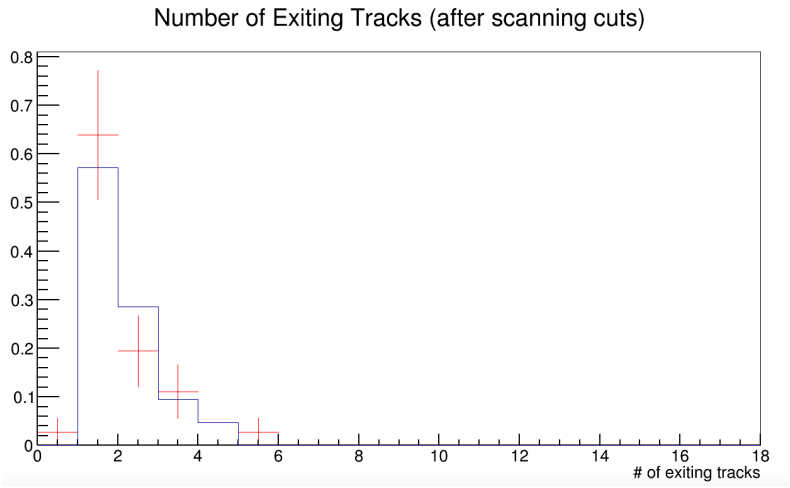

Figure 5.24: *Distribution for the exiting tracks for data and MC after scanning cuts. Data and MC plots are both normalized to one.*

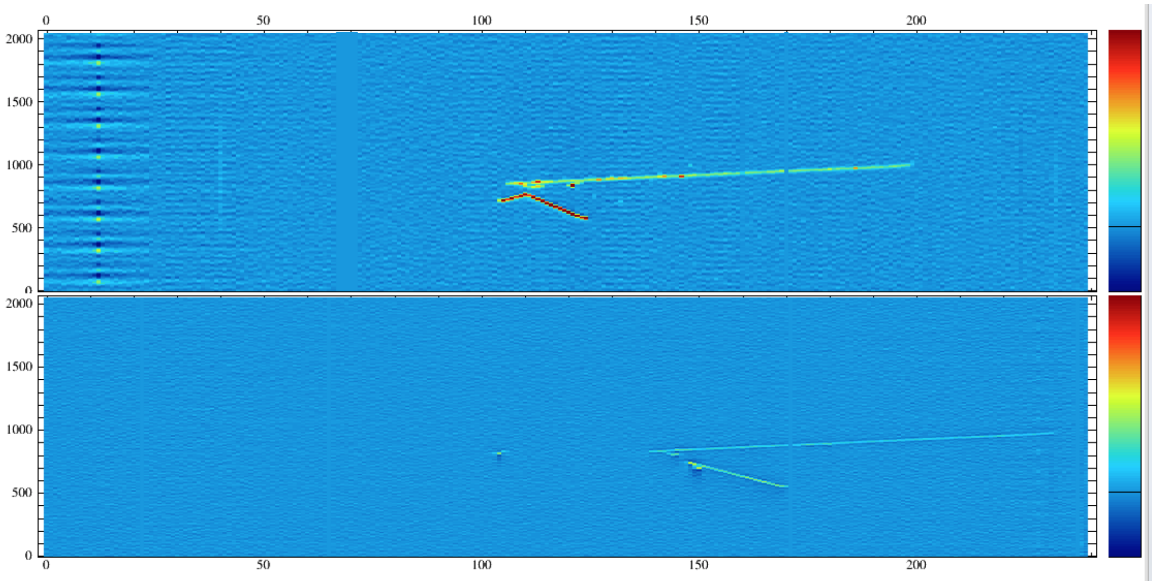

Figure 5.25: *Data event selected after scanning cuts.*

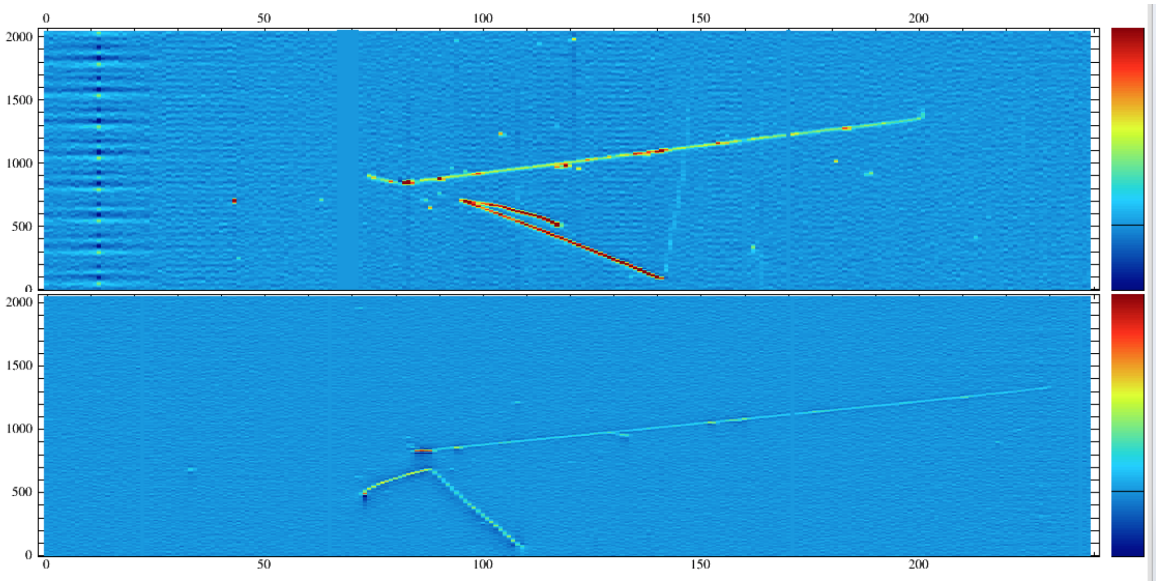

Figure 5.26: *Data event selected after scanning cuts.*

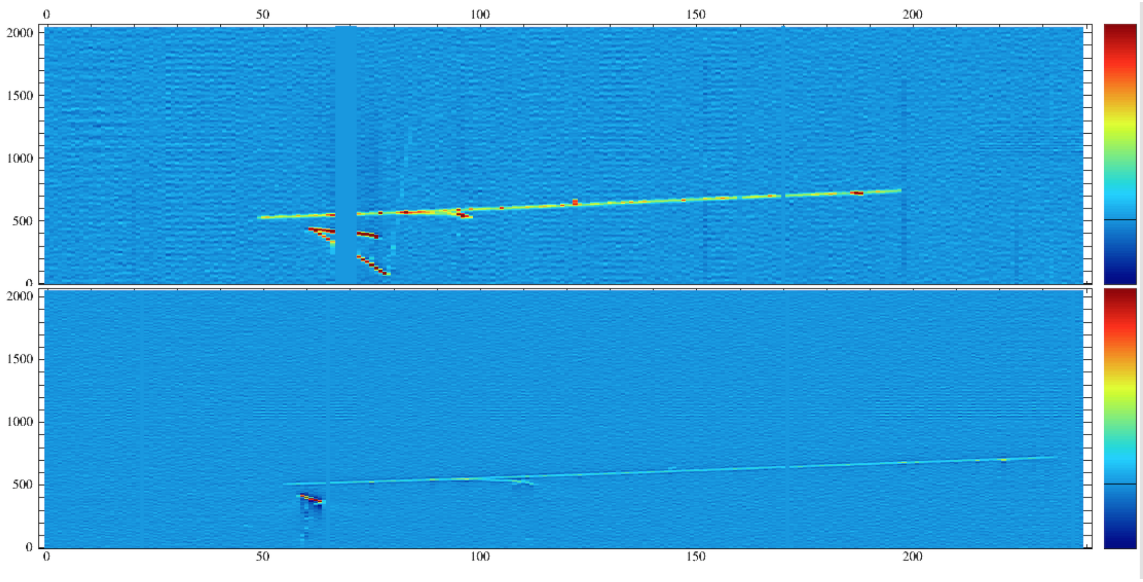

Figure 5.27: *Data event selected after scanning cuts. Five consecutive dead channels in the collection plane of the ArgoNeuT are visible as a 'gap' in the tracks.*

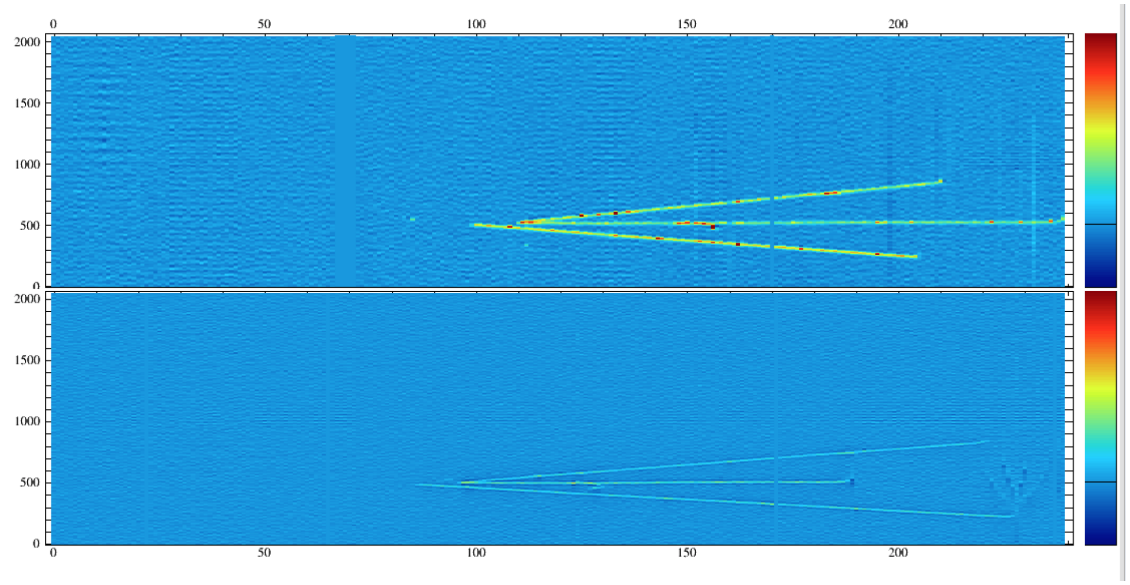

Figure 5.28: *Data event selected after scanning cuts.*

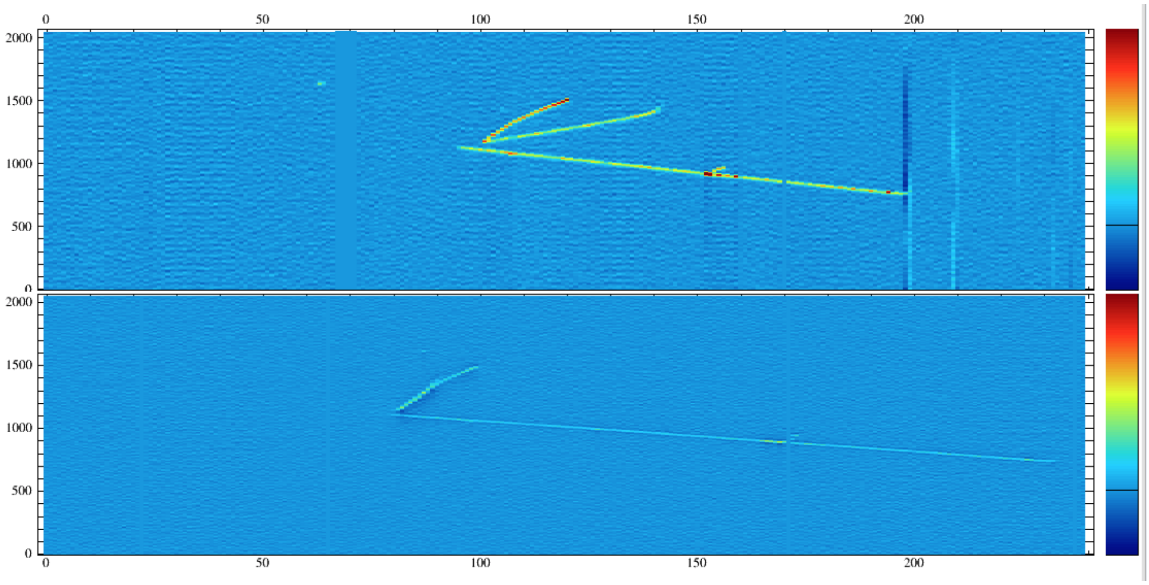

Figure 5.29: *Data event selected after scanning cuts.*

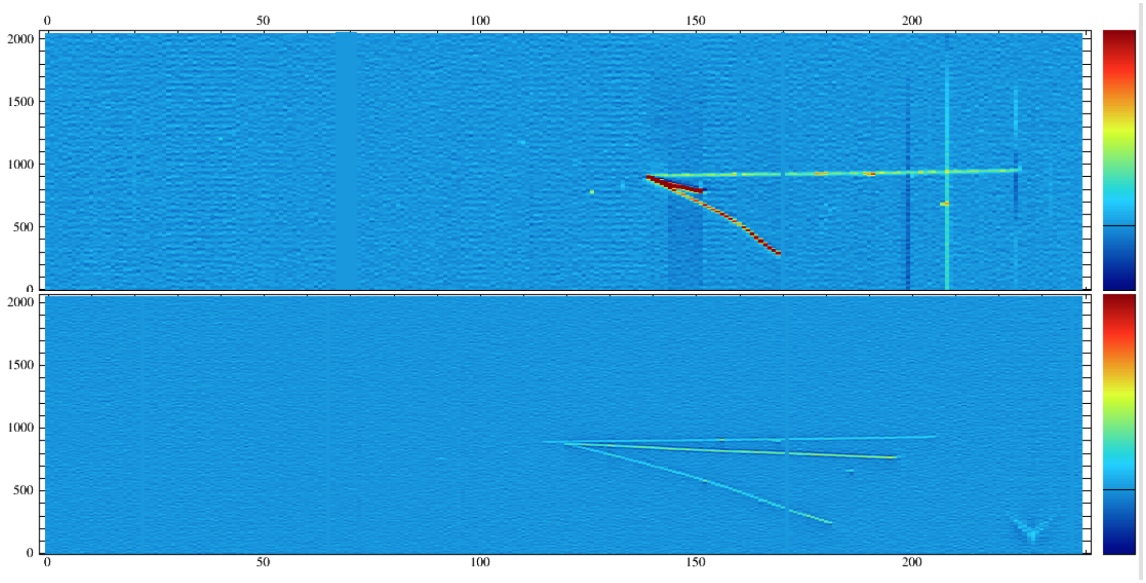

Figure 5.30: *Data event selected after scanning cuts.*

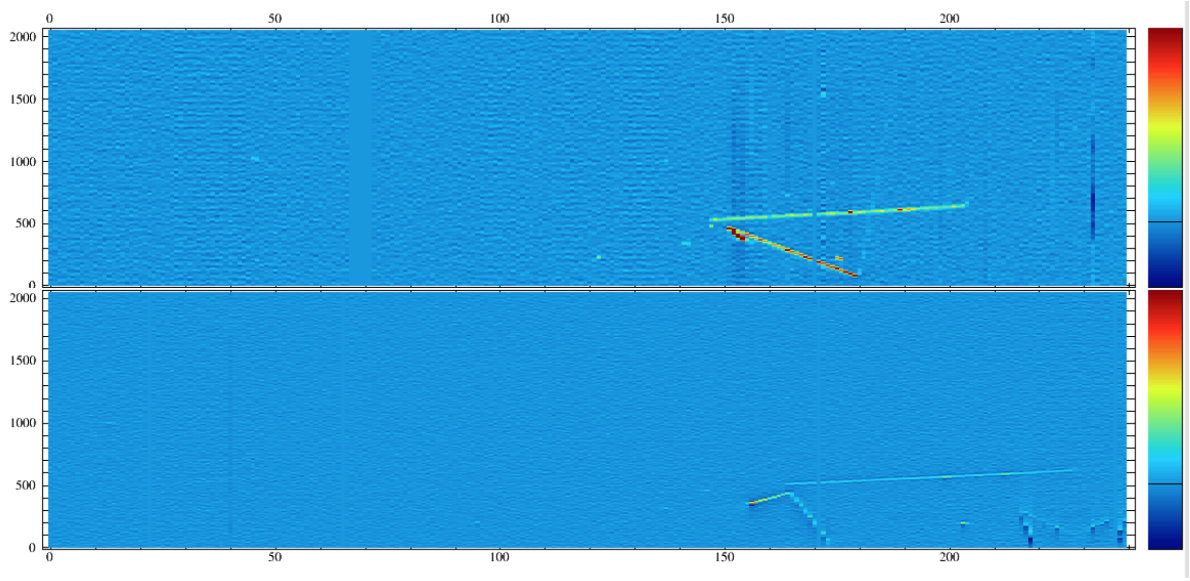

Figure 5.31: *Data event selected after scanning cuts.*

The visual scanning of events allows for determining the 3D quantities in an event, such as separation between the primary and detached secondary vertex; 'vertex separation', the opening angle and lengths of the two secondary tracks. Figure 5.32 shows the 3D vertex

separation in the data and MC events after scanning cuts. Figure 5.33 show the 3D opening angle of the secondary tracks in data and MC events after scanning cuts. Figure 5.34 and Figure 5.35 show 3D length of the longer secondary track and the 3D length of the shorter secondary track in the data and MC events, respectively.

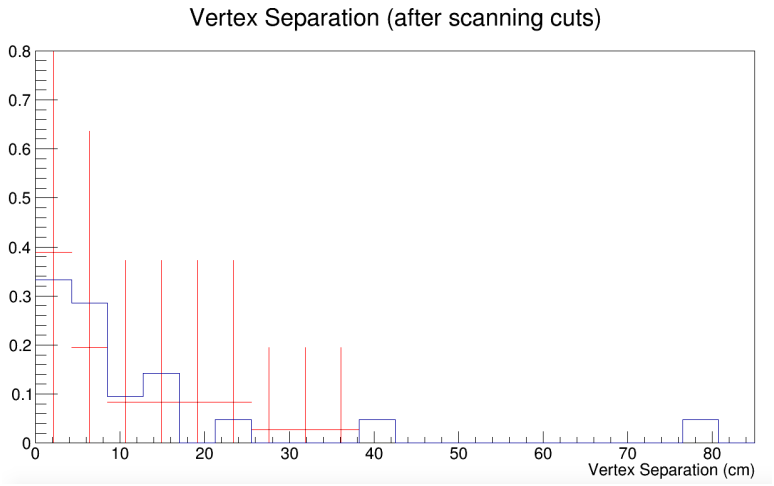

Figure 5.32: *Vertex separation – the distance between primary and the secondary detached vertex in the data and MC events after scanning cuts. Data and MC plots are both normalized to one.*

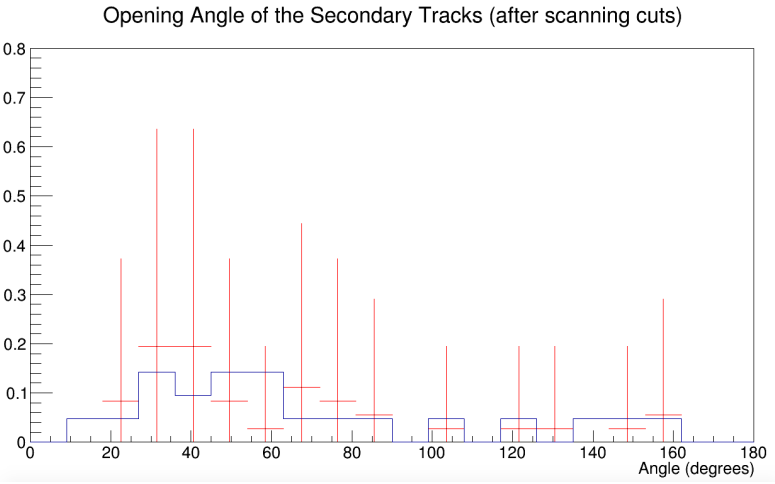

Figure 5.33: *3D opening angle of the secondary tracks in the data and MC after scanning cuts. Data and MC plots are both normalized to one.*

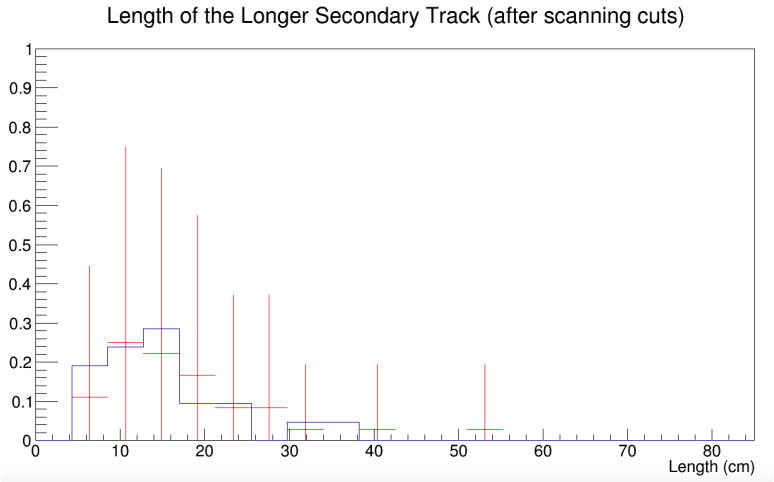

Figure 5.34: *Length of the longer secondary track in the data and MC after scanning cuts. Data and MC plots are both normalized to one.*

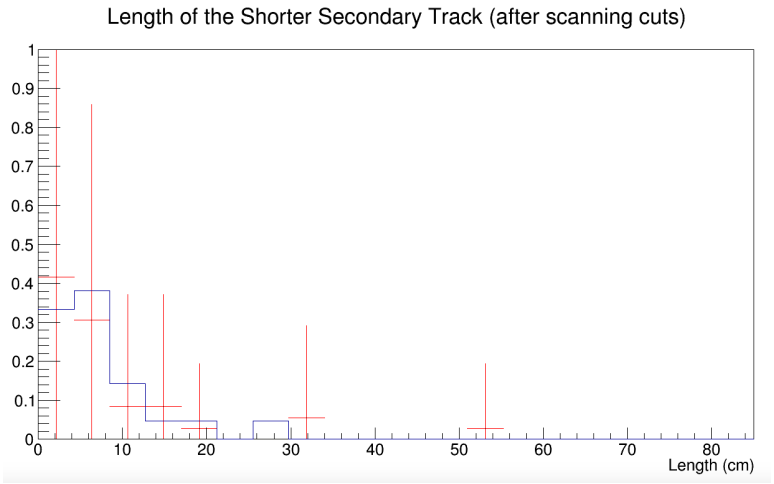

Figure 5.35: *Length of the shorter secondary track in the data and MC after scanning cuts. Data and MC plots are both normalized to one.*

5.3 Background

The background is calculated by normalizing the MC to 1.2×10^{20} protons-on-target (POT). Any event in MC that passes all the analysis cuts but is not a CCQE neutral hyperon event

shown in Equation 5.1. Background events are in which the scanner sees a detached vertex with two tracks originating from it along with one or two primary tracks. One example of such event is charge current deep inelastic (CCDIS) interaction, where particles such as K^0, Σ^0 or Λ^0 are produced in pairs and one of them exits the detector without decaying, or decays to neutral particles. Another example could be when a charged hyperon is produced along with a neutral one in a CCDIS or neutral current deep inelastic (NCDIS) interaction. Other examples would include events when a neutron produced in the primary interaction scatters off of an argon nucleus and produce exactly two tracks in the detector. A total of 64% of the total background is such processes.

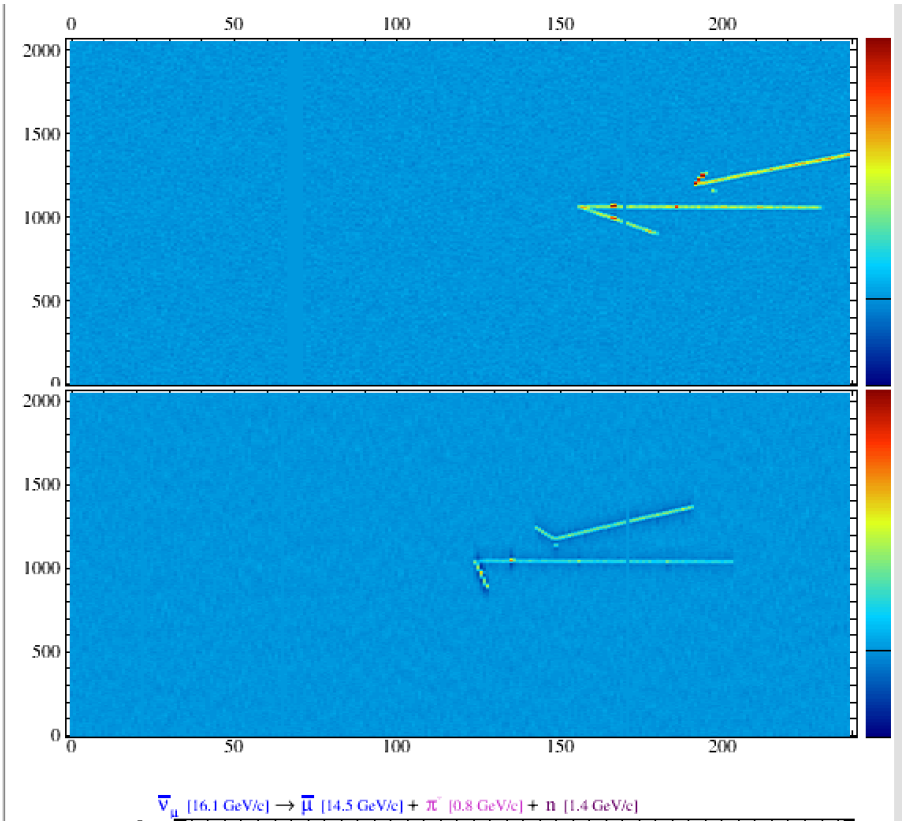

Figure 5.36: *An example of a background event (after scanning cuts).*

Based on the scanned MC sample, 7% of the background comes from CCQE interactions, 50% from NC/CCDIS, 43% from CC-resonant interactions. The event rates for each inter-

action are calculated by convolving the cross section from NUANCE and flux histograms. After scaling the MC to 1.2 x 10^{20} protons-on-target (POT), 20 background events are predicted. Figure 5.36 and Figure 5.37, each show an example of background event that is selected during the visual scanning. Figure 5.36 shows an event where a neutron scatters to produce a detached vertex with two secondary tracks. Figure 5.37 shows an example where a K^0 and Λ^0 are produced (associated production) and one of them decays to charge particles inside the TPC.

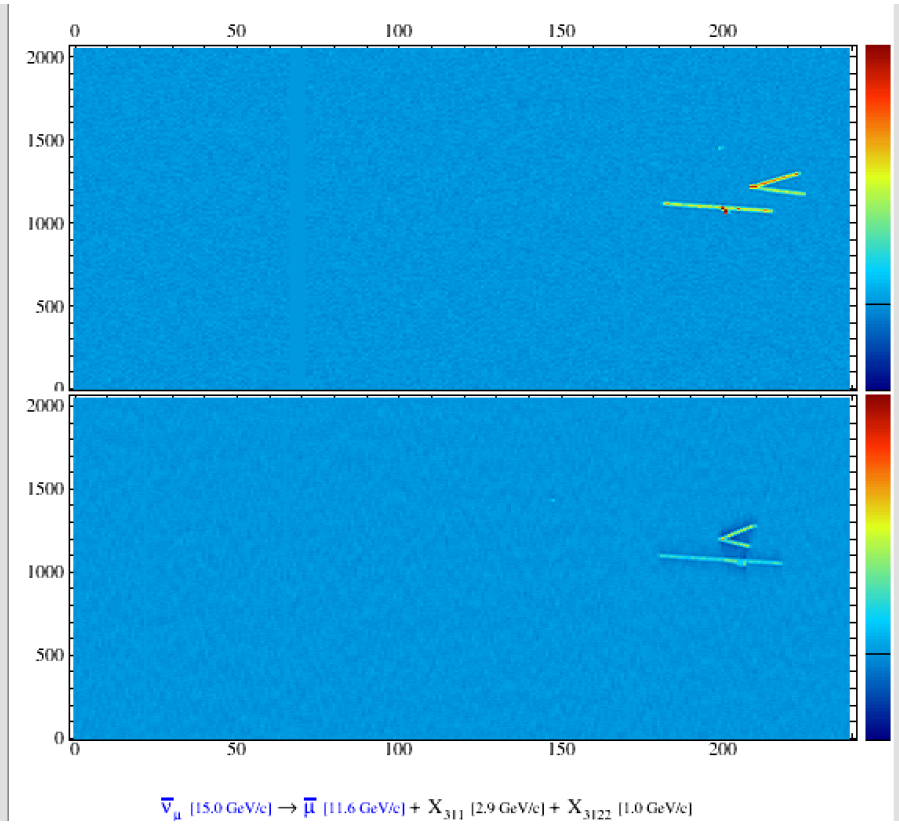

Figure 5.37: *An example of a background event (after scanning cuts).*

5.4 Flux

The flux in the antineutrino NUMI beam mode in low energy (LE) is shown in the Figure 5.38.

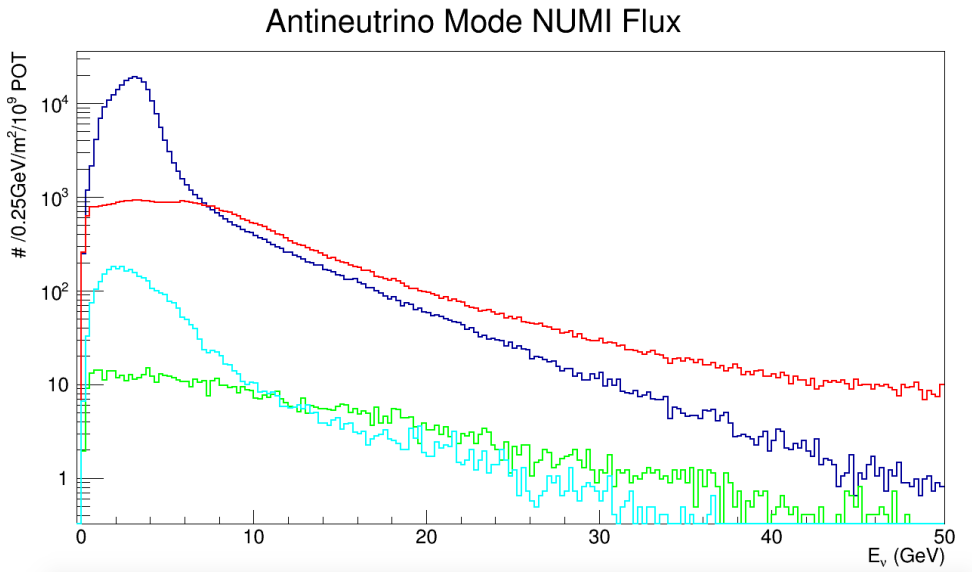

Figure 5.38: *Antineutrino flux of ν_μ(red), $\bar{\nu_\mu}$(blue), ν_e(green) and $\bar{\nu_e}$(cyan) in the low energy (LE) antineutrino-mode NUMI beam [**?**].*

The analysis uses total integrated flux of 2.4 $\times$ 10^5 $\bar{\nu_\mu}/\mathrm{m}^2/10^9$POT [**?**] for the antineutrino-mode beam. ArgoNeuT took 1.25 $\times$ 10^{20} POT in the antineutrino-mode run. However, since the analysis makes use of the muon track information from MINOS, which demands to correct for the amount of POT when both the detectors were active, hence 1.20 $\times$ 10^{20} POT are used in this analysis.

5.5 Errors

The statistical error is dominant in this analysis and is due to the small number of events. The error on the number of selected data events and the predicted background events, error on efficiency of automatic reconstruction cuts and scanning cuts contribute to the statistical errors;

$$\left(\frac{\delta\sigma_{stat}}{\sigma}\right)^2 = \left(\frac{\delta N_{data}}{N_{data}-N_{bkg}}\right)^2 + \left(\frac{\delta N_{bkg}}{N_{data}-N_{bkg}}\right)^2 + \left(\frac{\delta\epsilon_{cuts}}{\epsilon_{cuts}}\right)^2 + \left(\frac{\delta\epsilon_{scan}}{\epsilon_{scan}}\right)^2. \quad (5.3)$$

The first two terms in the Equation 5.3 dominate the total (statistical) error. Their contribution to the total (statistical) error are 37% and 33%, respectively. Error on the background comes from the uncertainties in the background selection efficiencies of each cut on the MC sample and the uncertainty in the NUANCE scaling factor (to scale the MC to the 1.2×10^{20} protons-on-target). Binomial errors are considered for all the efficiencies.

Although the analysis is statistically limited, systematic errors from prominent sources are also calculated and accounted for. Equation 5.4 shows different contributions to the systematic error on the cross section measurement. The flux is assigned a flat 11% uncertainty that accounts for the uncertainty in hadron production and beamline modeling [**?**]. Systematic error introduced due to visual scanning is also taken into account. A set of 4680 data events that pass automatic reconstruction cuts (excluding muon sign requirement) is scanned by two scanners. The scanning cuts are then applied to the events and considering the number of common events that the scanners selected out of the total number of events that each of them selected, the maximum difference in their selection efficiency is calculated to be 3.5%. The difference between beam angle in MC and data also introduces systematic error. The MC events after passing all cuts are weighted in the muon angle bins and an error of 6% is assigned. The systematic error due to the fiducial volume cut is calculated by increasing and decreasing 1 cm on all sides of the fiducial volume (FV). The maximum difference in the event density (number of events per unit volume) is determined to be 1%. Systematic error on the POT count is 1% [103]. Error associated with the number of targets is 2% [10]. Background prediction uncertainty is also included in the systematic error.

There are two estimates of the background, which are consistent (and have same mean value of 20 estimated events, likely a coincidence); one is the estimated background from MC after applying all analysis cuts. A conservative estimate of 50% uncertainty is assigned on the background prediction from NUANCE model. The second estimate of the background comes from the shape fit (described in the next section), which also gives the uncertainty in the number of background events. Combining the two uncertainties, a total systematic

error in the background prediction is found to be 39%, which is the biggest contribution to the systematic error.

$$\left(\frac{\delta\sigma_{syst}}{\sigma}\right)^2 = \left(0.11\ _{\text{flux}}\right)^2 + \left(0.035\ _{\text{scan}}\right)^2 + \left(0.01\ _{\text{FV}}\right)^2 + \left(0.01\ _{\text{POT}}\right)^2 + \left(0.02\ _{\text{N}_{targ}}\right)^2 + \left(0.06\ _{\text{angle}}\right)^2 + \left(0.39\ _{\text{bkg}}\right)^2. \tag{5.4}$$

5.6 The Measurement

This analysis measures the total cross section for charge current quasi-elastic neutral hyperon production and sets an upper limit to the cross section at 90% confidence-level. Two independent approaches are used to make the measurement. The first is model dependent (absolute normalization to the cross section model), and the second one is nearly model independent and uses only the shape distributions for MC signal and background.

The cross section generally can be written in the form of Equation 5.7. One can write the expression for cross section for this specific analysis;

$$\sigma(_{CCQE_{\Lambda^0+\Sigma^0}}) = \frac{f \times (N_{data} - N_{bkg})}{\phi \times N_{targ} \times \epsilon_{cuts} \times \epsilon_{scan}}. \tag{5.5}$$

Here, N_{data} is the number of total data events that pass all the cuts in analysis, N_{bkg} is the predicted number of background events, ϕ is the integrated antineutrino flux of the NUMI beam in antineutrino mode, N_{targ} is the number of targets in the fiducial volume of the detector, and ϵ_{cuts} and ϵ_{scan} are the efficiencies of the automatic cuts and the scanning cuts, respectively. f is the correction factor for the branching ratio of neutral hyperon decay to the neutral particles. Using the model dependent approach, after plugging in all the values as shown in the table in Figure 5.39, the measured cross section is

$$\sigma(_{CCQE_{\Lambda^0+\Sigma^0}}) = \left(3.7 \pm 1.9(\text{stat.}) \pm 1.5\ (\text{sys.})\right) \times 10^{-40}\ \text{cm}^2. \tag{5.6}$$

The observed excess in the event yield is consistent with the expectation of CCQE Λ^0 and Σ^0 production in the model. A common convention in high energy physics is that a measurement is considered statistically significant observation if it is at least three standard deviations (3σ) away from zero, which is not the case here, hence the study sets a 90% confidence-level (C.L.) upper limit on the total cross section of CCQE Λ^0 and Σ^0 production following the procedure described in [104].

$$\sigma(_{CCQE_{\Lambda^0+\Sigma^0}}) \quad < \quad 7.3 \times 10^{-40} \text{ cm}^2 \text{ at } 90\% \text{ C.L.} \tag{5.7}$$

N_{data}	36
N_{bkg}	20
f	100/63
ϕ	2.88×10^{12} $\bar{\nu}_\mu$/cm^2
N_{targ}	2.21×10^{27} x 18 nucleons
ϵ_{cuts}	0.787
ϵ_{scan}	0.757

Figure 5.39: *Numbers for cross section calculation. N_{data}, N_{bkg} and N_{targ} correspond to fiducial volume (FV) of the TPC.*

For consistency check, the measured total cross section of CCQE Λ^0 and Σ^0 production by the model dependent method, shape fits are employed on the MC signal and background events. This method estimates the number of signal and backgrounds events in the selected data events without relying on the absolute normalization to the cross section model, and using only the signal and background shapes from the MC. The vertex separation distributions for MC signal and MC background events (selected after all analysis cuts) are each fitted with an exponential function and the combination of both is fitted to the 36 data events that passed all cuts. Figure 5.40 show the fits for signal, background and data. This method predicts 16±8 signal events and 20±8 background events, with a fit $\chi^2/d.o.f. = 0.08$.

The central value of the result matches with the results from the model dependent method but gives bigger errors. The statistical errors come from the data statistics and the limited MC statistics. More MC signal and MC background statistics can improve the precision in shape descriptions for signal model and background model. Systematic errors on this measurement also come from Equation 5.4. We exclude the last term in the equation since for this (model-independent) method, systematics from the model are much reduced. The cross section measurement from this method gives

$$\sigma(_{CCQE_{\Lambda^0+\Sigma^0}}) = \left(3.7\ ^{+3.2}_{-2.9}(\text{stat.})\ \pm 0.5\ (\text{sys.})\right) \times 10^{-40}\ \text{cm}^2. \tag{5.8}$$

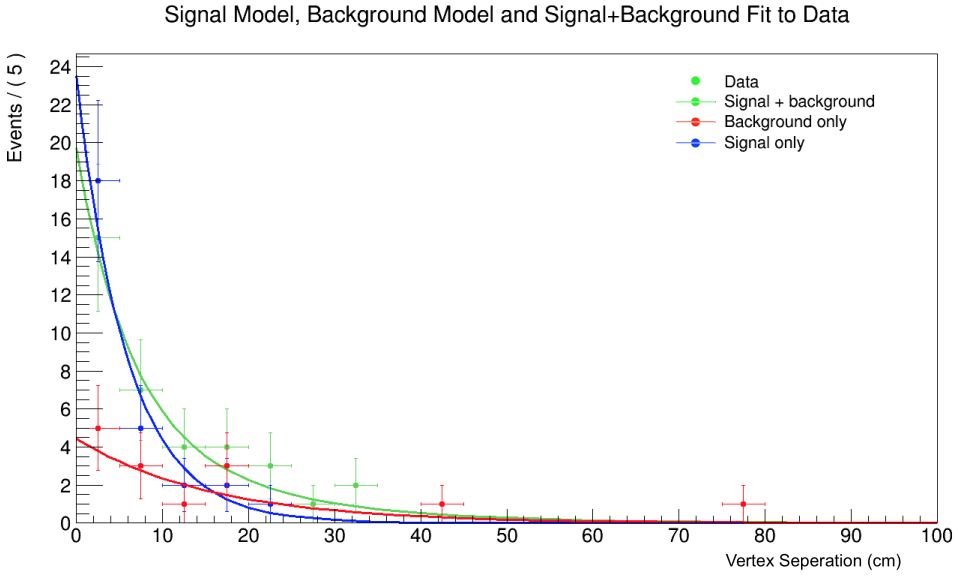

Figure 5.40: *MC signal model (blue), MC background model (red) and signal + background model (green) fit to data events (after scanning cuts). Roofit provides the estimates of signal and background events in the data events that pass all analysis cuts. MC signal and MC background models are normalized to the number of MC events in each category (after scanning cuts).*

Another way of presenting the result is the ratio of CCQE hyperon production cross section to CCQE neutron production cross section at the mean production energy of CCQE hyperons (3.42 GeV), $\sigma(_{CCQE_{\Lambda^0+\Sigma^0}})/\sigma(_{CCQE_n})$. The 90% C.L. upper limit on this ratio is

also reported. The upper limit is calculated as described before for the calculation of upper limit of the total cross section in Equation 5.7. Many model dependencies associated with NUANCE cancel when reporting the result as a ratio. $\sigma(_{CCQE_n})$ cross section is taken directly from NUANCE model.

$$\frac{\sigma(_{CCQE_{\Lambda^0+\Sigma^0}})}{\sigma(_{CCQE_n})} = 0.06 \pm 0.03(\text{stat.}) \pm 0.02 \text{ (sys.)}. \tag{5.9}$$

$$\frac{\sigma(_{CCQE_{\Lambda^0+\Sigma^0}})}{\sigma(_{CCQE_n})} < 0.12 \text{ at } 90\% \text{ C.L.} \tag{5.10}$$

The errors on the measurement are the same as reported in Equation 5.6, neglecting a relatively small error on the predicted value of $\sigma(_{CCQE_n})$. The measured value of this ratio is consistent with the predicted value from NUANCE model, $\sigma(_{CCQE_{\Lambda^0+\Sigma^0}})/\sigma(_{CCQE_n}) = 0.04$ at 3.42 GeV.

5.7 Results

The analysis gives the first measurement of the CCQE neutral hyperon production cross section using data from ArgoNeuT; a LArTPC detector exposed to low energy neutrino beam and sets an upper limit, at 90% C.L., on the total cross section of CCQE neutral hyperon production. The analysis employs two separate methods to measure the cross section. First, using the absolute normalization to the cross section model to predict the background events, and second, using the MC shapes of the signal and background to predict the number of signal and background events in the selected data sample. The analysis is statistically limited; however, both methods give the same mean value with the latter having bigger errors than the former. The event selection is based on two steps, automatic reconstruction cuts and the visual scanning cuts. This is a topological analysis that looks for the events with no more than two primary tracks and a detached vertex with exactly two secondary tracks

and rejects events with two or more showers. The cross section measurement is reported at the average energy of the CCQE neutral hyperon production. Figure 5.41 shows the energy distribution of these events in MC. The distribution is fitted with a Gaussian, which gives 3.42 GeV as the mean energy of these interactions. The measured total cross section is reported in Figure 5.42 at the mean production energy. A ratio of CCQE Λ^0 and Σ^0 total cross section to CCQE neutron cross section is also reported.

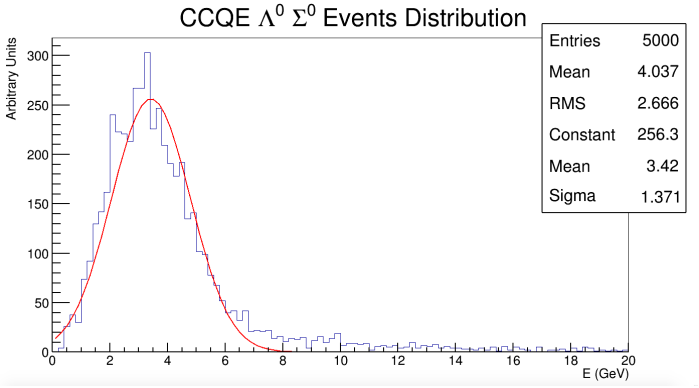

Figure 5.41: *Energy distribution of CCQE neutral hyperon interactions (MC) in ArgoNeuT.*

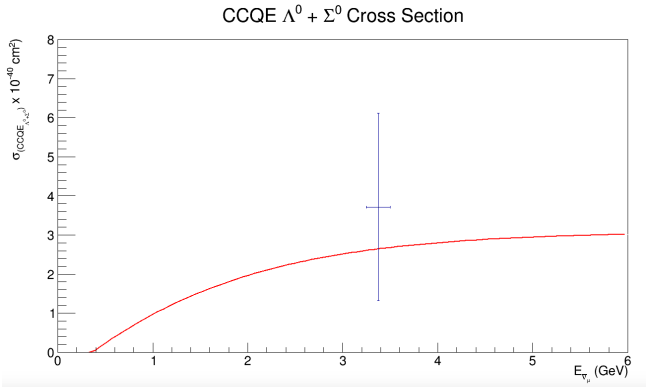

Figure 5.42: *Total cross section of charge current quasi-elastic Λ^0 and Σ^0 production from the NUANCE model (red line) and the measured in this study (blue line). Errors are from the MC dependent method of the measurement. Error bars include statistical and systematic errors. The measurement is consistent with the expectation.*

5.8 Conclusion

The first measurement of CCQE neutral hyperon production cross section in a liquid argon time projection chamber (LArTPC) is presented in this thesis. The analysis uses 1.20×10^{20} protons-on-target (POT), in the NUMI beam operating in the low energy antineutrino mode. The total cross section measurement is reported at the mean production energy of 3.42 GeV for CCQE neutral hyperons. The results are consistent with the NUANCE cross section model. The study sets an upper limit on the total cross section at 90% confidence-level. Also a ratio of CCQE Λ^0 and Σ^0 total cross section to CCQE neutron cross section is reported. The study is statistically-limited which is attributed to the following factors. The process studied here is naturally suppressed by a factor of $\sin^2\theta_c$ as compared to CCQE neutron production process, where θ_c is Cabibbo angle. Other obvious reasons are the small size of ArgoNeuT detector and its short runtime (about five months). These results can be improved by studying these processes in the current and future bigger LArTPC detectors (with higher proportion of contained events), intense neutrino beams, and longer runtimes. Since these processes are induced only by antineutrinos, these can serve as 'antineutrino tagger' in those detectors. In future, this study will be extended by improving short track reconstruction, and automatic particle identification and developing techniques of particle identification for exiting tracks.

Bibliography

[1] W. Pauli, December 4th (1930).

[2] E. Fermi, Zeitschrift für Physik **88**, 161 (1934).

[3] C. Cowan, F. Reines, F. Harrison, H. Kruse, and A. McGuire, Science **124**, 103 (1956).

[4] G. Danby, J. Gaillard, K. Goulianos, L. Lederman, N. Mistry, M. Schwartz, and J. Steinberger, Physical Review Letters **9**, 36 (1962).

[5] K. Kodama, N. Ushida, C. Andreopoulos, N. Saoulidou, G. Tzanakos, P. Yager, B. Baller, D. Boehnlein, W. Freeman, B. Lundberg, et al., Physics Letters B **504**, 218 (2001).

[6] C.-S. Wu, E. Ambler, R. Hayward, D. Hoppes, and R. P. Hudson, Physical review **105**, 1413 (1957).

[7] R. Smith and E. J. Moniz, Nuclear Physics B **43**, 605 (1972).

[8] M. Goldhaber, L. Grodzins, and A. Sunyar, Physical Review **109**, 1015 (1958).

[9] F. Hasert, S. Kabe, W. Krenz, J. Von Krogh, D. Lanske, J. Morfin, K. Schultze, H. Weerts, G. Bertrand-Coremans, J. Sacton, et al., Physics letters B **46**, 138 (1973).

[10] J. B. Spitz, Ph.D. thesis, Yale University (2011).

[11] S. Mikheev and A. Y. Smirnov, Sov. J. Nucl. Phys.(Engl. Transl.);(United States) **42** (1985).

[12] L. Wolfenstein, Physical Review D **17**, 2369 (1978).

[13] J. Lenkeit, Ph.D. thesis, University of Hamburg (2015).

[14] B. Kayser, arXiv preprint hep-ph/0506165 (2005).

[15] E. Majorana, Nuovo Cim **14**, 50 (1937).

[16] J. N. Bahcall, *Neutrino astrophysics* (Cambridge University Press, 1989).

[17] E. Adelberger, A. García, R. H. Robertson, K. Snover, A. Balantekin, K. Heeger, M. Ramsey-Musolf, D. Bemmerer, A. Junghans, C. Bertulani, et al., Reviews of Modern Physics **83**, 195 (2011).

[18] R. Davis, Progress in Particle and Nuclear Physics **32**, 13 (1994).

[19] J. Abdurashitov, V. Gavrin, V. Gorbachev, P. Gurkina, T. Ibragimova, A. Kalikhov, N. Khairnasov, T. Knodel, I. Mirmov, A. Shikhin, et al., Physical Review C **80**, 015807 (2009).

[20] W. Hampel, J. Handt, G. Heusser, J. Kiko, T. Kirsten, M. Laubenstein, E. Pernicka, W. Rau, M. Wojcik, Y. Zakharov, et al., Physics Letters B **447**, 127 (1999).

[21] M. Altmann, M. Balata, P. Belli, E. Bellotti, R. Bernabei, E. Burkert, C. Cattadori, R. Cerulli, M. Chiarini, M. Cribier, et al., Physics Letters B **616**, 174 (2005).

[22] Y. Fukuda, T. Hayakawa, K. Inoue, K. Ishihara, H. Ishino, S. Joukou, T. Kajita, S. Kasuga, Y. Koshio, T. Kumita, et al., Physical Review Letters **77**, 1683 (1996).

[23] K. S. Hirata, T. Kajita, T. Kifune, K. Kihara, M. Nakahata, K. Nakamura, S. Ohara, Y. Oyama, N. Sato, M. Takita, et al., Physical Review Letters **63**, 16 (1989).

[24] Q. Ahmad, R. Allen, T. Andersen, J. Anglin, J. Barton, E. Beier, M. Bercovitch, J. Bigu, S. Biller, R. Black, et al., Physical Review Letters **89**, 011301 (2002).

[25] S. Abe, T. Ebihara, S. Enomoto, K. Furuno, Y. Gando, K. Ichimura, H. Ikeda, K. Inoue, Y. Kibe, Y. Kishimoto, et al., Physical Review Letters **100**, 221803 (2008).

[26] B. Aharmim, S. Ahmed, A. Anthony, N. Barros, E. Beier, A. Bellerive, B. Beltran, M. Bergevin, S. Biller, K. Boudjemline, et al., Physical Review C **88**, 025501 (2013).

[27] F. Kaether, Ph.D. thesis, Ruprecht-Karls-Universität Heidelberg (2007).

[28] B. T. Cleveland, T. Daily, R. Davis Jr, J. R. Distel, K. Lande, C. Lee, P. S. Wildenhain, and J. Ullman, The Astrophysical Journal **496**, 505 (1998).

[29] G. Bellini, J. Benziger, S. Bonetti, M. B. Avanzini, B. Caccianiga, L. Cadonati, F. Calaprice, C. Carraro, A. Chavarria, A. Chepurnov, et al., Physical Review D **82**, 033006 (2010).

[30] G. Bellini, J. Benziger, D. Bick, S. Bonetti, G. Bonfini, M. B. Avanzini, B. Caccianiga, L. Cadonati, F. Calaprice, C. Carraro, et al., Physical Review Letters **107**, 141302 (2011).

[31] K. Abe, Y. Hayato, T. Iida, M. Ikeda, C. Ishihara, K. Iyogi, J. Kameda, K. Kobayashi, Y. Koshio, Y. Kozuma, et al., Physical Review D **83**, 052010 (2011).

[32] J. Cravens, K. Abe, T. Iida, K. Ishihara, J. Kameda, Y. Koshio, A. Minamino, C. Mitsuda, M. Miura, S. Moriyama, et al., Physical review D **78**, 032002 (2008).

[33] J. Hosaka, K. Ishihara, J. Kameda, Y. Koshio, A. Minamino, C. Mitsuda, M. Miura, S. Moriyama, M. Nakahata, T. Namba, et al., Physical Review D **73**, 112001 (2006).

[34] A. Gando, Y. Gando, K. Ichimura, H. Ikeda, K. Inoue, Y. Kibe, Y. Kishimoto, M. Koga, Y. Minekawa, T. Mitsui, et al., Physical Review D **83**, 052002 (2011).

[35] Y. Fukuda, T. Hayakawa, E. Ichihara, K. Inoue, K. Ishihara, H. Ishino, Y. Itow, T. Kajita, J. Kameda, S. Kasuga, et al., Physical Review Letters **81**, 1158 (1998).

[36] M. Ishitsuka et al., arXiv preprint hep-ex/0406076 (2004).

[37] M. Ahn, E. Aliu, S. Andringa, S. Aoki, Y. Aoyama, J. Argyriades, K. Asakura, R. Ashie, F. Berghaus, H. Berns, et al., Physical Review D **74**, 072003 (2006).

[38] P. Adamson, I. Anghel, C. Backhouse, G. Barr, M. Bishai, A. Blake, G. Bock, D. Bogert, S. Cao, C. Castromonte, et al., Physical Review Letters **110**, 251801 (2013).

[39] P. Adamson, C. Ader, M. Andrews, N. Anfimov, I. Anghel, K. Arms, E. Arrieta-Diaz, A. Aurisano, D. Ayres, C. Backhouse, et al., Physical review letters **116**, 151806 (2016).

[40] P. Adamson, C. Ader, M. Andrews, N. Anfimov, I. Anghel, K. Arms, E. Arrieta-Diaz, A. Aurisano, D. Ayres, C. Backhouse, et al., Physical Review D **93**, 051104 (2016).

[41] N. Agafonova, A. Aleksandrov, A. Anokhina, S. Aoki, A. Ariga, T. Ariga, T. Asada, D. Bender, A. Bertolin, C. Bozza, et al., Progress of theoretical and experimental physics **2014**, 101C01 (2014).

[42] D. Forero, M. Tortola, and J. Valle, Physical Review D **90**, 093006 (2014).

[43] A. Aguilar-Arevalo, B. Brown, L. Bugel, G. Cheng, E. Church, J. Conrad, R. Dharmapalan, Z. Djurcic, D. Finley, R. Ford, et al., Physical Review Letters **110**, 161801 (2013).

[44] D. Casper, Nuclear Physics B-Proceedings Supplements **112**, 161 (2002).

[45] C. L. Smith, Physics Reports **3**, 261 (1972).

[46] R. Smith and E. J. Moniz, Nuclear Physics B **43**, 605 (1972).

[47] A. Pais, Annals of Physics **63**, 361 (1971).

[48] N. Cabibbo, Physical Review Letters **10**, 531 (1963).

[49] N. Cabibbo and F. Chilton, Physical Review **137**, B1628 (1965).

[50] S. K. Singh and M. V. Vacas, Physical Review D **74**, 053009 (2006).

[51] S. Mintz and L. Wen, The European Physical Journal A **33**, 299 (2007).

[52] K. Kuzmin and V. Naumov, Physics of Atomic Nuclei **72**, 1501 (2009).

[53] M. R. Alam, M. S. Athar, S. Chauhan, and S. Singh, Journal of Physics G: Nuclear and Particle Physics **42**, 055107 (2015).

[54] V. Hopper and S. Biswas, Physical Review **80**, 1099 (1950).

[55] T. Eichten, H. Faissner, S. Kabe, W. Frenz, J. Von Krogh, J. Morfin, K. Schultze, J. Lemonne, J. Sacton, W. Van Donnick, et al., Physics Letters B **40**, 593 (1972).

[56] O. Erriquez, M. F. Muciaccia, S. Natali, S. Nuzzo, A. Halsteinslid, C. Jarlskog, K. Myklebost, A. Rognebakke, O. Skjeggestad, B. Tvedt, et al., Nuclear Physics B **140**, 123 (1978).

[57] O. Erriques, M. F. Muciaccia, S. Natali, S. Nuzzo, A. Halsteinslid, K. Myklebost, A. Rognebakke, O. Skjeggestad, S. Bonetti, D. Cavalli, et al., Physics Letters B **70**, 383 (1977).

[58] J. Brunner, H.-J. Grabosch, H. Kaufmann, R. Nahnhauer, S. Nowak, S. Schlenstedt, V. Ammosov, V. Ermolaev, A. Ivanilov, P. Ivanov, et al., Zeitschrift für Physik C Particles and Fields **45**, 551 (1990).

[59] I. Sick and J. McCarthy, Nuclear Physics A **150**, 631 (1970).

[60] V. Flaminio, W. Moorhead, D. Morrison, and N. Rivoire, CERN-HERA-83-01 (1983-1984).

[61] V. Flaminio, W. Moorhead, D. Morrison, and N. Rivoire, CERN-HERA-83-02 (1983-1984).

[62] V. Flaminio, W. Moorhead, D. Morrison, and N. Rivoire, CERN-HERA-84-01 (1983-1984).

[63] G.Höhler, Landolt-Börnstein **I/9b2** (1999-2001).

[64] C. Rubbia, Tech. Rep., CERN-EP/77-08 (1977).

[65] S. Amerio, S. Amoruso, M. Antonello, P. Aprili, M. Armenante, F. Arneodo, A. Badertscher, B. Baiboussinov, M. B. Ceolin, G. Battistoni, et al., Nuclear Instruments and Methods in Physics Research Section A: Accelerators, Spectrometers, Detectors and Associated Equipment **527**, 329 (2004).

[66] C. Rubbia, M. Antonello, P. Aprili, B. Baibussinov, M. B. Ceolin, L. Barze, P. Benetti, E. Calligarich, N. Canci, F. Carbonara, et al., Journal of Instrumentation **6**, P07011 (2011).

[67] R. Acciarri, C. Adams, R. An, C. Andreopoulos, A. Ankowski, M. Antonello, J. Asaadi, W. Badgett, L. Bagby, B. Baibussinov, et al., arXiv preprint arXiv:1503.01520 (2015).

[68] J. Spitz, A. Collaboration, et al., in *Journal of Physics: Conference Series* (IOP Publishing, 2011), vol. 312, p. 072017.

[69] M. Soderberg, arXiv preprint arXiv:0910.3433 (2009).

[70] O. Bunemann, T. Cranshaw, and J. Harvey, Canadian Journal of Research **27**, 191 (1949).

[71] A. Martinez, Ph.D. thesis, PhD thesis, Universidad de Granada (2007).

[72] J. B. Birks, Proceedings of the Physical Society. Section A **64**, 874 (1951).

[73] P. Cennini, S. Cittolin, J. Revol, C. Rubbia, W. Tian, P. Picchi, F. Cavanna, G. P. Mortari, M. Verdecchia, D. Cline, et al., Nuclear Instruments and Methods in Physics

Research Section A: Accelerators, Spectrometers, Detectors and Associated Equipment **345**, 230 (1994).

[74] M. Soderberg, arXiv preprint arXiv:0910.3433 (2009).

[75] C. Anderson, M. Antonello, B. Baller, T. Bolton, C. Bromberg, F. Cavanna, E. Church, D. Edmunds, A. Ereditato, S. Farooq, et al., Journal of Instrumentation **7**, P10019 (2012).

[76] http://www.fnal.gov/pub/inquiring/physics/accelerators/00-635D.jpg.

[77] B. C. Brown, P. Adamson, D. Capista, W. Chou, I. Kourbanis, D. K. Morris, K. Seiya, G. H. Wu, and M.-J. Yang, Physical Review Special Topics-Accelerators and Beams **16**, 071001 (2013).

[78] http://operations.fnal.gov/rookie*books*/$BoosterV4.1$.*pdf*.

[79] http://operations.fnal.gov/rookie*books*/$Main\_Injectorv1.1$.*pdf*.

[80] http://arxiv.org/pdf/1507.06690v2.pdf.

[81] A. Abramov, N. Galyaev, V. Garkusha, J. Hylen, F. Novoskoltsev, A. Ryabov, and V. Zarucheisky, Nuclear Instruments and Methods in Physics Research Section A: Accelerators, Spectrometers, Detectors and Associated Equipment **485**, 209 (2002).

[82] S. E. Kopp, arXiv preprint physics/0508001 (2005).

[83] P. Adamson, D. Ayres, C. Backhouse, G. Barr, M. Bishai, A. Blake, G. Bock, D. Boehnlein, D. Bogert, S. Cao, et al., Physical review letters **108**, 191801 (2012).

[84] S. E. Kopp (2015).

[85] D. Michael, P. Adamson, T. Alexopoulos, W. Allison, G. Alner, K. Anderson, C. Andreopoulos, M. Andrews, R. Andrews, C. Arroyo, et al., Nuclear Instruments and

Methods in Physics Research Section A: Accelerators, Spectrometers, Detectors and Associated Equipment **596**, 190 (2008).

[86] D. Drakoulakos, M. Collaboration, et al., arXiv preprint hep-ex/0405002 **16** (2004).

[87] G. Bakale, U. Sowada, and W. F. Schmidt, The Journal of Physical Chemistry **80**, 2556 (1976).

[88] B. Baibussinov, M. B. Ceolin, E. Calligarich, S. Centro, K. Cieslik, C. Farnese, A. Fava, D. Gibin, A. Guglielmi, G. Meng, et al., Journal of Instrumentation **5**, P03005 (2010).

[89] A. Curioni, B. Fleming, W. Jaskierny, C. Kendziora, J. Krider, S. Pordes, M. Soderberg, J. Spitz, T. Tope, and T. Wongjirad, Nuclear Instruments and Methods in Physics Research Section A: Accelerators, Spectrometers, Detectors and Associated Equipment **605**, 306 (2009).

[90] P. Cennini, S. Cittolin, L. Dumps, A. Placci, J. Revol, C. Rubbia, L. Fortson, P. Picchi, F. Cavanna, G. P. Mortari, et al., Nuclear Instruments and Methods in Physics Research Section A: Accelerators, Spectrometers, Detectors and Associated Equipment **333**, 567 (1993).

[91] Engelhard Corporation, MSDS for Cu-0226 S 14 x 28. (2002).

[92] G. Carugno, B. Dainese, F. Pietropaolo, and F. Ptohos, Nuclear Instruments and Methods in Physics Research Section A: Accelerators, Spectrometers, Detectors and Associated Equipment **292**, 580 (1990).

[93] P. Adamson, C. Andreopoulos, K. Arms, R. Armstrong, D. Auty, S. Avvakumov, D. Ayres, B. Baller, B. Barish, P. Barnes Jr, et al., Physical Review D **77**, 072002 (2008).

[94] D. Michael, P. Adamson, T. Alexopoulos, W. Allison, G. Alner, K. Anderson, C. Andreopoulos, M. Andrews, R. Andrews, K. Arms, et al., Physical Review Letters **97**, 191801 (2006).

[95] C. Andreopoulos, A. Bell, D. Bhattacharya, F. Cavanna, J. Dobson, S. Dytman, H. Gallagher, P. Guzowski, R. Hatcher, P. Kehayias, et al., Nuclear Instruments and Methods in Physics Research Section A: Accelerators, Spectrometers, Detectors and Associated Equipment **614**, 87 (2010).

[96] T. Golan, C. Juszczak, and J. T. Sobczyk, Physical Review C **86**, 015505 (2012).

[97] L. Berg, ZAMM-Journal of Applied Mathematics and Mechanics/Zeitschrift für Angewandte Mathematik und Mechanik **62**, 282 (1982).

[98] L. R. Rabiner and B. Gold, Englewood Cliffs, NJ, Prentice-Hall, Inc., 1975. 777 p. **1** (1975).

[99] M. Ester, H.-P. Kriegel, J. Sander, and X. Xu, in *Kdd* (1996), vol. 96, pp. 226–231.

[100] P. V. Hough, in *International Conference on High Energy Accelerators and Instrumentation* (1959), vol. 73.

[101] D. Michael, P. Adamson, T. Alexopoulos, W. Allison, G. Alner, K. Anderson, C. Andreopoulos, M. Andrews, R. Andrews, C. Arroyo, et al., Nuclear Instruments and Methods in Physics Research Section A: Accelerators, Spectrometers, Detectors and Associated Equipment **596**, 190 (2008).

[102] K. A. Partyka, Ph.D. thesis, Yale University (2013).

[103] D. Harris, M. Collaboration, et al., arXiv preprint hep-ex/0410005 (2004).

[104] W. A. Rolke, A. M. Lopez, and J. Conrad, Nuclear Instruments and Methods in Physics Research Section A: Accelerators, Spectrometers, Detectors and Associated Equipment **551**, 493 (2005).